Title
A Double Time of Flight Method For Measuring Proton Light Yield

Author
Brown, Josh Arthur

Publication Date
2017

Peer reviewed|Thesis/dissertation

A Double Time of Flight Method For Measuring Proton Light Yield

By

Josh A. Brown

A dissertation submitted in partial satisfaction of the

requirements for the degree of

Doctor of Philosophy

in

Engineering – Nuclear Engineering

in the

Graduate Division

of the

University of California, Berkeley

Committee in charge:

Professor Jasmina Vujic, Chair
Professor Lee A. Bernstein
Professor Phillip Colella

Fall 2017

A Double Time of Flight Method For Measuring Proton Light Yield

Abstract

A Double Time of Flight Method For Measuring Proton Light Yield

by

Josh A. Brown

Doctor of Philosophy in Engineering – Nuclear Engineering

University of California, Berkeley

Professor Jasmina Vujic, Chair

Organic scintillators have been used in conjunction with photomultiplier tubes to detect fast neutrons since the early 1950s. The utility of these detectors is dependent on an understanding of the characteristics of their response to incident neutrons. Since the detected light in organic scintillators in a fast neutron radiation field comes primarily from neutron-proton elastic scattering, the relationship between the light generated in an organic scintillator and the energy of a recoiling proton is of paramount importance for spectroscopy and kinematic imaging. This relationship between proton energy deposited and light production is known as proton light yield.

Several categories of measurement methods for proton light yield exist. These include direct methods, indirect methods, and edge characterization techniques. In general, measurements for similar or identical materials in the literature show a large degree of variance among the results. This thesis outlines the development of a new type of indirect method that exploits a double neutron time of flight technique. This new method is demonstrated using a pulsed broad spectrum neutron source at the 88-Inch Cyclotron at Lawrence Berkeley National Laboratory.

The double time of flight method for proton light yield measurements was established using two commercially available materials from Eljen Technology. The first is EJ-301, a liquid scintillator with a long history of use. Equivalent materials offered by other manufacturers include NE-213 from Nuclear Enterprise and BC-501A from Saint-Gobain Crystals. The second material tested in this work is EJ-309, a liquid scintillator with a proprietary formulation recently introduced by Eljen Technology with no commercial equivalents. The proton light yield measurements were conducted in concert with several system characterization measurements to provide a result to the community that is representative of the material itself. Additionally, the errors on the measurement were characterized with respect to systematic uncertainties, including an evaluation of the covariance of data points produced and the covariance of fit parameters associated with a semi-empirical model.

This work demonstrates the viability of the double time of flight technique for continuous measurement of proton light yield over a broad range of energies without changes to the system configuration. The results of the light yield measurements on EJ-301 and EJ-309 suggest answers to two open questions in the literature. The first is that the size of the scintillation detector used to measure the proton light yield should not effect the result if the spatial distributions of Compton electrons and proton recoils are equivalent. Second, the shape of the scintillation detector should not effect the light yield with the same constraint on the spatial distributions.

A characterized hardware and software framework has been developed, capable of producing proton light yield measurements on additional materials of interest. The acquisition, post processing, error analysis, and simulation software were developed to permit characterization of double time of flight measurements for a generic system, allowing it to be utilized to acquire and analyze data for an array of scintillation detectors regardless of detector size or geometric configuration. This framework establishes an extensible capability for performing proton light yield measurements to support basic and applied scientific inquiry and advanced neutron detection using organic scintillators.

It came to me in a dream once ... or maybe many dreams.

Contents

List of Figures

List of Tables

Acknowledgments

Without the consistent support I have received throughout the process of obtaining an education, I would not have been successful in this endeavor. I have been remarkably fortunate to have a personal support system constructed of loving friends and family members. Similarly, I am consistently astonished with the brilliance, creativity, and dedication of the research and academic mentors with whom I have had the pleasure of surrounding myself. I am overwhelmed when I reflect on the people who have enabled me to complete this process.

My parents willingness to allow me to tear anything we owned apart, from inexpensive toys to our family's first computer, regardless of the amount of scrap this behavior generated, was essential in my becoming a lifelong learner full of curiosity. My fathers undying faith in my capability, regardless of my reflections at any given time, was grounding and inspiring. Without my mother's strong prodding to return to school, regardless of my conviction that it was too late in life to start such an adventure, I never would have approached this path. My brother's support, both in helping me piece together transportation in the early years of my education and through his universal encouragement and acceptance of me as I was completing this degree, has been essential in me completing it.

I am constantly impressed at the wisdom with which my uncle Sidford Brown approaches any problem I bring to him. His support and guidance have been essential to my success. I wouldn't be writing this without him. His generosity and kindness have made what would have been a very painful process not only tolerable, but enjoyable. I am overwhelmed with gratitude when I reflect on his contributions to my current state.

I am indebted to Ryan Turner for his companionship and support through this process. He has been selflessly willing to listen to me whine about circumstances. He has provided an intellectual outlet for me to grapple with hard questions. I could not have imagined myself with a better friend to blow off steam and explore ideas.

An open invitiation to dinner with Dr. Claudia Stanger and Dan Viele over the last decade provided me with moral support and challenging conversations that were never particularly technical. Their guidance on finding balance while pursuing graduate studies was an important part of my success.

I am grateful for the time I spent with Roger McWilliams. My first experience in a physics lab working with him helped me understand what I needed to be successful in this endeavor. His suggestion that I could work after dinner, not allowing myself to turn into a wastrel in the evenings, changed how I approached this journey. The "fireside chats," as he

would refer to them, helped me reflect on the culture and mentorship I would seek in my future research appointments.

The Bay Area Neutron Group (BANG) has been an absolute pleasure. Dr. Bethany Goldblum's leadership of the group, organizational tenacity, insistence on best coding practices, and requirement that my explanations were not complete without writing the math shaped this work and my skills dramatically. Her pressure for realistic and meaningful uncertainty quantification has driven me to be more thorough and complete and opened up a study of statistics I would not have undertaken without it. Dr. Lee Bernstein's enthusiasm for science is infectious. His willingness to engage in my development as an experimental scientist has been selfless. I have enjoyed his company and benefited immensely from his endless well of ideas. Dr. Darren Bleuel's tireless focus on seemingly needless details has saved me from many erroneous trains of thought. Keegan Harrig has provided direct support of this work since its inception. Her efforts in supporting the experimental campaigns during my tenure in BANG were critical to the success of many cyclotron experiments. Her ability to be positive about testing much of the software developed in this project when it was in really rough states was wonderful and inspiring. Matthew Harasty's efforts in the software development were essential. Dr. Thibault Laplace's willingness to lend a second set of hands or cover the one remaining late night shift should not go unmentioned. I am grateful for his efforts in developing the acquisition software alongside me as well as benchmarking and testing it.

Dr. Walid Younes was critical to my development of the uncertainty analysis for this project. His understanding of physics, statistics, and ability to communicate mathematics is astonishing. My exploitation of his office hours to pick his brain on uncertainty quantification didn't seem to bother him in the slightest. His brilliance is nearly outshone by his kindness and modesty. I am grateful for his time and effort in support of this work and his support in my development of analytic and computational skills.

The radiation detection group at Sandia National Laboratories was essential in all aspects of this project. Dr. David Reyna's enthusiasm for getting the project off the ground was essential in many respects. He provided much of the equipment for the testing and measurements supporting the work, and he helped to organize meetings at Sandia that provided essential feedback on the postprocessing. This development would not have happened without his support. I am also very grateful for his willingness to sit on my qualifying exam committee and his questions about neutrinos that I attempted to fumble through. Dr. Peter Marleau provided inspiration with regard to the data analysis procedures, acquisition software development, and signals processing algorithms. I am grateful for his willingness to toss around ideas freely and how that contributed to this result. I initially found Dr. Erik Brubaker very difficult to understand. His grasp on probability and statistics is astonishing. The final state of the uncertainty quantification is largely due to his early outline of how I might approach the error analysis, which I did not fully grasp until much later in the process. His feedback on the development of the Monte Carlo approach in evaluating the systematic uncertainty was essential in getting it right, and I am grateful for his contributions.

Professor Phil Collela's course on software engineering fundamentally changed what I

thought about writing code for scientific endeavors. The code developed for this project has followed the standards introduced in his course. This has allowed for collaborative development and an ease in bringing in new students that would not have been realized without his tutelage. I am grateful for his willing to serve on my qualifying exam committee, the committee for this thesis, and for his impact on my skills as a scientific software engineer.

Professor Jasmina Vujic has been steadfastly supportive and dedicated to my success as a graduate student and beyond since she took on the role of my adviser. I am grateful for her tolerance in my initial wandering as I was trying to outline a project that would allow me to develop the skills I desired. Her willingness to engage her network on my behalf and support of this project were essential to its success.

This material is based upon work supported by the Department of Energy National Nuclear Security Administration under Award Numbers DE-NA0003180 and DE-NA0000979 through the Nuclear Science and Security Consortium. This report was prepared as an account of work sponsored by an agency of the United States Government. Neither the United States Government nor any agency thereof, nor any of their employees, makes any warranty, express or implied, or assumes any legal liability or responsibility for the accuracy, completeness, or usefulness of any information, apparatus, product, or process disclosed, or represents that its use would not infringe privately owned rights. Reference herein to any specific commercial product, process, or service by trade name, trademark, manufacturer, or otherwise does not necessarily constitute or imply its endorsement, recommendation, or favoring by the United States Government or any agency thereof. The views and opinions of authors expressed herein do not necessarily state or reflect those of the United States Government or any agency thereof.

Chapter 1

Introduction

1.1 Fast Neutron Detection in Organic Scintillators

Detection and characterization of high energy neutrons, in the energy range of $0.5 - 20$ MeV, provides a formidable challenge. The majority of neutron interaction mechanisms lead to partial energy deposition through conversion of some fraction of the neutron's kinetic energy into a nuclear recoil. Proton elastic scattering is a good candidate for fast neutron detection as the neutron can transfer up to its full energy to a proton in a single collision. Since the energy deposition is fractional, incident energy information must be obtained through stochastic methods or by exploiting information of multiple interactions for a single event.

Organic scintillators are a popular medium for detecting neutrons in this energy range. They are composed of aromatic hydrocarbons that luminesce when heavy charged particles or electrons slow down and stop in them. They are largely hydrogenous which means that appreciable interaction probabilities can be obtained using manageable volumes. Since γ-rayscan produce energetic electrons in organic scintillators they are also sensitive to γ-ray fields. Given that in most cases neutron fields are accompanied by γ-ray fields, this is an undesirable quality with respect to the desire to use them as neutron detectors. Thankfully, in many materials, the temporal profile of the luminescence is dependent on the type of incident radiation, meaning that γ-ray backgrounds can be identified and removed in post-processing. Crystal, liquid, and plastic organic scintillators have found a broad spectrum of applications from nuclear security and non-proliferation to basic nuclear physics.

The number of photons produced when a proton of a given energy stops in an organic scintillating medium is stochastic in nature. Thus for a proton with a given energy, the number of photons produced varies around some mean value. Of particular interest is how the mean value varies as a function of the proton energy deposited in the scintillating medium. Since the absolute number of photons produced in a detection system is complicated by many factors, it is useful to compare this to the number of photons produced by electrons of equivalent energies. This ratio between the mean value of the number of photons produced for a electron of a given energy to the mean value of the number of photons produced by

a recoiling proton is the relative proton light yield, and from here on will be referred to as the proton light yield. Working in this relative unit allows the cancellation of several detector-specific quantities. First, the collection efficiency resulting from the specific detector geometry will be canceled out as long as the distributions of energetic particles are similar or the observed difference in light for different spatial locations is small. Second, the photocathode conversion efficiency will be the same between the two quantities and as such will be canceled out when considering the ratio. This means that the ratio quantity should be useful across specific detector configurations allowing a single measurement of the ratio to be used for many configurations. Additionally, the proton light yield is non-linearly proportional to the proton energy, while for a broad range of energies the response to electrons is linear. This makes the electron equivalent light space an ideal one to work in as common calibration sources can be used to establish the relationship between measured quantities and electron energies.

The proton light yield is an input to several applications. These include neutron time of flight, a means of determining incident neutron energies by observing the time it takes neutrons to transit a flight path, where external information regarding the start time and the flight path is required. In this application, the time of the interaction is of primary interest while the detected number of photons is required to be above a light detection threshold. To characterize the efficiency of a neutron time of flight detector setup, knowledge of the number of interactions that led to detection is needed. The number of detected interactions is highly dependent upon the light detection threshold and the relationship between light and proton energy (i.e., proton light yield). Calculations of the neutron detection efficiency of organic scintillators are generally managed via a Monte Carlo code, which requires the relationship between the proton energy and light production as input. For an example of this type of calculation as well as an assessment on the sensitivity of the relation, see Pino et al. [1]. Another application is again spectroscopic, but instead requires external information on the response of the detector to neutrons across a broad range of energies. Using the detector response, a neutron flux corresponding to the measured pulse integral can be obtained through either forward modeling with parameter optimization or matrix inversion techniques. The necessary detector response either needs to be measured or modeled using Monte Carlo methods. The relationship between the proton recoil energy observed in the Monte Carlo trial and the light production is needed to construct the response functions in simulation space. Another application of interest is kinematic imaging. Kinematic imaging involves the detection of multiple neutron-proton elastic scattering events. With the information from multiple interactions, angular information can be derived as well as incident energy information. The kinematic imaging method uses the measured light from the first interaction to establish the recoiling energy, and thus the energy loss in the first interaction. So the inverse of the proton light yield relation is needed. The work here was primarily motivated by the last example.

1.2 Scope of the Work and Overview

Measurements of proton light yield in the literature have historically shown much disagreement. Significant speculation exists as to the source of these discrepancies. Some of the postulates include differences due to different detection volumes, geometries, and readout systems, or potentially variance in the material itself. Only the last postulate here should have a differential effect on the ratio of electron light to proton light. This works attempts to address some of these open questions through the development and implementation of a novel method for measuring proton light yield and a review of the current status of the literature. The development of a system for performing proton light yield measurements is also detailed as the intention is to deliver a functional system capable of providing needed inputs to the radiation detection community as well as answering unresolved questions regarding the underlying physics of the materials of interest.

In Chapter 2, the composition and light production mechanisms of organic scintillators is discussed. Then, an established semi-empirical model useful in characterizing light production in response to neutrons is introduced. Following this, the energy deposition mechanisms for both γ-ray interactions, which lead primarily to recoiling electrons, and neutron interactions, which lead primarily to recoiling protons, are explored. A discussion of neutron-proton elastic scattering kinematics as relevant to light yield measurements is included.

Chapter 3 provides a look at the history of methods to measure proton light yield following the evolution from initial work to current popular methods. Chapter 4 begins with the neutron detectors and readout system used in this work. This is followed by a discussion of the basic digital signal processing algorithms used to reduce waveform data to physics quantities. A GEANT4 [2] construction of the apparatus used in the experimental efforts is also discussed. Next, a code package developed to calibrate the measured quantities into the electron equivalent space is described. Lastly, the double time of flight method for measuring light yield that is the focus of this work is described.

Chapter 5 begins with an overview of the experimental setup including a specification of the neutron beam generated at the 88-Inch Cyclotron at Lawrence Berkeley National Laboratory exploiting deuteron breakup. Next, the neutron scattering array used to measure the proton light yield and associated experimental details are described. Next, an experimental apparatus used to measure the phototube linearity is detailed. Lastly, the details of the data collection for γ-ray calibrations are included.

Chapter 6 presents the results of simulating both the scattering array's response to a neutron beam and the γ-ray data collected. The results of the simulation with respect to both an investigation of the anticipated proton energy resolution and the potential for bias between the spatial recoil distributions of γ-ray interactions and neutron interactions are explored. Additionally, the anticipated recoil energy distribution for the calibration γ-ray sources are presented.

Chapter 7 details how the information about the system is combined with the experimental data to produce the proton light yield relation. This focuses both on how the data were processed and on the software developed to manage it and includes information on pro-

cessing the linearity data and how the correction is applied to the experimental data from both the light yield measurement and calibration data collection. The specific details on selecting events based on physics constraints is presented. The calibrations of the system are discussed for both the light and time dimensions. Finally, an assessment of the systematic contributions to the uncertainty in the measurement is detailed.

Chapter 8 presents the results of the proton light yield measurements produced as a result of this work and discusses them in the context of the existing literature. Additionally, the state of the developed system and work being continued on the developed platform are explored.

Chapter 2

Theory

This chapter first presents a functional definition and overview of the properties of organic scintillators and then explores the mechanisms for energy deposition by radiation of interest in these materials.

2.1 Organic Scintillators

In the context of this work, organic scintillators refer to materials composed of aromatic hydrocarbons that emit visible light following molecular excitation after an interaction with radiation. They can generally be classified as unitary, binary, or higher order materials corresponding to the number of included compounds. Unitary materials represent organic crystals, while the higher order materials can be either doped crystals or solutions where the aromatic hydrocarbons are contained in a solvent [3]. The excitation leading to light emission can occur through several pathways: prompt fluorescence, delayed fluorescence, and phosphorescence. The light emission process is more complicated in non-unitary materials as the primary energy deposition occurs in the solvent and there must be energy transfer to the luminescent molecules. Regardless, the same pathways for luminescence exist in non-unitary materials.

A common feature in organic scintillators is the presence of carbon ring structures that give rise to hybridized sp^2 orbitals resulting in covalent σ bonds. This hybridization leaves the p_z orbital of an individual carbon atom unchanged and protruding orthogonal to the plane of the ring on the top and bottom of the molecule. The p_z orbitals have strong overlapping spatial configuration and result in a π orbital with delocalized electrons. The excitation and decay of these delocalized π electrons form the basis for luminescence in organic scintillators [4]. The excitation of these electrons can be illustrated in a similar manner to most quantum systems by a series of discrete energy levels. Excited states of these molecules include both singlet and triplet states. Pathways for luminescence will be explored through these Jablonski diagrams beginning with prompt fluorescence.

2.1.1 Prompt Fluorescence

Prompt fluorescence is the primary detected light in a radiation detection application of organic scintillators. The scintillator molecule has an excitation of a π electron of the molecule to an excited singlet state. Following the excitation, the molecule relaxes to the first excited singlet state through radiationless transitions involving phonons or the generation of heat. Once in the lowest-lying first excited state, the excitation decays via the production of a photon, in general, to a state in the vibrational ground state band of the molecule. The decay to a state in the ground state vibrational band is important in that the energy of the photon is less than the energy required for re-absorption in the material. A Jablonski diagram of this process is shown in Figure 2.1.

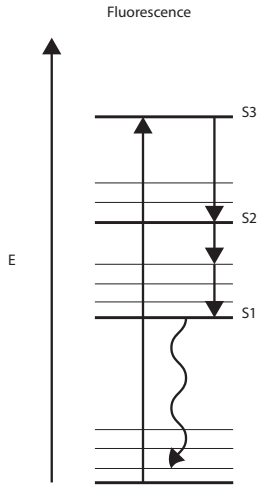

Figure 2.1: Jablonski diagram showing the excitation, radiationless relaxation, and luminescent decay of an organic molecule, a process known as prompt fluorescence

2.1.2 Delayed Fluorescence

Another means of generating light in organic scintillators is delayed fluorescence. Instead of a single molecule producing light, delayed fluorescence requires a bimolecular interaction between two molecules in excited triplet states. The triplet states are created either by intersystem crossing from a singlet state, or recombination following ionization. When two molecules with triplet state excitations interact, triplet-triplet annihilation can occur leaving one of the excited molecules in an excited singlet state and the other in the singlet ground state. The singlet excited state can then decay via photon emission to the ground state band. The half life of the triplet states is much longer than that of the singlet states, and the reaction is bimolecular, meaning it requires two excited states locally, which leads to a longer characteristic time of emission. The requirement that multiple excited molecules be present also means that processes leading to higher ionization densities can produce more delayed light than processes that have lower ionization densities. This behavior is in

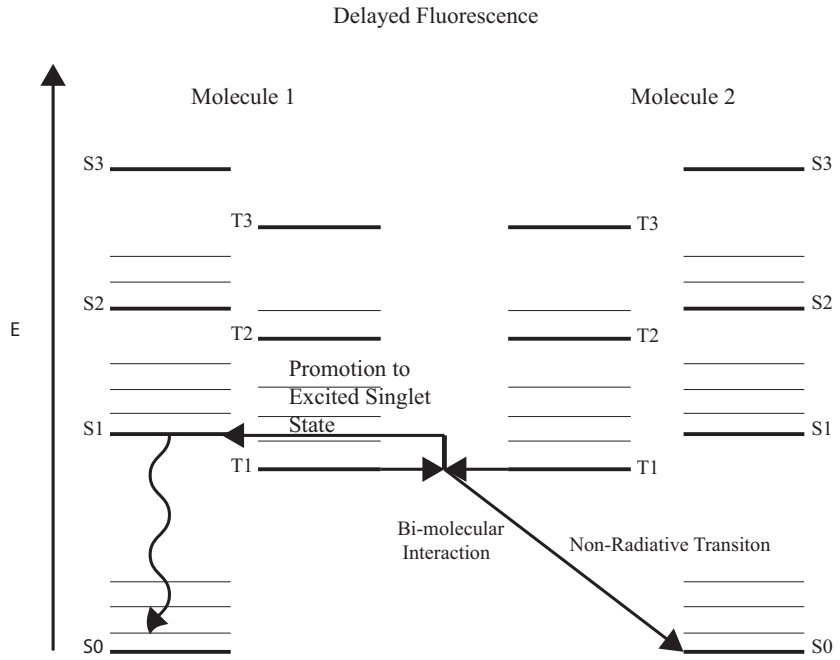

Figure 2.2: Jablonski diagram showing the bimolecular interaction of two excited π electrons leading to the radiationless transition to the ground state for one of the molecules, and the promotion to a singlet state for the other. The molecule left in the excited singlet state is free to decay leading to delayed fluorescent light.

part responsible for measurable differences in pulse shapes for electron energy deposition and energy deposition from heavy charged particles. A Jablonski diagram of the delayed fluorescence process is shown in Figure 2.2.

2.2 Quenching Mechanisms in Organic Scintillators and Birks Model

The term 'quenching' refers to energy deposited in a scintillator that does not result in the production of detectable photons. Several mechanisms exist that provide energy loss and do not lead to detectable photon emission. These include singlet ionization quenching, radiationless de-excitation, molecular damage, contamination quenching, and triplet-triplet annihilation. Singlet ionization quenching occurs when two singlet states undergo a bimolecular interaction similar to triplet-triplet annihilation leaving one of the molecules in the ground state and the other in a higher lying singlet excited state. The result is the reduction in potential for photon production as one of the excited states is lost. Radiationless de-excitation can occur both in the relaxation to the lowest lying excited excited singlet state and potentially from the first excited state to the ground. Both of these processes consume energy without the production of detectable photons. Due to the comparatively

high energies of both protons and electrons following a radiation interaction, the potential to ionize σ electrons exists which leads to a damaged molecule. Contamination quenching refers to a potential process where a singlet or triplet state can transfer its energy to an undesired contaminant. Dissolved oxygen in liquid scintillators is a common contaminant and leads to a reduction both in the overall light yield and in the ability to observe pulse shape differences. It is common to bubble liquid scintillators with nitrogen to displace the oxygen in the environment. Similar to singlet ionization quenching, triplet-triplet annihilation reduces the potential for light emission by transferring one of the excited state directly to the ground state band without emitting radiation.

Of primary interest in this work is the non-linearity in the relationship between proton energy deposition and the number of photons produced. The difference in both the magnitude and temporal profile of the photon production from energetic electrons and proton recoils comes from differential quenching. The difference in quenching is postulated to come from the large difference in stopping power, or the energy deposition per unit pathlength. Of the above-mentioned quenching mechanisms, three potentially lead to differences in quenching between recoiling protons and energetic electrons. Both singlet-singlet annihilation and triplet-triplet annihilation require two locally-excited molecules to exist. Thus, if there are more locally excited molecules, these processes have a higher probability of occurring. This makes these two mechanisms prime candidates for the difference in quenching between the two particles. The third is molecular damage. The higher stopping power for proton interactions leads to a larger probability of ionizing a σ electron and damaging a molecule when compared to electron energy deposition.

A semi-empirical model introduced by Birks attempts to characterize the photon emission for different particles using the stopping power of the particle [5]. Specifically, Birks introduced a relation describing the differential photon production per unit path length:

$$\frac{dL}{dx} = \frac{S\frac{dE}{dx}}{1 + kB\frac{dE}{dx}}, \tag{2.1}$$

where L is the light emission in number of photons, x is distance along the path in cm, E is the energy of the particle in MeV, S is the scintillation efficiency or the number of exitons produced per unit path length, B is the fraction of molecules damaged per unit pathlength, and k is the fractional probability that a damaged molecule will lead to light emission. When working with the relative light yield, the units here are changed so that L is the light emission in MeVee, and S is the light emission relative to an electron per unit energy deposited in $\frac{MeVee}{MeV}$. The MeVee unit is the light observed compared to that observed for Compton electron of a given energy.

This relation can be modified by multiplying both sides by the inverse of the stopping power to yield

$$\frac{dL}{dE} = \frac{S}{1 + kB\frac{dE}{dx}}, \tag{2.2}$$

which describes the differential light production in MeVee per unit energy deposited in MeV. This can be integrated to yield a description of the total light production for a particle with

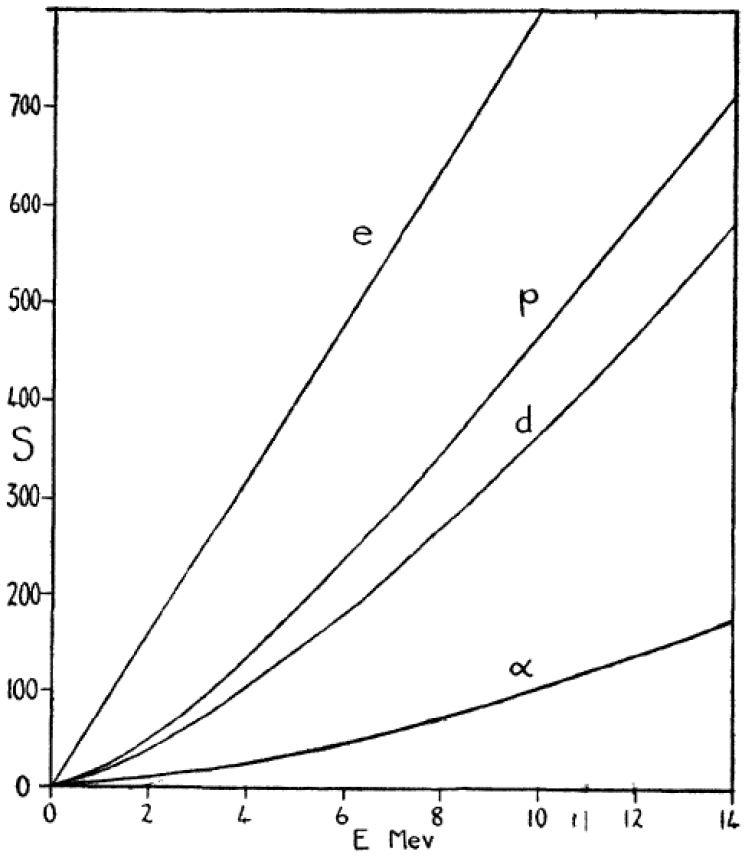

FIG. 2. Calculated scintillation response of anthracene to electrons, protons, deuterons, and α-particles.

Figure 2.3: Light yield for a number of particles as described by Birks relation. Reproduced from [5].

an initial kinetic energy E_i as

$$L(E_i) = S \int_0^{E_i} \frac{dE}{1 + kB\frac{dE}{dx}(E)}. \tag{2.3}$$

The integral in Eq. 2.3 must be computed numerically due to the complexity of the energy dependence of the stopping power for the particles of interest. Figure 2.3 shows the results from the original reference [5] showing the predicted light yield for various particles. Although the model only addresses one of the proposed quenching mechanisms (i.e., molecular damage), it provides good predictions for particles of interest in the energy range explored in this work. It should be noted that for much heavier particles ($A > 12$) and for very low energies (electron energies < 100 keV and proton energies < 500 keV), the model diverges from experimental observations [3].

2.3 Energy Deposition Mechanisms in Organic Scintillators

The organic scintillators used in this work provide simultaneous detection of neutrons and γ rays with the ability to distinguish between the type of interacting radiation via pulse shape discrimination. Detectable events from neutron interactions primarily come from the elastic scattering of neutrons on protons, while detectable events from γ rays primarily come from Compton scattering or pair production.

2.3.1 Neutron Energy Deposition Mechanisms

When considering the elastic scatter of a neutron on a proton, the initial state of the system can be considered as an energetic incident neutron with energy, E_n, and a free stationary proton, given that the molecular binding energies of the organic molecules and thermal motion are negligible compared to detectable neutron energies. Following n-p elastic scattering, the system is left with both an energetic neutron with energy E'_n and a proton with energy E_p both dependent on the scattering angle θ. A diagram of this interaction is shown in Figure 2.4.

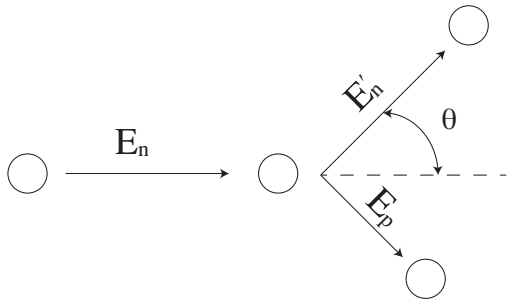

Figure 2.4: neutron proton elastic scattering diagram showing the primary means of neutron energy deposition leading to light output in organic scintillators.

Several n-p elastic scattering relations are used throughout this work. Using conservation of energy and momentum, it can be shown that the proton recoil energy can be calculated in terms of several other parameters. That is,

$$E_p = \sin^2(\theta) E_n, \tag{2.4}$$

and

$$E_p = \tan^2(\theta) E'_n, \tag{2.5}$$

and finally

$$E_p = E_n - E'_n. \tag{2.6}$$

Similarly, the incoming and outgoing neutron energy can be related by

$$E'_n = \cos^2(\theta) E_n. \tag{2.7}$$

Following an n-p scattering event in the organic scintillator, the resultant energetic recoiling proton slows down in the material through excitation and ionization of the organic molecules, which ultimately leads to light emission. The specific ionization along the path of the proton is high compared to that for electrons, which leads to a relative enhancement of the delayed fluorescence as well as an increase in the quenching of the prompt fluorescence via singlet-singlet annihilation. The combination of these differences gives rise to different observed pulse profiles enabling pulse shape discrimination between protons and electrons.

Additionally, an understanding of the distribution of proton energies resulting from a given incident neutron energy is required. The n-p elastic scattering reaction in the center-of-mass frame for energies less than 10 MeV is isotropic. Furthermore, as the masses of the neutron and proton are approximately equal and the scattering process is elastic, the total kinetic energy of the particles before the collision is equal to the total kinetic energy after the collision. A diagram of both the center-of-mass and lab frame relations is shown in Figure 2.5.

Since the scattering process in the center-of-mass frame is isotropic, the probability of scattering into a given angle β in the center-of-mass frame is given as

$$P_\beta(\beta)d\beta = \frac{1}{2}\sin(\beta)d\beta. \tag{2.8}$$

To translate this to the lab frame and obtain a distribution function for the resultant proton energies, a relation between β and the recoiling particle energy is required. To begin

$$P_\beta(\beta)d\beta = P_\theta(\theta)d\theta, \tag{2.9}$$

where θ is the scattering angle in the lab frame. This can be re-arranged as

$$P_\theta(\theta) = P_\beta(\theta)\frac{d\beta}{d\theta}. \tag{2.10}$$

The conservation of kinetic energy in the center-of-mass frame leads to initial and final momentum vectors of equal length. Since the difference between the momentum vector in the center-of-mass and lab frame is $\frac{1}{2}M_nV_n$, where M_n is the mass of the neutron and V_n is the velocity of the incident neutron, and the y components of the momentum vectors in the center-of-mass and lab frames are equal, an isosceles triangle is formed that allows the relation of β and θ to be elucidated. The result is

$$\beta = 2\theta. \tag{2.11}$$

Taking the derivative and substituting it back into Equation 2.10 gives

$$P_\theta(\theta) = \sin(2\theta)d\theta = 2\sin(\theta)\cos(\theta)d\theta. \tag{2.12}$$

To relate the energy and angle distributions:

$$P_{E_p}(E_p)dE_p = P_\theta(\theta)d\theta, \tag{2.13}$$

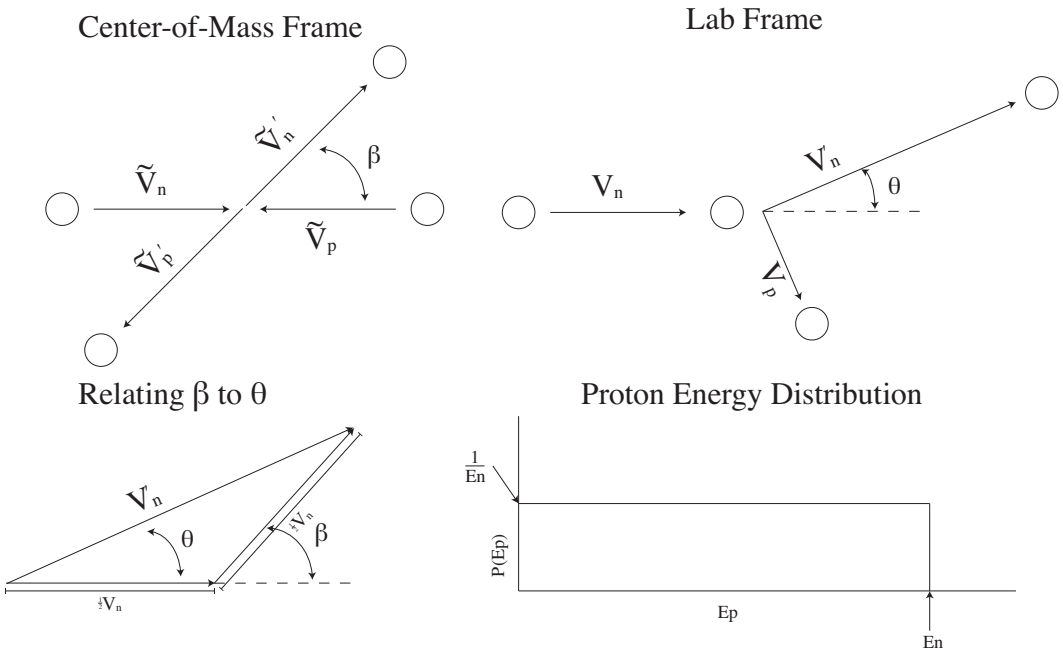

Figure 2.5: Diagram of n-p elastic scattering relationships.

which is equivalent to

$$P_{E_p}(E_p) = P_\theta(\theta)\frac{d\theta}{dE_p}. \tag{2.14}$$

Looking back at Equation 2.4, this gives

$$\frac{dE_p}{d_\theta} = 2\sin(\theta)\cos(\theta)E_n. \tag{2.15}$$

A combination of Equations 2.12, 2.14, and 2.15 yields the desired distribution function:

$$P_{E_p}(E_p) = \frac{1}{E_n}, \tag{2.16}$$

which is notably constant across the proton energy spectrum up the the maximum possible energy (i.e., the incoming neutron energy). This means that the ideal energy deposition spectra for a flux of mono-energetic neutrons is given by a rectangle, illustrated in Figure 2.5. So, all recoil proton energies are equally probable between 0 and the incoming neutron energy.

2.3.2 γ-ray Energy Deposition Mechanisms

Compton scattering, diagrammed in Figure 2.6, is the primary means of γ-ray interaction

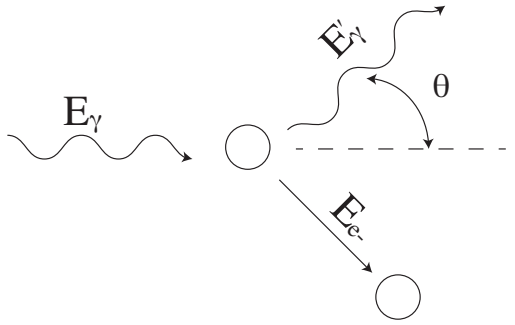

Figure 2.6: Compton scattering diagram showing the primary means of γ-ray interactions leading to light output in organic scintillators.

that eventually leads to light production in organic scintillators. An incoming γ ray undergoes an elastic scatter on what can be considered a free electron. The Compton electron energy can be shown through conservation of energy and momentum to be

$$E_{e-} = E_\gamma \left(1 - \frac{1}{1 + \frac{E_\gamma}{E_0}\left(1 - \cos(\theta)\right)} \right), \tag{2.17}$$

where E_{e-} is the energy of the Compton electron, E_γ is the incident γ-ray energy, E_0 is the rest mass energy of an electron in the same unit as the γ-ray energy, and θ is the angle of the scattered photon. This equation has a maximum recoil energy corresponding to a back-scattered γ ray given by

$$E_{e-} = E_\gamma \left(1 - \frac{1}{1 + 2\frac{E_\gamma}{E_0}} \right), \tag{2.18}$$

which is the energy of the Compton edge – the feature corresponding to the upper energy limit of the energy distribution from the scattering of a mono-energetic γ-ray source. The energy distribution of Compton electrons from a mono-energetic source is derived from the the Klein-Nishina formula that describes the angular differential cross section $\frac{d\sigma}{d\Omega}$ [6]. It must be integrated over the ϕ dimension and translated into energy space. From [7], the resulting formula for the distribution is given as:

$$\frac{d\sigma}{dE_{e-}} = 2\pi r_0^2 \sin(\theta) g(\theta) \left[\frac{\left(1 + \frac{E_\gamma}{M_e}\left(1 - \cos(\theta)\right)\right)^2 M_e}{E_\gamma^2 sin(\theta)} \right], \tag{2.19}$$

where

$$g(\theta) = \left(\frac{E'_\gamma}{2E_\gamma} \right)^2 \left(\frac{E'_\gamma}{E_\gamma} + \frac{E_\gamma}{E'_\gamma} - \sin^2(\theta) \right) \tag{2.20}$$

and r_0 is the classic electron radius, $\frac{1}{4\pi\epsilon_0}\frac{e^2}{M_e}$. Although other mechanisms for γ-ray energy deposition exist, the relative cross sections are very small and the anticipated ideal response

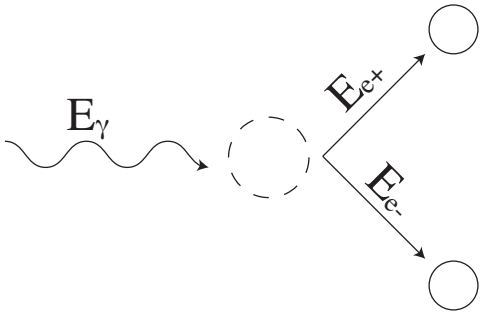

Figure 2.7: Diagrammatic representation of pair production.

of an organic scintillator to a mono-energetic γ ray is described by the distribution in Eq. 2.19 plus geometric effects. If the γ-ray interaction is of higher energy, pair production begins to contribute (illustrated in Fig. 2.7). In the detectors used in this work, this leads to a double escape peak as the annihilation photons generally both escape. Example calculations of Compton recoil probability distributions for a few common γ rays are shown in Figure 2.8.

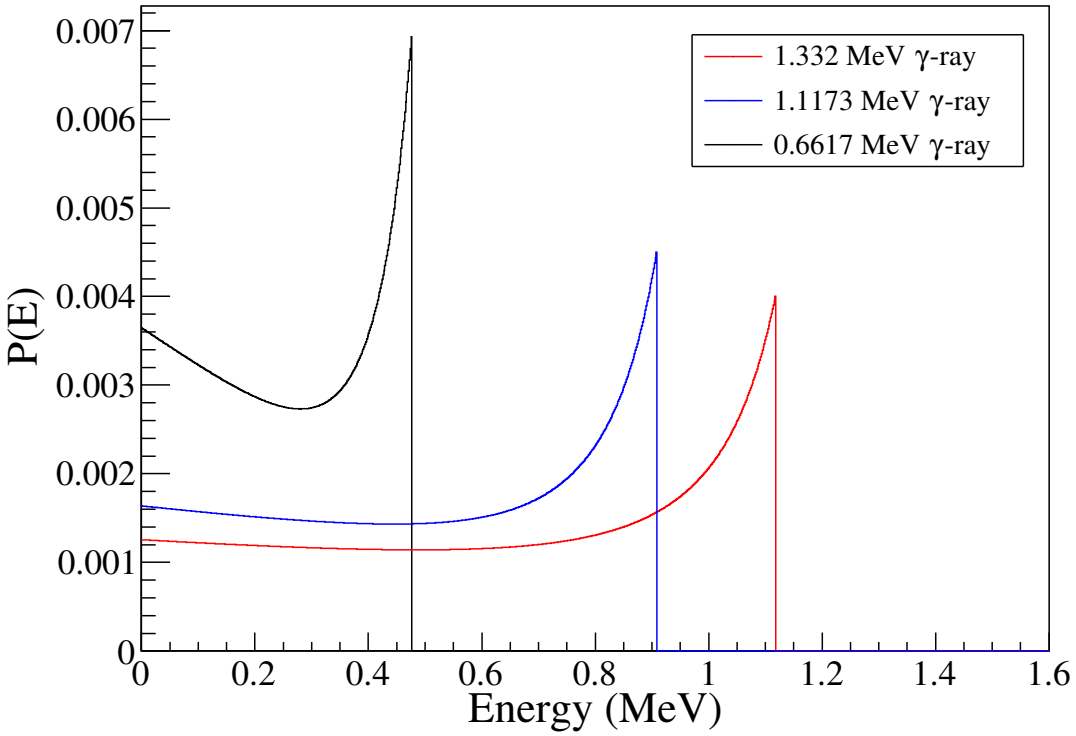

Figure 2.8: Calculations of the probability distribution of electron kinetic energy following a Compton scattering event as described in Eq. 2.19.

Chapter 3

Foundational Work

Given the importance of the proton light yield relation in understanding the response of neutron detection systems employing organic scintillators, it is unsurprising that experimental techniques for measuring the relationship have been employed since shortly after their discovery. A review of the literature produces three broad categories of light yield measurements: direct methods, edge characterization methods, and indirect methods. The review article by Brooks from 1979 [3] makes several recommendations for measuring light yield, some of which require re-interpretation due to advances in methodology. To start, Brooks suggests that geometries should be normalized and that the absolute light collection efficiency of the readout system should be known. Working in a relative unit, where the light is reported relative to the electron equivalent energy, makes both of these recommendations unnecessary. They are instead replaced by the following recommendations. The geometry and method used for the relative calibration procedure must not lead to different spatial distributions of Compton electrons and proton recoils. Alternatively, the method of electron equivalent calibration method must be shown to be unbiased with regard to the spatial distribution of Compton electrons. Additionally, the means of relating measured proton light back to electron light must be well characterized and provide a good calibration across the energy range reported.

Brooks' next recommendations involve sample conditioning. With liquids, care should be taken that no oxygen is present in the sample as it leads to contamination quenching. With plastics and crystals, the surfaces should be clean and free of contaminants if a direct method is to be used. Brooks also makes recommendations regarding potential bias from the readout system. First, he recommends that the response across the entire photocathode should be uniform. Again, this is mitigated by a relative measurement to electron light with the same caveats as above. Secondly, the system response should be linear across the full range of light considered. An alternative provided herein is the suggestion that the non-linearity of the system should be well characterized and compensated for in the data interpretation. Third, Brooks states that the integration time constant for the pulse processing chain should be specified, as short time constants will lead to a result primarily proportional to the singlet decay, and that integration times may need to be as large as

500 ns to capture the full emission of an event. In view of the development and common use of waveform digitizers, this should include that the digital pulse processing chain should be clearly defined including the method of baseline estimation and integration time. Brooks also notes that most of the measurements, of which he has a short review, are lacking in one of these outlined aspects. This continues to be the case in more modern literature with few exceptions. In this section, the three categories of light yield measurements are explored with examples from the literature, starting with direct methods.

3.1 Direct Methods

Much of the early work in the 1950s on understanding the nature of light production in organic scintillators was focused on crystals, specifically anthracene, and used direct methods. A thorough example – characteristic of the early direct measurements – is found in Taylor et. al. from 1951 [8]. The authors use the University of Illinois cyclotron to produce energetic beams of either protons, deuterons or α-particles that were then degraded with aluminum foils to achieve multiple energies. The beams were extracted from the cyclotron into open air and then made incident onto a crystal placed on the front face of a photomultiplier tube covered by a thin aluminum foil. The authors investigated multiple crystals with the apparatus. This example of an early direct method shows some of the general features of this category of measurements. They generally involved using low-energy-capable linear accelerators, or cyclotrons, to generate monoenergetic beams of protons or alpha particles. The beams were made incident on small samples of the material of interest and read out using photomultiplier tubes and analog pulse shaping circuits. The energy of the incident beams was modified by a series of aluminum degrader foils. A good review of the early measurements is found in Ref. [4] and evinces a large degree of variance between results obtained from different early experiments.

Another type of direct measurement developed with the intent of observing the differential quantity given by Equation 2.1 directly involves the use of thin scintillating foils. Voltz et. al. [9] developed an apparatus of this type by depositing thin films of scintillating material of interest onto a glass substrate and loosely coupling a photomultiplier tube such that the detection never exceeded single photons. The authors then related the coincident rate between a surface barrier detector and the photomultiplier tube either in the presence or absence of the scintillating film. The surface barrier detector was placed such that particles passing through the scintillating film would be detected in it, and thus their energy, and their energy deposition in the thin film could be determined. The authors then use the differential coincident event rate to determine the total light yield for a given energy deposition.

Although almost all of the early work on understanding the luminescent response of organic scintillators to energetic particles was accomplished using direct methods, very little modern work uses them demonstrating a preference for either indirect or edge characterization methods. Several reasons for this exist. First, it was known very early on that using surface incident particles produced different light yield results when compared to using re-

coiling particles [4]. Next, the spatial distributions of light generation are fundamentally different for directly incident charged particles compared to recoiling particles. The spatial extent of modern scintillation detectors is on the order of cm while the range of particles in the energy regime of interest is on the mm scale. For recoiling particles, the interactions happen throughout the volume producing light, while for directly incident charged particles the light comes from a small region where the particle stops. This effect can be reduced by using small samples, but the use of γ-ray calibration sources will still lead to different spatial distributions of light production and potential biases. Additionally, the use of liquid scintillators would require either appropriate vacuum-rated housings or extracting charged particle beams into air, the latter of which is undesirable from an uncertainty and radiological risk perspective. Finally, given the variance of the results for different systems, much of the current work tends to focus on obtaining an empirical understanding of the total response of a system under study as opposed to an attempt to extract general materials properties. As such, separately-developed test systems are less desirable when compared with the ability to measure the observed light output of the system of interest, as both indirect and edge characterization methods allow.

3.2 Edge Characterization Methods

Edge characterization methods for determining proton light yield involve the exploitation of Equation 2.16, which shows that the expected response to a monoenergetic flux of incident neutrons is a rectangular probability distribution with the right edge of the rectangle corresponding to protons with an energy equal to that of the incident neutron. This in principle should allow an experimenter to measure the response of a scintillator of interest to series of monoenergetic incident neutron fluxes and relate the edge of the response for each of these fluxes to a proton energy, thereby producing a series of points relating the observed light and inferred proton energy. One of the earliest papers demonstrating this idea comes from Kraus et. al. [10]. The authors here attempt to establish an estimate of the ratio of light production from electrons to protons, which at the time was thought to be roughly an order of magnitude lower, by looking at the endpoint of distributions from Compton scattered γ rays and neutrons both with roughly 0.5 MeV recoiling particles; They showed that the light ratio was closer to a factor of two. Several other authors work with this idea in the late 1950s and early 1960s [11] [12] [13] with perhaps Batchelor et. al. [13] being the first to systematically cover an energy range for recoiling protons.

One of the most cited papers, produced about a decade later, comes from Verbinski et. al. [14]. This work provided a complete outline of the edge characterization approach with an extension that featured a Monte Carlo feedback loop. Verbinski approached the characterization by obtaining 20 different monoenergetic beams using a series of monoenergetic nuclear reactions – $T(p,n)^3He$, $D(d,n)^3He$, and $T(d,n)^4He$ – induced by particles accelerated from a 5 MeV Van de Graaf generator. This allowed the authors to access energies ranging from 0.2 MeV up to 22 MeV, but required dramatic changes in the accelerator configuration

to do so. For a determination of the light corresponding to these proton recoil energies, Verbinski took the half-height of the edge of the measured distributions and related it to the endpoint of an observation of the bienergetic γ-ray spectra generated by ^{22}Na, similar to the MeVee electron equivalent scale. The measured distributions as well as calibration spectra are reproduced here in Figure 3.1. Instead of taking these light values and known proton energies corresponding to the endpoint of the recoil spectrum as absolute points on the light yield curve, the authors used these data as an initial estimate of the light yield. This estimated light yield relation was then used as a trial input for a Monte Carlo calculation of the measured response functions, where the result was used in a feedback loop to make corrections to the trial light yield relation. The output was a nearly continuous series of data points describing the relationship for NE-213, a longstanding commercially-available liquid scintillator. What is notably missing from this work is the size of the correction factors that were obtained to adjust the data points taken directly from the half-height of the edge of the response functions at a given energy to give the resultant light yield relation.

A more recent development on this method involves a more sophisticated means of characterizing the maximum proton recoil edge. Kornilov et al. [15] generated a series of quasi-monoenergetic response functions using a tagged time of flight technique in conjunction with a ^{252}Cf spontaneous fission source. The authors then investigated the derivative of the resultant quasi-monoenergetic response functions. The derivative was characterized by an inverted Gaussian function, where the mean was taken as the proton recoil edge. This is born from the reasoning that the derivative of a rectangle (i.e., the idealized energy deposition spectrum) convolved with a Gaussian distribution (reflective of the detector resolution function) is indeed an inverted normal distribution. The authors made a single comparison between their edge determinations and modeled response functions at 4 MeV, specifying the relative difference between the modeled and measured response as less than 5%. They also noted that their material, LS301, another commercially available liquid scintillator thought to be equivalent in formula to NE-213, exhibited a light yield roughly 15% less than a measurement for NE-213, concluding that this was a difference in the purported equivalent material. Additionally, recent work has been conducted that used time of flight methods to generate continuous measurements of the proton light yield using the edge characterization technique of Kornilov [16] for EJ309, a recently developed liquid scintillator measured in this work, over the lower portion of the fast neutron energy regime. Another recent measurement by Scherzinger et al. [17] examines the difference in result using both Kornilov's method and the half-height prescription for edge characterization. The author finds that the simulations of mono-energetic neutron response functions agree at the 1% level at 5 MeV, but disagree by nearly 20% when considering a 3 MeV response. Additionally, little disagreement between the half-height method and the method of Kornilov was observed. Scherzinger also explored the difference in results considering different integration lengths. The author notes a dramatic difference in the result for integration times of 35 ns vs. 475 ns of nearly 20%.

There are several practical complications to this approach. The idealized rectangular response is distorted by several effects. One of the distortions comes from the non-linear proton light yield itself. The non-linearity leads to a non-linear compression of the idealized

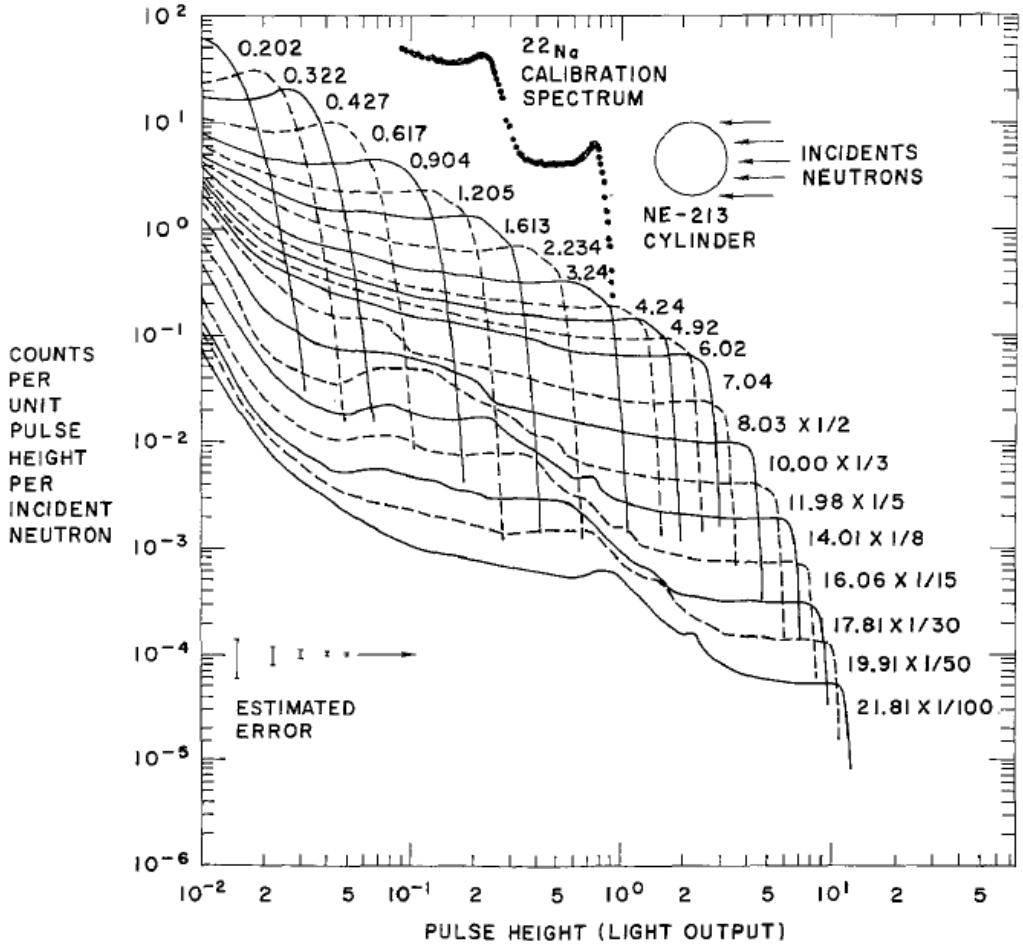

Figure 3.1: Measured monoenergetic response functions, an incident neutron flux diagram, and the result of a measurement of the bienergetic γ-ray flux from a ^{22}Na calibration source. Each curve represents the measured light distribution for a given neutron energy, labeled to the right of the lines and scaled by a given factor to make the plot more observable. Half-heights of the edges of these distributions were taken as trial light yield values and then corrected in a feedback loop with a Monte Carlo calculation of the anticipated response. Reproduced with permission from Elsevier [14].

proton recoil distribution such that in the low light region, where the non-linearity is most pronounced, the probability of observing light increases rapidly when approaching the origin. When considering the effect that this has on the edge of the recoil distribution, it causes more distortion near the edge for lower energy considerations. Another distortion comes from multiple n-p scattering reactions in the scintillator volume. This again is more problematic at lower energies as the probability of the multiple events generating a similar amount of light as a single n-p scattering event increases, and the probability of multiple n-p scattering events increases. These effects are potentially mitigated with the use of feedback between the measurement and a Monte Carlo estimate although this is not common practice. Recent work from Bai et al. [18] uses the same methods as Verbinski, including the Monte Carlo feedback loop, and details that the difference between the edge characterization output and the final result corrected with the Monte Carlo is less than or equal to 8% across the energy range considered.

3.3 Indirect Methods

Alongside the development of edge characterization techniques, a method referred to as the indirect method was developed. An early comprehensive paper that outlines the method and explores a series of materials in common use in 1968 comes from Smith et al. [19], in which he states:

> There are two methods for measuring the response of a scintillator to charged particles. The direct method is to bombard the scintillator with external beams of charged particles. The indirect method is to bombard the scintillator with mono-energetic beams of neutral particles such as gamma rays and neutrons of which a portion will elastically scatter from charged particles within the scintillator. Unique energy recoils will be recorded only if one detects the elastically scattered neutral radiation in a second detector, placed at a specific angle relative to the incident beam direction, in time coincidence with the recoil pulse.

Although this work was produced at nearly the same time as that of Verbinski [14], which detailed the edge characterization method, the summary from Smith et al. recognizes only the direct and indirect measurement approaches to proton light yield. Regardless, the quote provides an overview of the indirect method.

A diagram of the setup utilized by Smith et al. [19] is shown in Figure 3.2. Smith exploited mono-energetic incident neutrons, γ rays, and a two-detector scattering setup to measure coincident events between the detectors. For the γ-ray events, the coincidences correspond to a Compton scattering event in the primary scintillator and any reaction leading to detection in the secondary detector. This leads to an energetic Compton electron in the primary detector whose energy can be calculated from kinematics. For neutrons, the coincidences correspond to an n-p scattering event in the primary detector and any reaction leading to a detectable event in the secondary detector. This leads to an energetic recoil proton in

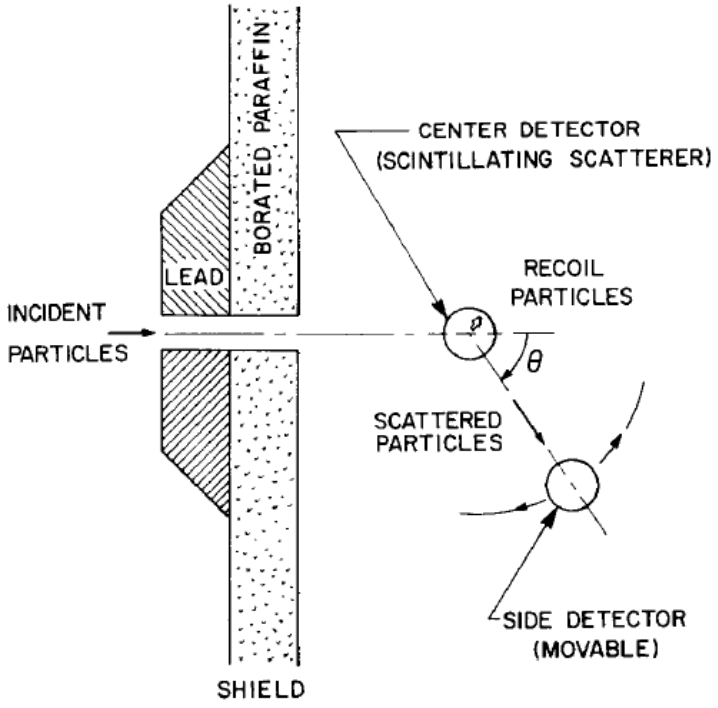

Figure 3.2: Illustration from Smith et al. showing the experimental configuration of an indirect method setup involving coincidences between a detector of interest irradiated with a mono-energetic beam allowing the calculation of recoiling particle energies within the detector. By moving the secondary detector and exploiting many nuclear reactions to produce a series of measurements for independent recoil energies, Smith et al. covered a large energy range and investigated a large collection of materials. Reproduced with permission from Elsevier [19].

the primary detector whose energy can be calculated from kinematics. For a given incident mono-energetic flux of either particle type, a single-angle scattering event leads to a single recoil energy in the primary detector. To overcome this, Smith et al. [19] both uses many nuclear reactions and relocates the secondary detector to sample different scattering angles.

The indirect method has evolved in a number of ways to overcome potential issues with the system described by Smith et al. [19] First, later authors [20] add a stationary secondary detector that enables tracking the long term gain drift of the photomultiplier tube coupled to the sample of interest while the non-stationary detector is being moved. With only a single non-stationary detector present, this potential drift would be undetectable. Additional measurements make use of many secondary detectors. A recent example of this comes from Yoshida et al. [21], which employs 7 secondary detectors to cover the full range of possible recoil angles for an n-p scattering reaction with the highest angle observing only background. This setup allowed the authors to cover proton recoil energies from 400 keV to 10.5 MeV without moving detectors, although the coverage was sparse.

Although time of flight between detectors has been used as a background rejection criteria for indirect methods from the beginning, very recent work by Iwanowska et al. [22] exploited this as a means of calculating the proton recoil energy using a mono-energetic neutron source. One of the more interesting earlier examples of a similar idea comes from the early 1980s where Galloway et al. [23] used a mix of direct methods and edge characterization methods with a white neutron spectrum from an AmBe source. This allowed the author to select proton recoil energies in a primary detector and obtain quasi-monoenergetic response functions from the secondary time of flight detectors.

The primary issue with indirect methods is one of efficiency. The detection efficiency of a system designed to produce an indirect light yield measurement (with each angle providing an individual data point) is orders of magnitude smaller than experiments involving a single detector in an edge characterization approach. The precision of the measurement is inversely related to this efficiency. As secondary flight paths get longer or secondary detectors get smaller, the angular variance is reduced but so is the efficiency. To maintain a reasonable precision, this requires long dwell times on accelerators capable of generating mono-energetic neutron beams of a variety of energies or machines capable of generating very high fluxes. Again, using many secondary detectors can help assuage this. The other issue is the sparsity of the data points collected with indirect methods. With a mono-energetic source and a single angle producing a recoil spectrum for a single energy, employment of many angles and reactions is required to generate data across a range of energies.

3.4 Summary and Discussion

Although light yield has been measured in a variety of ways over the last seven decades, little consensus in the literature exists for even the most commonly measured materials. For example, a summary regarding the recent work to establish the light yield of EJ309 shown by Bai et. al. [18] and reproduced here in Figure 3.3 shows a dramatic variance in the result

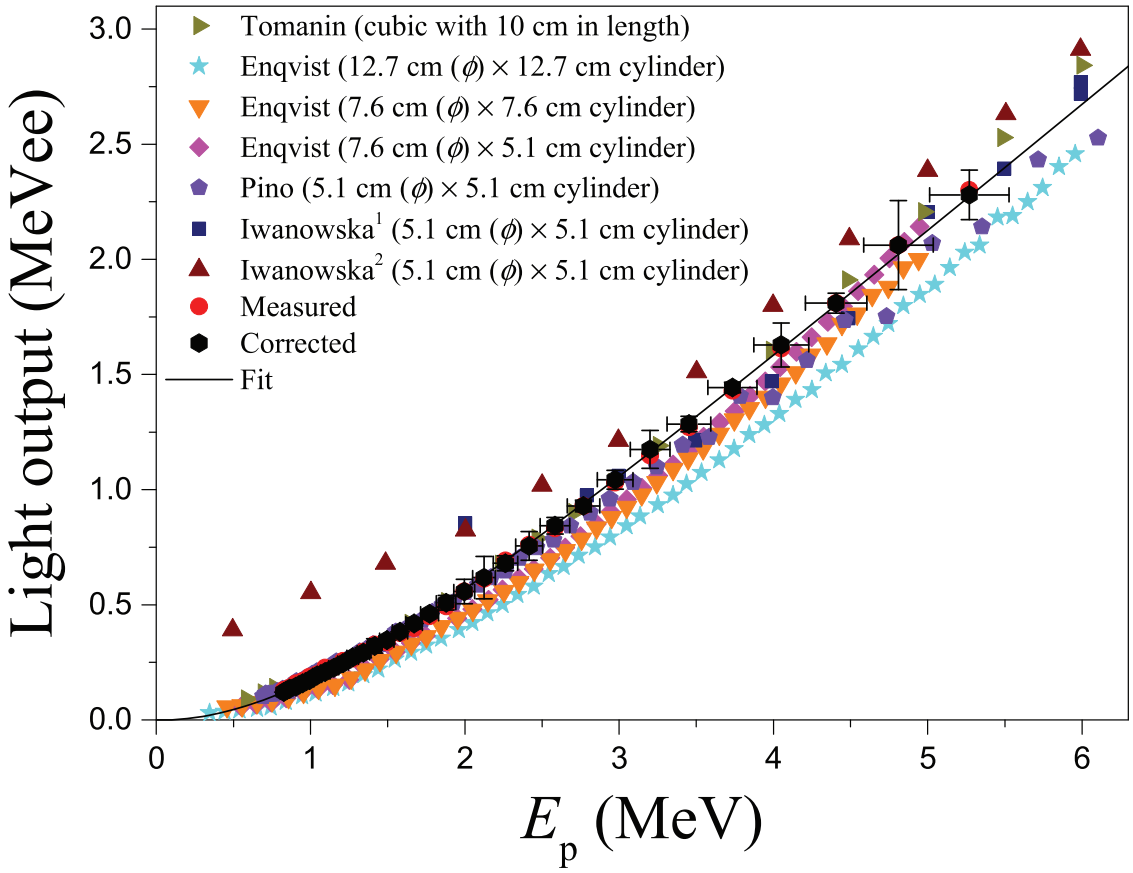

Figure 3.3: Summary of the recent measurements conducted on EJ309 by Bai et al. [18] including data from [1, 16, 22, 24, 25] shows a dramatic variance in the result of attempts to measure the proton light yield. Reproduced with permission from Elsevier.

from many authors. It is worth noting that the data presented in Enqvist et al. [16] for 7.62 mm detectors has been re-interpreted by Norsworthy et al. [26] and shows dramatically different results. The status of the literature for NE-213 is not more consistent despite its long history of use and a litany of measurements. Although the work by Verbinski [14] is commonly referenced, it is common to misinterpret the light unit used in the original paper leading to perhaps more confusion. This has led to the conclusion that the light output of detection system need to be characterized for any detector that an experimenter would like to use. For example, Scherzinger et al. [17] states:

> It would seem that a dedicated measurement of the recoil-proton scintillation-light yield must be made on a case-by-case basis to obtain the best accuracy in precision neutron measurements.

This is an undesirable outcome given the number of detectors deployed for which this quantity is important. This is especially true considering the challenge of measuring this quantity over the energy range relevant for the majority of applications. Benchtop experiments such as those employed by Bai et al. [18] and Scherzinger et al. [17] cover proton recoil energy ranges from $\sim 1-6$ MeV. A much more desirable outcome would be a measurement relevant for the scintillator material itself along with standardized, readily-approachable benchtop methods for characterizing the system response.

Chapter 4

Methods

4.1 Detectors and Acquisition

4.1.1 Neutron Detectors

Two types of neutron detectors were used in this work. They differ in the type of scintillator material used as the detection medium, either Eljen 301 (EJ301) or Eljen 309 (EJ309). The EJ301 scintillator is an NE-213 equivalent that has a long history of use in the community. The EJ309 scintillator is a newer addition prompting many recent measurements. A table of the materials properties supplied by Eljen Technology for the materials tested here is given in Table 4.1. Both are right cylindrical volumes contained in an aluminum housing coupled to the front face of a Hamamatsu 1949-50 photomultiplier assembly through a thin acrylic window and a thin layer of optical grease. The housings are airtight and the materials were bubbled with nitrogen upon construction. The Hamamatsu 1949-50 photomultiplier tubes have borosilicate windows backed by a bialkali photocathode. The dynodes are linear focused, which provide good temporal response and a high peak current where space-charge-induced non-linearities become an issue. The Hamamatsu 1949-50 requires a negative bias with a maximum of -3000 V; thus interactions in the scintillator lead to negative pulses.

Material	EJ301	EJ309
Commercial Equivalents	Nuclear Enterprise NE213 Saint-Gobain Crystals BC-501A	none
Scintillation Efficiency (photons / 1 MeV e^-)	12,000	12,300
Maximum Emission Wavelength (nm)	425	424
Specific Gravity	0.874	0.959

Table 4.1: Materials information for scintillators tested.

4.1.2 Data Acquisition

The data for this work were collected using a CAEN v1730 500 MS/s waveform digitizer housed in a CAEN NV8020 mixed NIM/VME crate. The communications were handled by a CAEN v1718 VME-USB 2.0 bridge which has a 30 MB/s bandwidth limitation. The digitizer has a 2 V peak-to-peak input limitation with a software-selectable DC offset. Since the detectors used are negatively biased, the offset was set so that the baseline averaged 97% percent the full scale range. The v1730 includes the optional DPP-PSD firmware which provides several onboard pulse processing algorithms handled in a field programmable gate array. Given the nature of the work, it was preferential to store full waveforms on disk for post-processing. The test software supplied with the system, DPP-PSD Control Software, provides limited flexibility for data storage formats and mixed mode write-out; Storing FPGA-derived quantities as well as waveforms is not possible. As a result, the DPP-PSD Control Software was converted to be C++ compatible and code was injected in the software suite with the desired additional functionality.

The supplied data format for writing out waveforms in the DPP-PSD Control Software is column-based ASCII with individual files for each active channel. It is preferential when writing waveforms to do so in a compressed format. It was also preferential to store FPGA derived quantities along with the waveforms. This was accomplished by linking the CERN ROOT data analysis framework to leverage the event-wise data storage capabilities of the ROOT TTree class [27]. An *IndividualDigitalDaqEvent* container class was developed to store an event for a single channel of the digitizer. The class contains an integer to reference the number of samples recorded, two 32-bit unsigned integers to store the trigger time tag supplied by the FPGA as well as the user selected 'extras word' from the FPGA, and a vector of 16-bit unsigned integers to store the waveform samples. When multiple channels are active, each channel gets a unique tree in a shared ROOT file. A reduction of nearly a factor of 20 was achieved storing the data in this format as compared to the original ASCII format.

Additionally, shared memory parallelism was introduced via OpenMP to prevent the system from overflowing the V1730's onboard memory buffers during write-out. One thread handles the system control and data retrieval from the digitizer itself and storage of the data in a pre-allocated ring buffer of *IndividualDigitalDaqEvents*. A second thread follows the primary thread and handles the disk input/output (I/O). Synchronization is managed through atomic updates to state flags that allow the threads to communicate. The secondary thread managing I/O has the ability to stop the acquisition if it gets too far behind the main thread, as well as when the file reaches a specified file size. This modification allows the system to operate up to the bandwidth limit of the USB 2.0 interface without the risk of data loss.

A post-processing base class, *SCDigitalDaqPostProcessing*, was also developed that leverages the ROOT data analysis framework to provides functionality to load the ROOT TTrees into memory and retrieve events, plot waveforms, plot a series of waveforms in a movie (analogous to a replay function for an oscilloscope), and test signal processing algorithm

functionality.

One of the FPGA algorithms that is used in the analysis is CAEN's digital constant fraction discrimination, which is used to report a global time since the beginning of the acquisition. The signal processing algorithm mixes the signal with a time delayed attenuated version of itself creating a bi-polar signal with a zero crossing time proportional to a fractional height of a pulse. This zero crossing time is interpolated between samples to provide an estimate of the pulse arrival time with greater resolution than the sampling frequency of the digitizer [28].

4.2 Digital Pulse Processing

This section provides details of the basic signal processing algorithms used to reduce the collected waveform data into pulse integral and pulse shape information. The first requirement in the pulse processing chain is to estimate the zero point of the recorded waveforms. This was accomplished by creating a digital implementation of the algorithm outlined in Ref. [29]. The baseline estimation algorithm is designed to obviate the potential influence of the tail of a previous pulse on the estimate of the waveform under consideration. The algorithm has a state based on its previous use. That is, it first estimates the baseline based on the beginning of the collected waveform by calculating the average, $\overline{x}$, of a user-specified number of samples. It then compares the current baseline estimate to a running average, $\overline{X}$, over a user-specified number of waveforms, n. If the current estimate is outside of a threshold, the baseline returned is the running average. If the baseline is within the threshold, the baseline estimated from the average of the samples is used and the running average is updated. The update to the running average is specified as

$$\overline{X}_{i+1} = \overline{X}_i - \frac{\overline{X}_i}{n} + \frac{\overline{x}}{n} \tag{4.1}$$

for the ith iteration. Since the detector signals are negative, the signal must also be inverted. The baseline subtraction and inversion is handled simultaneously on a sample-by-sample basis and a corrected sample is specified as

$$W_k = -s_k + C_i, \tag{4.2}$$

where C_i is either $\overline{x}$ or $\overline{X}_i$ depending on the whether or not $\overline{x}$ was within the threshold, s_k is the kth sample of the original waveform, and W_k is kth sample of the baseline-corrected trace.

Since it is both useful in considering multiple integration lengths and in pulse shape discrimination algorithms, a cumulative distribution function is developed. To accomplish this, the start sample of the event was identified, s, by testing for the first event above a specified threshold and then a cumulative distribution function (CDF_W) was developed.

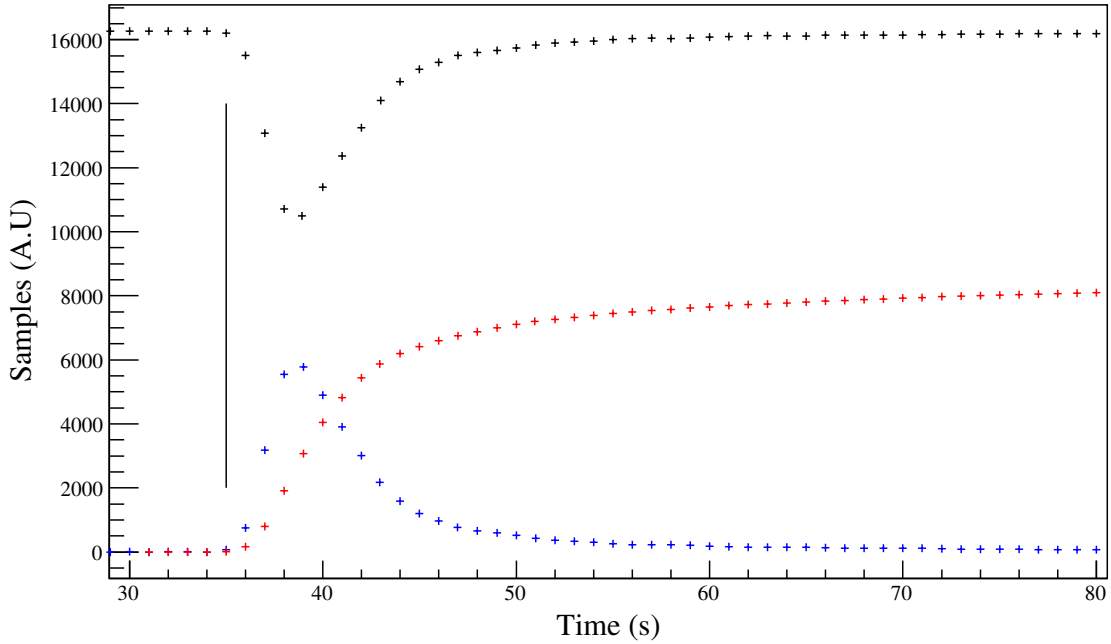

Figure 4.1: Schematic illustrating the main steps in the digital pulse processing chain. The black points represent the samples of an example waveform recorded from the acquisition. The blue points represent the baseline-corrected and inverted result, the vertical black line represents the determined start sample, and the red points represent the CDF from which the integral and pulse shape metric are obtained. The CDF has been arbitrarily scaled to fit the range of the other quantities.

The lth element of the cumulative distribution function is specified using

$$CDF_{W_l} = \sum_{k=s}^{l} W_k. \tag{4.3}$$

So for a specified integration length, t, the pulse integral is given as

$$I(t) = CDF_{W_{k=t}}. \tag{4.4}$$

An example of an original waveform, a baseline-subtracted and inverted waveform, the start sample determination, and the cumulative distribution function are shown in Figure 4.1.

For pulse shape discrimination, the time difference between the time at which the pulse integral was at 10% of its maximum value and the time at which it was at 90% of its maximum value was used as characteristic of the pulse shape. To accomplish this, the maximum of the CDF_W is identified. Then the samples bracketing the 90% and 10% values of the CDF are identified. The time at each point is determined as the linear interpolation between the two samples bracketing the level of interest, and the pulse shape metric is the difference in the interpolated times between the two points.

4.3 Calibration of Scintillator Light in MeVee

A common working unit for the light space of organic scintillators that has been developed is MeVee, or MeV electron energy equivalent. Light units recorded from any particles are related to the equivalent electron energy that would produce the same amount of light. There are several motivations for using this unit. First, a large number of common γ-ray sources are readily available for calibration of γ-ray detectors. Second, the response to electrons is linear in organic scintillators allowing for interpolation and extrapolation between and beyond the γ-ray source energies used. Third, working in a space that can be easily related between labs allows comparison of results between research activities. The goal of any calibration attempt using this unit is to find a map between the measured output of a system and the light a specific energy electron would produce. This work attempts to find a linear map of the form:

$$L(x) = a * x + b, \tag{4.5}$$

where L is the light in MeVee, x is the pulse integral in arbitrary units, a is the linearity between them, and b accounts for any potential offsets in the scale.

4.3.1 Foundational Work

Much of the initial work on measuring scintillator response relies on characterization of the edge of a pulse integral distribution observed when using mono-energetic or bi-energetic γ-rays. The means of characterizing the edge varied dramatically among the early work leading to an approximate difference in their light spaces of 5% [30]. Dietze and Klein [30] came to this conclusion through studying comparisons of Monte Carlo models of the electron energy deposition in organic scintillators following γ-ray irradiation and comparing them to empirical spectra. From this, a table was developed for estimation of the underlying Compton edge for a series of detectors sizes and observed resolutions. They note that, “In any case the best analysis is obtained by comparing the experimental pulse height spectra with properly folded Monte Carlo distributions." There is no recommendation on best practices for making this comparison. This works takes the concepts introduced in this paper and builds on them in an attempt to obtain reliable well-characterized MeVee calibrations.

4.3.2 Detector Resolution

Following the work of Dietze [30], the detector resolution function is treated as a normal distribution with a width dependent on the light generated. The relative full width at half maximum of the distribution is given as

$$\frac{\Delta L}{L} = \left(E_c^2 + \frac{E_1^2}{L} + \frac{E_2^2}{L^2} \right)^{\frac{1}{2}}. \tag{4.6}$$

These contributions to the resolution come from: the variance in the interaction position within the detector and associated photon losses, E_c; the statistical variance due to the light

conversion and amplification, E_1; and electronic noise contributions from the amplification, acquisition and readout, E_2. To make a comparison between Monte Carlo simulation output and observed data, the Monte Carlo result must be convolved with this resolution function.

4.3.3 γ Calibration Framework

To approach the systematization of the comparison between the Monte Carlo model of energy deposition for known γ-ray spectra and the observed spectra, a software framework was developed that builds on the work of Dietze [30]. The γ Calibration Framework (γCF) is designed to facilitate a χ^2 minimization of a set of parameters of interest with a comparison between multiple independently-collected source spectra with Monte Carlo models of the anticipated energy deposition simultaneously. It is a modular C++ code with dependence on the ROOT data analysis framework [27]. It leverages ROOT's minimization algorithms and graphical user interface (GUI) and couples them to algorithms developed to facilitate the comparison. The major components of the framework include: histogram manipulation algorithms for conditioning the input simulations and data, visualization and parameter modification GUI elements, and interface functions to allow access to the ROOT minimization algorithms to change their behavior.

The interface for the framework comes in the form of an abstract base class, *GammaScintCalibration*, and an inherited class, *MultiDataScintCalibration*. There is an additional inherited class, *SumScintCalibration*, used for considering spectra with multiple γ-ray sources present that is similar in function. The *MultiDataScintCalibration* branch was used for the experiment discussed here, so the discussion will focus on it.

The base class *GammaScintCalibration* provides part of the user interface and defines an interface for the GUI elements. The GUI elements include ROOT's triple sliders for setting individual parameters and their limits, double sliders for setting the range of consideration for each individual histogram, and graphical windows showing the current state of the model compared to the data as well as the residuals. The base class also contains the data structures for storing the references to the simulation data, experimental spectra, parameter values, parameter limits, and parameter names. The base class requires inheriting classes to define algorithms to draw the state of the comparison, return a χ^2 value for the current parameter set, and update the GUI elements.

The *MultiDataScintCalibration* class implementation has several methods of construction. The construction methods generally require vectors of pointers to histograms. The first vector contains pointers to ROOT histograms of the observed data and the second contains pointers to ROOT histograms of the simulations. An exception to this is when considering small samples. The normal geometrical complications requiring the Monte Carlo of what is primarily Compton Scattering can be replaced by a calculated Klein-Nishina distribution. A constructor exists to support this. It takes a single vector of pointers to the histograms of the data and a vector of strings corresponding to the name of the calibration sources used. Additional options on construction are either passing a set of starting parameters for the model to the constructor or letting the package attempt initial rough parameter estimates

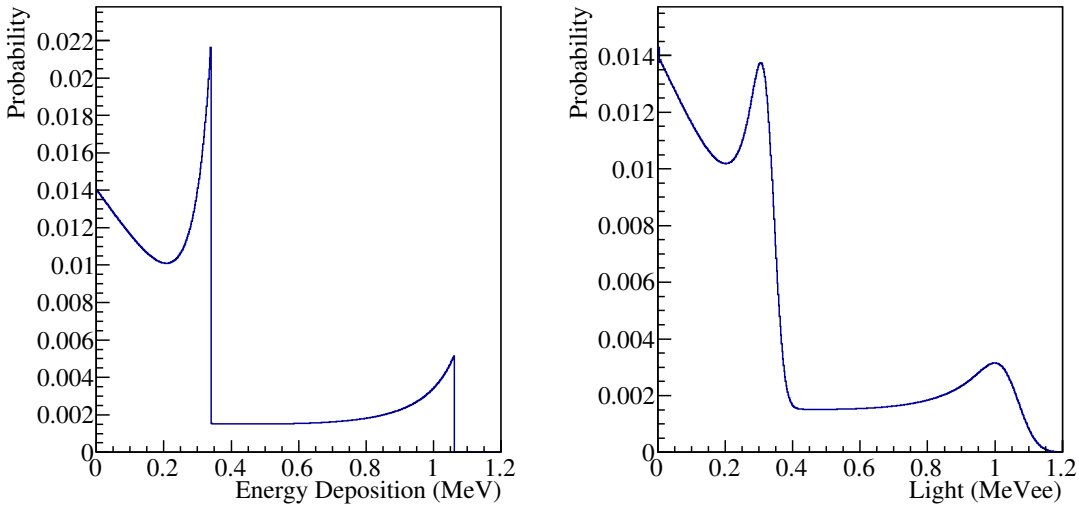

Figure 4.2: Left: The idealized response of an organic scintillator to a ^{22}Na γ-ray source. Right: The result of convolving the idealized spectrum with a realistic set of parameters for the resolution function.

as well as specification of whether or not to consider additional empirical backgrounds in the spectra using power law functions. Upon construction, the simulation inputs are normalized to be treated as probability distribution functions.

The full set of the parameters for the comparison consist of five parameters that are applied to all histograms considered, which includes the primary parameters of interest and several nuisance parameters. The primary parameters are a, b, E_c, E_1, and E_2 coming from Eqs. 4.5 and 4.6. Several nuisance parameters also exist which are applied to the histograms individually. The number of nuisance parameters depends on the operational mode. Depending on the user selected operation mode, there is either one nuisance parameter per source spectrum, a scaler for the overall magnitude of the model, or three, the same magnitude scaler as well as a magnitude scaler and exponent for an empirically-observed power law background contribution.

The construction of the model for an individual spectrum in the χ^2 comparison with a given set of parameters begins by duplicating the histogram of the input data, clearing all the contents, and scaling the range axis using a and b creating a separate histogram with identical bin structure and a proposed mapping between observed data and light in MeVee. This histogram is then filled with the simulation data accounting for the change in bin structure from the stored simulation data. Next, the histogram is convolved with the resolution function given in Eq. 4.6. This is the most computationally complex operation in the model construction, and thus required optimization. Since the resolution function is heteroskedastic, normal Fourier transform-based fast convolution methods are not applicable as there is no singular convolution kernel of which to take the Fourier transform.

A discrete fast convolution algorithm was developed with the following specification. The resolution or convolution kernel, $r(L, \mu_L)$, is taken to be normal with a standard deviation that varies as a function of its centroid, i.e.,

$$r(L, \mu_L) = \frac{1}{\sqrt{2\pi}\sigma(\mu_L)} e^{-\left(\frac{1}{2}\frac{L-\mu_L}{\sigma(\mu_L)}^2\right)}, \tag{4.7}$$

where L is the light in MeVee, μ_L is the centroid of the distribution in MeVee, and $\sigma(L)$ is obtained from Equation 4.6. The ith bin of the convolution can be described discretely as

$$S_i = \sum_{k=0}^{N} s_k r(L_i, L_k), \tag{4.8}$$

where S_i is the bin content of the convolved result in the ith bin, s is the original bin content in the kth bin of the original histogram, L_i is the light value corresponding to the ith bin, and N is the total number of bins considered. This mathematical specification implies an N^2 algorithm, where each bin requires a loop over all of the original bins. Instead the implementation developed here reduces this to an $N \times m$ algorithm, where m is the width of the kernel in bins, by reversing the loop order so that for each original bin, one loops over $\pm 6\sigma$ bins in the resultant histogram and adds the integral of the resolution function over the resultant bin multiplied by the original bin content. Due to the heteroskedasticity of the resolution function, m varies in size but is in general orders of magnitude smaller than N, vastly reducing the computational complexity of the convolution. Although the algorithm is not perfectly conservative of the original number of counts in the simulation histogram, the loss is less than 1%. A plot showing the results of convolving an idealized input of the response of a ^{22}Na γ-ray source is shown in Figure 4.2.

Continuing the model development, the resultant convolved simulation is then scaled by a constant value to adjust the overall scale. Lastly, and optionally, the construction of the model is finalized by the addition of a background term. This can either be an experimentally measured background spectrum or an empirical power law function. In the latter case, a single bin of the model, M_i, used for comparison with the experimentally observed spectra is given by:

$$M_i = c_1 S_i + c_2 L_i^p, \tag{4.9}$$

where c_1 and c_2 are free parameters in the model, S_i is ith bin of the convolved simulation result given by Eq. 4.8, L_i is the light corresponding to the ith bin, and p is a free power law parameter.

The χ^2 comparison used as the objective function in the minimization is calculated for more than one histogram, i.e.,

$$\chi^2 = \sum_{l=0}^{M} \sum_{i=R_{l-}}^{R_{l+}} \left(\frac{D_{li} - M_{li}^2}{\sigma_{D_{li}}} \right), \tag{4.10}$$

where M is the total number of histograms considered, R_{l-} is the bin corresponding to the lower end of the set range for the lth histogram, R_{l+} is the bin corresponding to the upper end of the set range for the lth histgoram, D_{li} is the value in the ith bin of the lth experimental histogram, M_{li}, is the value in the ith bin of the lth constructed model, and $\sigma_{D_{li}}$ is the statistical uncertainty on the value in the ith bin of the lth experimental histogram. The parameter search is managed by the ROOT minimization algorithms. Once the search is complete, the resultant parameters are set in the base class, all the GUI elements are updated as needed, and the state of the class is redrawn to show the result. Once a statistically valid minimum has been found, the covariance matrix for the parameters can be obtained for a given subset of parameters.

4.4 Neutron Time of Flight

Neutron time of flight provides a means of determining on an event-by-event basis the energy of a neutron in a nuclear physics experiment. It requires the establishment of both a flight path and a flight time. With those two quantities, the relativistic energy-time relation can be used to calculate the neutron energy. The relativistic energy-time relation is

$$E_n = (\gamma - 1)M_n c^2, \tag{4.11}$$

where M_n is the neutron mass, c is the speed of light, and

$$\gamma = \frac{1}{\sqrt{1 - \frac{(L/t)^2}{c^2}}}, \tag{4.12}$$

where L is the flight path and t is the transit time.

4.5 Double Time of Flight Light Yield Measurements

Indirect methods have generally been conducted using monoenergetic incident neutrons allowing the calculation of proton energy from the known incident neutron energy and scattering angle. Few exceptions to this exist where broad spectrum neutrons from a continuous source were employed and the time of flight between detectors was used to calculate the recoil proton energy. Outside of that, time of flight methods have been used primarily for rejection criteria. Introduced here is a method for exploiting time of flight in conjunction with a pulsed broad spectrum neutron beam to determine the energy of both the incoming neutron and outgoing neutron leading to an overdetermined system that allows calculation of proton energies in multiple ways. This method allows for the continuous measurement of the light yield relation over a broad spectrum of energies. Schematically, the experimental setup looks similar to the setup shown in Figure 3.2. Using a pulse broad spectrum incident source introduces several complexities as well as advantages. For the purpose of this work,

the detector in beam that is the subject of the the light yield measurement will be referred to as the target detector, and the secondary detector out of beam will be referred to as the scatter detector.

One of the first things to consider in this method is the means of establishing proton energy. There are three primary ways in which the proton energy can be calculated. The first is to establish the neutron energy using the time of flight from the source location to target detector, and then use the known scattering angle and n-p elastic scattering kinematics to calculate the proton energy. This is described in Eq. 2.4. The second is to obtain the exit neutron energy from the time of flight between the detectors and then use the known scattering angle and kinematics. This is described in Eq. 2.5. The third is to use the difference in the energies established using time of flight, described in Eq. 2.6. The experimenter is left to assess the best means of determination based on the anticipated uncertainty for the specific methods.

Of particular interest when using this method is the ability to recover a clean incident time of flight when the pulsed source has a pulse period that is shorter than the anticipated flight times of the incident neutrons. This would lead to an ambiguous incident time of flight measurement. At any given time, multiple beam pulses may have led to an observed event. In this case, the incident time of flight would be uncertain by an integer number of pulse periods. With the overdetermined system, if desirable, the incoming time of flight can be established using the exit time of flight. In this situation, the incoming time of flight would be uncertain by an integer number multiplied by the period of the pulsed source. Assuming phase stability, an expected incoming time of flight, t_{expInc}, can be calculated as:

$$t_{expInc} = \frac{L_{inc}}{c\sqrt{1 - \frac{M_n}{M_n + E' \cos^{-2}(\theta)}}}, \tag{4.13}$$

where L_{inc} is the incoming flight path, c is the speed of light, M_n is the mass of the neutron in MeV, E' is the scattered neutron energy, and θ is the scattering angle. From this, the integer offset in the measured time of flight can be obtained using:

$$n = ||\frac{t_{expInc} - t_m}{T}||, \tag{4.14}$$

where t_m is the measured time of flight and T is the pulse period of the source. The correct time of flight is then given as

$$t_{inc} = t_m + n * T. \tag{4.15}$$

One notable change in the measurement obtained using an indirect method with a broad spectrum pulsed source is the continuous nature of the result. Compared to a monoenergetic incident beam, a given angle no longer observes a single proton energy, but instead a distribution of proton energies based both on the spectrum of the incident beam and the scattering angle. This enables a continuous measurement of the relation across a broad spectrum of energies with the ability to approach the characterization of the light yield in a variety of ways. If this idea is coupled with multiple detectors with overlapping resultant energies, a

strong check of the systematics of the result can be estimated by comparing the results from different angles that lead to similar energetic solutions. Given that any use of secondary detectors involves leaving them stationary, gain drifts can be tracked by examining the data as a function of time.

The relative efficiency between the target and scatter detectors provides a fundamental physics limit on the count rate for this method, as well as any other indirect method. With a strong enough pulsed source, the upper bound on the incident flux is the point where pulse pile-up is a dominant fraction of the events occurring in the target detector. At this point, establishing outgoing time of flight becomes intractable as it is unclear which of the primary events in the target detector the time should be associated with. If an experiment is run just under this limit, then the real coincident detection rate is set strictly based on the probability of detecting a neutron correlated with an event in the target detector.

Chapter 5

Experimental Configuration

This chapter will detail the experimental configuration that established the double time of flight method outlined in Section 4.5, while measuring properties of two materials of interest– EJ301 and EJ309–commercially available liquid scintillators available from Eljen Technology discussed in Section 4.1.1. First, the pulsed source used in this work will be discussed. Next, the specifics of the geometry for the scattering array will be detailed. Finally, the specific configuration of the data acquisition described in Section 4.1.2 will be discussed.

5.1 Deuteron Breakup Neutron Beam

The neutron source for this work was a high flux broad spectrum deuteron-breakup neutron beam developed at the 88-Inch Cyclotron at Lawrence Berkeley National Laboratory. The 88-Inch Cyclotron is a sector-focused cyclotron capable of accelerating a broad range of particles to high energies. For neutron production, a deuterium plasma is developed in the advanced electron cyclotron resonance ion source and extracted into the injection line of the cyclotron using a series of bending magnets. The deuterons are then accelerated to high energies. For the experiment detailed here, they leave the cyclotron at 33 MeV. After extraction, the deuterons are focused onto a thick, liquid-cooled, tantalum target. The energetic deuterons are slowed in the target with a portion of them forming neutrons from deuteron breakup. As the proton is charged, it is readily stopped in the breakup target. The neutron continues along the beamline path. This also leads to the production of a large number of high energy γ rays at the time of the breakup, which is important for calibrations. The breakup target is located $\sim$ 6.5 m from the experimental area, and is separated by a large amount of shielding made up of a combination of concrete walls, sand bags, and lead. The first $\sim$ 6 m of this flight path is an aluminum beamline under high vacuum. At the end is a beam box is a Kapton window that the neutrons pass through before encountering a wall with a 10-cm-diameter hole. The result is a collimated 10-cm open-air neutron beam in the experimental area where detectors can be place. A diagram of the experimental area is shown in Figure 5.1.

The neutron beam produced using deuteron breakup has a broad energy spectrum with

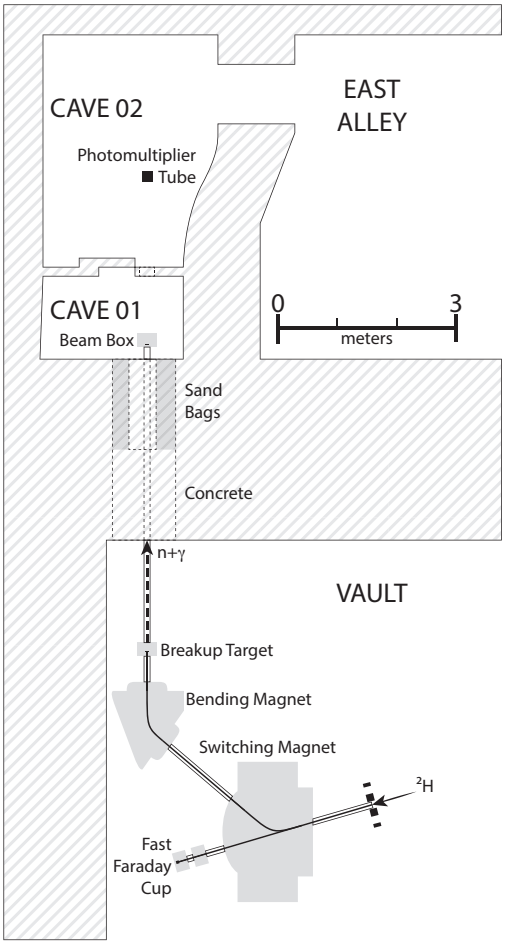

Figure 5.1: Diagram of the experimental area at the 88-Inch Cyclotron

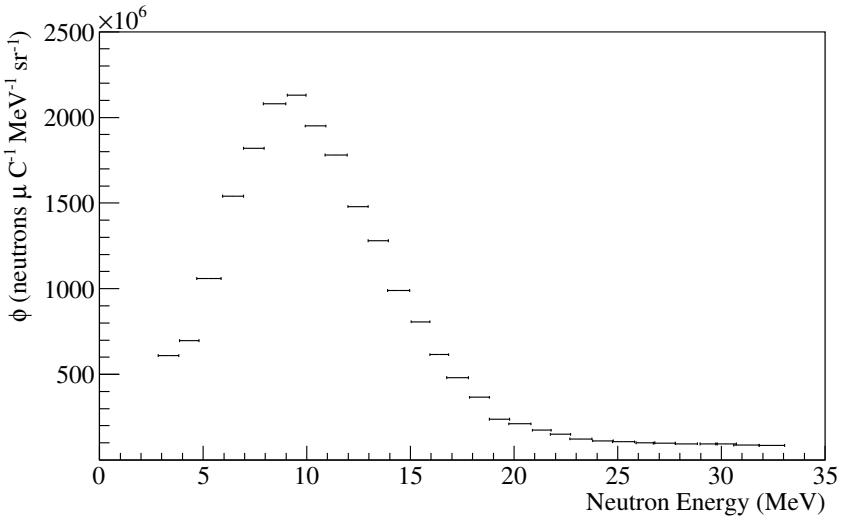

Figure 5.2: The anticipated flux from a 33 MeV deuteron breakup neutron beam in neutrons per μC per MeV per steradian presented as reported by Meulders et al. [32]

an upper energy limit slightly above the incident deuteron energy. The anticipated spectrum for the beam energy and breakup target used in this work is shown in Figure 5.2. Additional flux measurements of the 88-Inch Cyclotron deuteron-breakup neutron source for different beam energies are available in Ref. [31]. With the anticipated flux shown in Figure 5.2, using a 1 μA beam current would lead to an approximate count rate in the primary detector of 100 kHz, not including background events or γ-ray events. This means that the fundamental rate limit of the double time of flight method discussed in Chapter 4 Section 4.5 should be easily reached with this combination of beam energy and target material. Considering this energy spectrum, flight times on an incoming flight path of 700 cm range from ∼80 ns for the highest energy particles to ∼500 ns for a 1-MeV neutron. The 88-Inch Cyclotron requires an operating frequency of 9.0014 MHz to accelerate deuterons to 33 MeV meaning that the pulse period is 111.094 ns. This in turn leads to a temporal overlap where, for example, a 1-MeV neutron has a flight time an integer multiple pulse periods greater than 1.6 MeV, 3.2 MeV, and 8.7 MeV neutrons. Thus, the incoming time of flight reconstruction outlined in Section 4.5 was required. This spectrum will be transformed in energy space following an n-p scattering event so considerations of flight time between detectors requires knowledge of the specific angles and flight paths.

5.2 Scintillator Array

The array of target and scatter detectors used for this experiment were all of the type described in Section 4.1.1. Two target detectors were placed in the beamline: one EJ309 and one EJ301. The target detectors were mounted on a custom designed vertical mount coupled

Figure 5.3: The detector array at the experimental area of the 88-Inch Cyclotron. On the left are the two target detectors mounted horizontally and a tertiary target not analyzed or discussed in this work. On the right are the six scattering detectors that observe the neutrons scatter out of the target detectors.

to a tripod. The mount allowed a minimal amount of additional material to be placed in the beam while ensuring the scintillating volume of the detectors was overfilled. The mount is shown in the left side of the image in Figure 5.3. The target detectors were biased to set the peak amplitude of the observations of an AmBe neutron source on an oscilloscope at one-quarter of the full scale range of the digitizer, allowing a nearly 20 MeVee full scale range. This corresponded to a bias of -1280 V for the EJ309 target detector and -1390 V for the EJ301 target detector. High voltage was managed by a CAEN NDT1470 power supply located outside of the cave. Six scatter detectors were employed with a scattering angle range covering 37 to 61.5 degrees. Two of the detectors, one EJ309 and one EJ301, used a mount identical to the targets and were centered in the other scatter detectors, which were all mounted horizontally on custom constructed mounts that coupled them to tripods. The arrangement is shown on the right hand side of Figure 5.3. The bias of the detectors was set to include the full scale range of the anticipated incident neutron energy following an n-p elastic scattering event in the target. This resulted in biases for the detectors, starting from the largest angle to the smallest, of -1575 V, -1480 V, -1430 V, -1400 V, -1430 V, and -1300 V. The voltage was managed by a combination of a CAEN ND471 power supply and the remaining two channels of the CAEN NDT1470.

The detector locations were established by imposing a right-handed coordinate system on the room with $(0, 0, 0)$ being the beamline center on the wall from which the beam enters the room. The beam direction was taken as positive x, the direction towards the scatter detectors was taken as positive y, leaving z as up in the vertical direction. The distance

Direction	Material	x (cm)	y (cm)	z (cm)	reference
up	EJ-301	79.8 ± 0.25	0.0 ± 0.1	0.2 ± 0.1	target 0
down	EJ-309	79.8 ± 0.25	0.0 ± 0.1	-0.1 ± 0.1	target 1
horizontal	EJ-309	124.3 ± 1	125.1 ± 1	0 ± 0.1	scatter 0
horizontal	EJ-309	144.2 ± 1	118.3 ± 1	0 ± 0.1	scatter 1
down	EJ-309	169.4 ± 1	108.55 ± 1	5.6 ± 0.25	scatter 2
up	EJ-301	169.4 ± 1	108.55 ± 1	0 ± 0.25	scatter 3
horizontal	EJ-309	173.9 ± 1	88.9 ± 1	0 ± 0.1	scatter 4
horizontal	EJ-309	181.1 ± 1	76.9 ± 1	0 ± 0.1	scatter 5

Table 5.1: Summary of detector locations and estimated uncertainties. The larger uncertainties in the x and y dimension for the scatter detector results from having to project their positions in that dimension to the floor. Alternitavely, the z dimensions were estimated from the horlzontal laser plane aligned with beamline center allowing for a much more accurate measurement.

from the breakup target to the zero point of this coordinate system was measured with a laser aligned along beamline center as 647.2 ± 0.2 cm. To measure the detectors a bi-plane self-leveling laser was aligned with the beam line center. A second right-angle bi-plane laser was used to establish the x dimensions by ensuring alignment of one of the planes with the beam line, and centering the other on the front face of the detector. The x distance was measured along the beamline and right-angle laser to the cross point of the other plane of the right-angle laser using a metric tape measure. The y dimension was then measured from the center of the front face of the detector along the laser located orthogonal to the beamline to the beamline. The z dimension was measured as the distance from the plane aligned with the beamline center to the center of the front face of the detector. The detector locations in this system and the estimated uncertainties on their locations are detailed in Table 5.1.

5.3 System Linearity Characterization

The establishment of the relative linearity of the system response was handled using a finite difference method similar to that outlined in Ref. [33] with differences here in the handling of the result. The primary concern was the potential for space charge effects in the photomultiplier tube leading to a decrease in the slope of the response at higher incident photon fluxes. This can result in a distortion in the observed waveform amplitudes. The space charge effect is temporally constrained to $1 - 2$ ns allowing characterization of peak amplitude distortions to be translated to a correction of a measured amplitude for a single sample of the waveform.

The finite difference method used required two controlled pulses of light similar to those observed from a scintillation event. Two avalanche pulse drivers were constructed based on the driver detailed in Ref. [34]. The drivers were coupled to LED Engine 405-nm UV

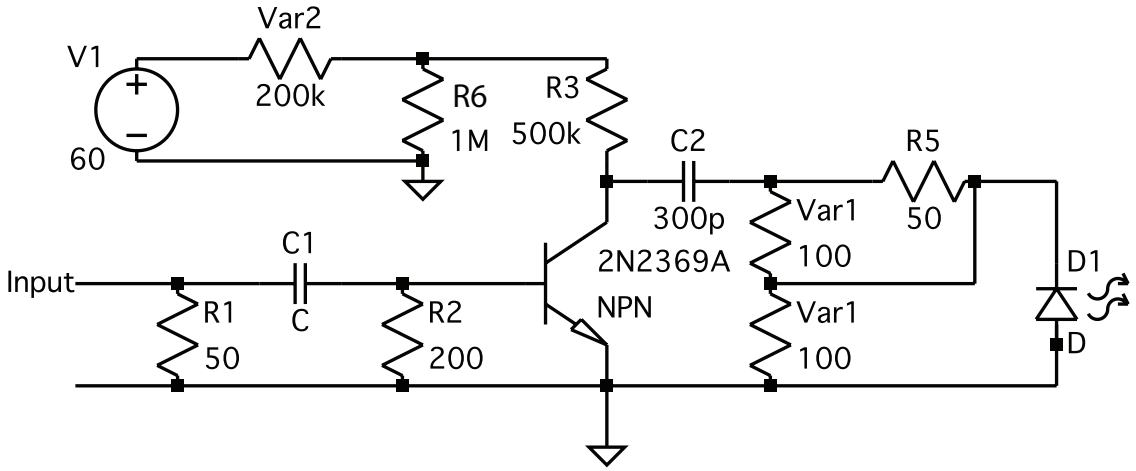

Figure 5.4: The avalanche pulse driver works by maintaining a voltage on capacitor C2 near the breakdown voltage of the 2n2369A NPN transistor. Any charge put into the base causes an electron avalanche in the NPN junction allowing it to transition into a conductive state on very short time scales resulting in pulse rise times on the order of ∼200 ps. This allows the capacitor to discharge quickly while R3 prevents the junction from pulling current continuously from the voltage source in a way that would cause it to overheat. The result is a large negative pulse on the right side of C2 pulling charge through the LED leading to a short light pulse. Var1 was used to make rough adjustments to the output of the LED. The voltage divider formed by Var1 and R6, where Var1 is actually a series of two potentiometers, allowed fine adjustments of the voltage stored on the capacitor that was used to make fine adjustments on the LED output. Once the capacitor is discharged, the NPN junction recovers and returns to a non-conductive state allowing the capacitor to slowly recharge.

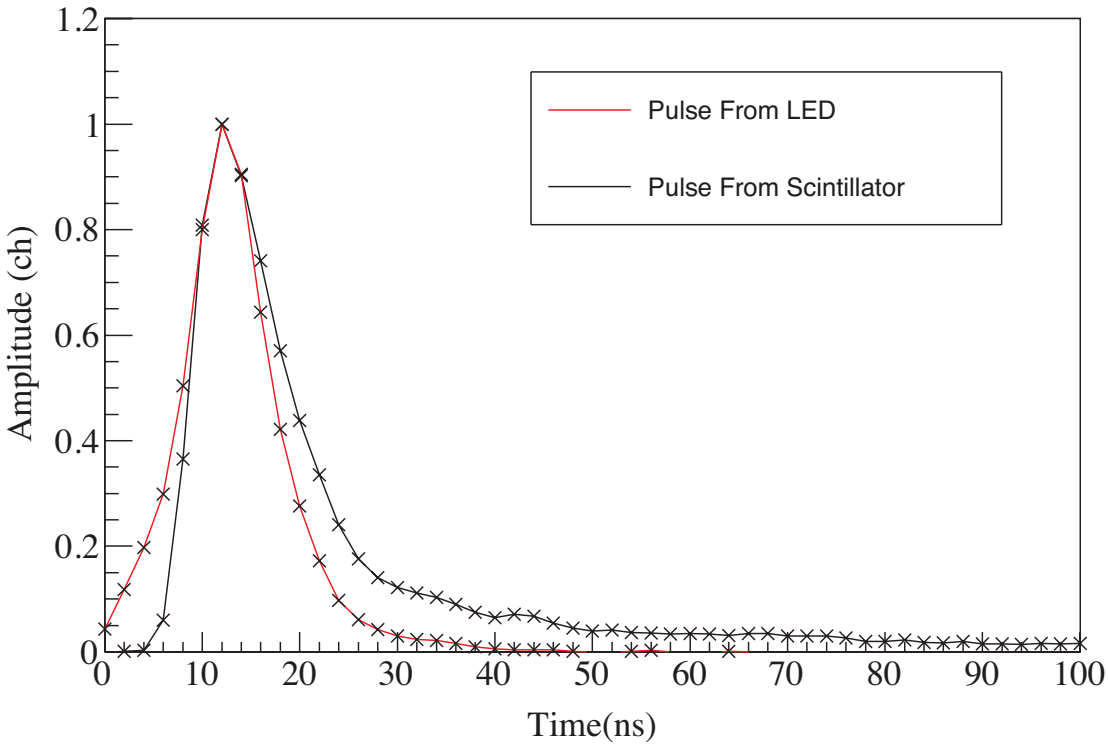

Figure 5.5: An event from the LED avalanche pulser compared to a scintillator event. The pulses were inverted and normalized by peak amplitude to compare their shape. The peak width is similar between them while there is a tailing from the scintillation event corresponding to the longer characteristic time of scintillation.

emitters. The avalanche pulse driver is detailed in Figure 5.4. The constructed system resulted in 405 nm pulses with a ∼7-ns full width at half maximum. A pulse from the LED is compared to the pulse from a scintillation event in Figure 5.5.

This approach to characterize linearity requires making adjustments to the amplitude of one of the LEDs, the 'variable pulse'. The other pulse, the 'delta pulse,' is left constant. The required sequence of pulses to make a finite difference estimate at a single location in the amplitude space requires three independent observations. First, the result of firing just the variable pulse is observed. Second, the result of firing just the delta pulse is observed. Third, the result of firing both of them simultaneously is observed. This allows construction of events where the response to the addition of a fixed quantity of light to a pulse at a given amplitude can be measured as a function of the input amplitude L:

$$\Delta r(L) = r(L + \delta L) - r(L) \tag{5.1}$$

where r is the response of the multiplier tube to a given light input, L. Since the absolute light is neither simple to obtain or necessary to linearize the system, the unit can have arbitrary units. A forward model is constructed to predict the differences measured using a trial

response function, $R(L)$. In this case, a fourth-order polynomial was used. To calculate the predicted measured difference, the location in the abstracted light space must be obtained from the measured quantities, $r(L)$ and $r(\delta L)$, by inverting $R(L)$. So, the trial response function allows prediction of the quantities:

$$L_t = R(r(L))^{-1} \tag{5.2}$$

and

$$\delta L_t = R(r(\delta L))^{-1}, \tag{5.3}$$

where L_t denotes the trial light. Then, the measured $\Delta r(L)$ can be predicted from the trial response as:

$$\Delta R(L) = R(L_t + \delta L_t) - R(L_t). \tag{5.4}$$

The parameters of the model prediction can then be modified in an iterative algorithm until the prediction of the measured differences is realized, allowing the calculation of the quantity that needs to be added to the measured amplitude to linearize the system.

To manage the pulsing, a logic sequence was constructed from delay generators and logic modules. The sequence was controlled by a waveform generator producing a square pulse logic signal at 750 Hz used as the master trigger for the sequence. This initial pulse was fed into a Logic Fan-in/Fan-out module to provide control for the individual LEDs. For the variable height pulse, this original signal was fed both into a CO4010 set in 'OR' mode and a delay gate generator set to produce to a pulse 666 μs following the initial signal. It was empirically observed that the pulse height of a pulse was dependent on the time since the last pulse was triggered. This effect was also amplitude dependent, with larger pulses resulting in larger differences. Since this behavior would render the finite difference estimates meaningless. So, both pulses to be triggered at fixed frequencies to obviate this effect. Although the source of the effect was not identified, it was not the result of an incomplete charge of the capacitor in the avalanche pulser as the period between pulses was much longer than the charging time of the capacitor. The delayed signal was fed into the same CO4010 module as the input to the delay gate so the variable pulse triggered at 1.5 kHz. The delta pulse was controlled in a similar manner, but the CO4010 module used to trigger it was fed signals from two delay generators, one set at 444 μs and the other set at 888 μs, to ensure it was triggered at a constant frequency of 2.25 kHz. Additionally, the output of the CO4010 module was fed into a second waveform generator to allow for accurate timing offsets. This allowed the fine tuning of the time between the pulses that were intended to come at the same time. To determine this fine time offset, a relatively large time offset of $\sim$20 ns was introduced on the second waveform generator. Then, the time difference between the variable and delta peak being observed by the bare photomultiplier tube was measured on an oscilloscope with 100 ps accuracy. The measurement of the time difference from the peaks was subtracted from the large time offset set on the waveform generator, thereby ensuring the light pulses from the two signals arrived at the same time. A block diagram of the logic modules and a representative timing diagram is shown in Figure 5.6.

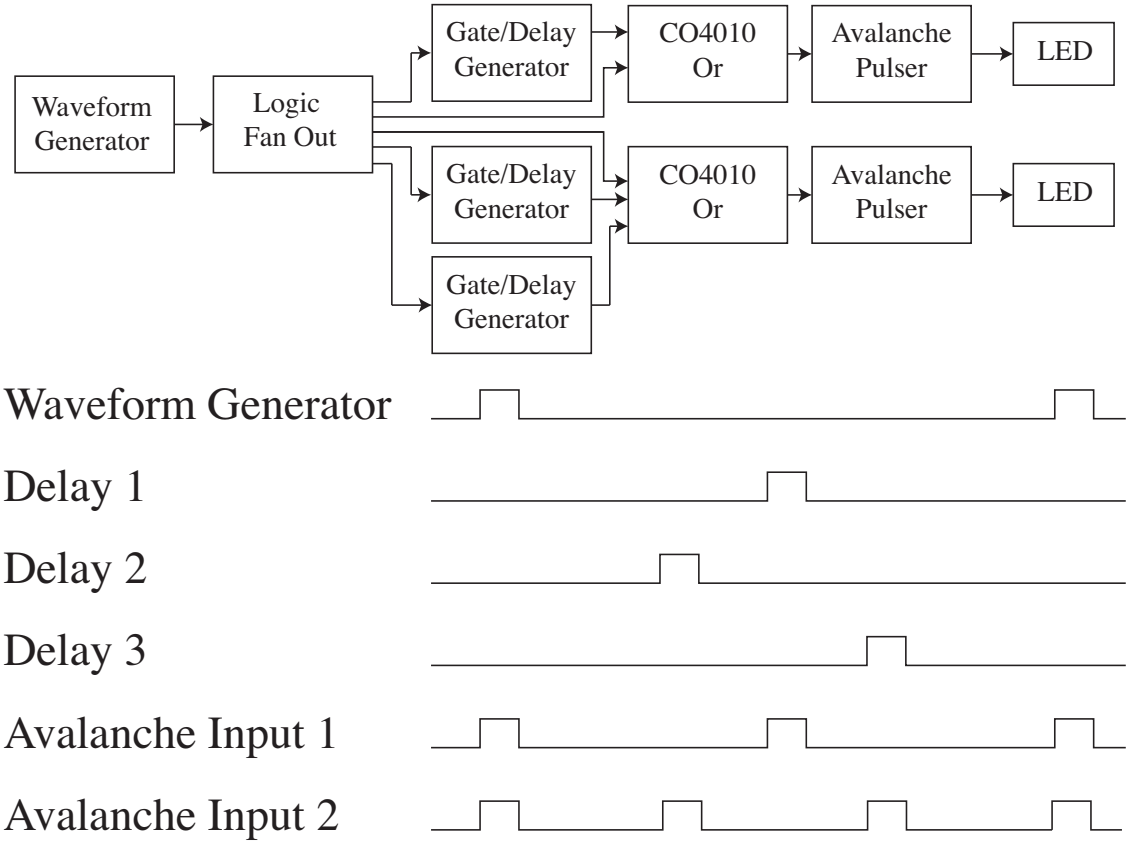

Figure 5.6: Block diagram of the control structure and resulting timing for performing finite difference linearity estimates of the phototubes used in the light yield measurements reported herein.

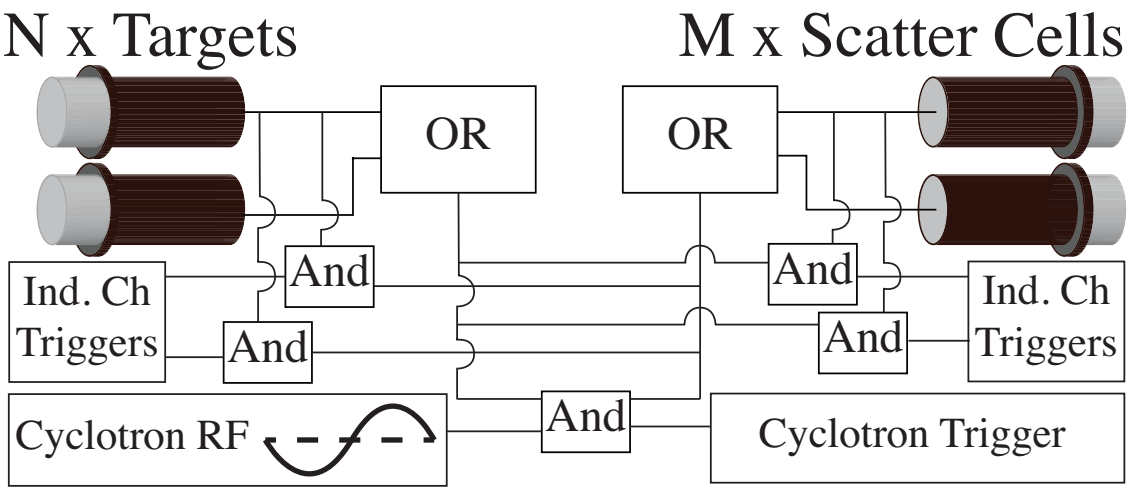

Figure 5.7: Block diagram of the trigger logic settings on the CAEN v1730 used in the experiment. The system was set up to write out a scatter event associated with any target event, a target event associated with any scatter event, and a RF event where both a scatter event and target event were present.

The resultant sequence is as follows: the variable pulse and delta pulse fire simultaneously, the delta pulse fires, the variable pulse fires, and the delta pulse fires. The LEDs were placed behind a diffuser ∼10 cm from the bare phototube in a light-tight enclosure and a series of data points were taken across the available full scale range of the digitizer for both phototubes use in the light yield experiment. The phototube output was fed into the same channel used in the experiment, and the system was triggered on an 'OR' of the avalanche pulser control signals. The logic gates controlling the LED were also fed into the acquisition system so that the state–sum, delta, or variable–corresponding to a given pulse could be identified in post-processing.

5.4 Acquisition Configuration

Given the desire to obtain event rates in the target detectors around 100 kHz and the 30 MB/s bandwidth limitation of the communications bus between the acquisition system and the acquisition computer storing data, it was paramount to develop a coincident trigger for the system. The CAEN v1730 has the capability of generating internal coincidence logic between channels with independent logic requirements for an individual channel trigger. The developed trigger logic is shown in Figure 5.7. The figure provides a block diagram meant to represent the functional logic, not the actual function of the onboard FPGA in the digitizer implementing the logic. An event in any detector produced a logic signal. For an individual target channel, this signal was branched into both an 'OR' with the other targets, and an 'AND' with an 'OR' from all the scatter detectors. The same configuration existed for the scatter detectors. The result was that an individual target detector triggered when a coin-

cidence was observed with any scatter detector, and an individual scatter detector triggered any time a coincidence was observed with a target detector. The individual nature of the trigger system resulted in events that were written asynchronously to disk, requiring reconstruction in post-processing. Additionally, the master control RF signal from the cyclotron was fed into a channel whose trigger logic was fed into an 'AND' with both the 'OR' from the target detectors and scatter detectors. So the RF channel was set to trigger when both a target detector event and scatter detector event were present.

The trigger generation on the digitizer was set to use CAEN's digital constant fraction discrimination algorithm with a delay of 4 ns and a 75% fraction setting for all of the channels associated with either target or scatter detectors [28]. The RF from the cyclotron is a sine wave and thus required different settings. The delay was set as close as possible to half the phase width, 56 ns, and the fraction was set to 50%. For the system to generate triggers from the RF, two features needed to be disabled: the trigger hysteresis protection, which is designed to keep the system from triggering on multiple pulses, and another feature that inhibits the trigger when opposite polarity signals are encountered.

The width of the trigger logic gates for the target detectors was set to 352 ns, and the trigger logic gates for the scatter detectors were set to 64 ns, making the total time window for the coincidences nearly 416 ns. This allowed a small amount of time for events where the scatter detector event occurred before the target detector to account for any potential signal chain offsets, and for background observation. The RF trigger logic gate was set to 96 ns, slightly less than the cyclotron period, to ensure that any event that included a coincidence between a scatter and target detector had an associated RF trigger. Despite this precaution, the RF trigger proved to be somewhat unreliable and not all coincidences resulted in an RF trigger. This was potentially due to the trigger request rate of the channel being 9 MHz.

All of the settings were managed using the customized version of the DPP-PSD Control Software discussed in Sec. 4.1.2, which includes the capability of reading a file containing a series of commands to write to registers on the digitzer. The file used during the experiment is reproduced in Appendix A. An error was discovered after the experiment that prevented the target detectors from triggering on one of the scatter detectors, so it was removed from the analysis.

5.5 γ-ray Calibration Data Collection

The primary data collected for calibration of the light axis come from three γ-ray sources: ^{137}Cs, activated Al, and AmBe. The ^{137}Cs produces a monoenergetic γ ray at 0.6617 MeV. The ^{137}Cs β^- decays into a meta-stable state of ^{137}Ba which then decays via γ-ray emission. The source is housed inside a small plastic disk that was placed on the vertical edge of the target scintillator housing between the two detectors. This line was used to anchor the bottom of the light axis.

The second source of γ rays used in the pulse integral calibrations came from the detectors themselves. Immediately preceding the experiment described here, the target detectors were

used for a different experiment that involved high fluxes of the same neutron beam. This led to activation of the aluminum housing through both (n, p) and (n, α) reactions. The (n, p) reaction leads primarily to two γ-ray lines at 0.8438 MeV and 1.014 MeV with a half life of 9.5 m. The (n, α) reaction also leads primarily to two γ-ray lines at higher energies: 1.368 MeV and 2.754 MeV. Since the energy difference between the three lines at lower energies is on the order of the system resolution, they are not good candidates for calibration purposes. Conversely, the 2.754 MeV line is in a region with little background contamination and has a double escape peak at 1.732 MeV. The data with no source present except the detectors themselves were taken so that this clean higher energy region could be used as a midway point between the ^{137}Cs line and the last γ-ray line used. The data with no source present were also needed as a background for the lower energy ^{137}Cs data.

The last γ-ray line used for calibration purposes comes from an AmBe source. The AmBe is primarily used as a neutron source, made up of a homogeneous mixture of ^{241}Am, which decays via α emission, and ^{9}Be. The α-decay of ^{241}Am leads to (α, n) reactions on ^{9}Be leaving an excited ^{12}C nucleus. The excited ^{12}C nucleus decays via the emission of a 4.438 MeV γ ray. An AmBe source was place in the same configuration as the ^{137}Cs for data collection to provide a higher-amplitude light calibration point.

Chapter 6

Simulation

This chapter explores questions addressed in simulation space to either validate experimental methods or provide input to the experimental analysis chain. First, the energy deposition spectra of mono-energetic γ rays was modeled for calibration purposes. Second, the potential differences in spatial distributions of particle energy deposition was investigated. Third, the quantities calculated from gross geometry (e.g., scattering angle) were verified as appropriate for the observed distributions of those quantities when the extended geometry is considered. Lastly, uncertainties in time of flight calculations were evaluated.

6.1 Monte Carlo Model

The GEANT4 simulation toolkit [2] was used as the basis for the Monte Carlo models of the detectors used in this work. The individual detector geometry in the simulation included the aluminum housing, scintillator volume, acrylic window, the glass front face of the phototube, the photocathode, and the magnetic shield of the phototube. These elements were housed in a *G4Tubs* cylinder with placements handled by reading an ASCII configuration file that specified detector use (i.e., scatter or target detector) and location, which is also used to process the experimental data. This allows adaptation for multiple experimental configurations without modification of the code itself while using the same information set used to analyze the experimental data.

The tracking was accomplished through the development of a *PostitionTimeEdHit* class derived from the *G4SensitiveDetector* class. The scintillator volumes were established as sensitive detectors, each placed with a unique ID corresponding to its occurrence in the configuration file and the type of detector. Target detector ID values start at 100 and increment upon occurrence in the configuration file. Scatter detector ID values start at 200 and increment on occurrence in the configuration file. This allows for identification of coincident events between categories of detectors and event classification of scatters between unique detector pairs when multiple target and scattering detectors are used. The simulation stores information for all particles which deposit energy in the scintillator volumes with the volume ID tags, particle mass and charge, energy deposition, starting point of the particle track, time

of the start of the particle track, and light production using Birks relation given in Equation 2.3. The quantities are then put into a TTree container class *PositionTimeEdTreeStructure*, which has helper functions developed to make statistical accumulation easily accessible through either the ROOT interface or post-processing classes.

The physics lists used, QGSP_BERT_HP or FTFP_BERT_HP, include high precision neutron interaction models which use cross section data from version 4.5 of the G4NDL library. This library is based on ENDF/B-VII.1 [35]. Although the physics validation for these packages have been shown wanting with respect to carbon reactions in this type of modeling, they benchmark well with respect to both γ-ray interactions and n-p elastic scattering [36]. Given that the requirements for the simulation in this project were an understanding of properties of the system response with respect to γ-ray interactions and n-p elastic scattering, no modifications to the physics lists were made.

For both the geometry and proton energy uncertainty calculations, it was desirable to compare known quantities to quantities calculated by the analysis software used in the analysis of the experimental data itself; a translation layer was developed to store the experimental data in the data structures used for the experimental data. The result was a TTree with the original *PositionTimeEdTreeStructure* and an associated *ScatterEvent* structure discussed in Chapter 7. The translation included the addition of the experimentally-observed temporal resolution to the time quantities associated with the Monte Carlo output.

For simulations of the experimental configuration of the double time of flight detector array, the configuration consisted of the setup detailed in Sec. 5.2. The GEANT4 representation of the array is shown in Figure 6.1. The beam transported was a planar circular source of 10-cm-diameter centered at $(0, 0, 0)$ that formed a beam of neutrons in the positive x direction. For two runs of 2×10^9 particles, the energy distribution was uniform from 0 to 38 MeV. The statistics of high energy events were poor compared to the lower energies due to the differential efficiencies, so an additional 2×10^9 particles were transported with a uniform energy distribution from 15 to 38 MeV. All events that simultaneously deposited energy in both a target and a scatter detector were stored on disk.

6.2 Recoil Distributions

To establish the recoil distributions for protons, the x, y, and z locations of single n-p elastic scattering events in the target detectors were accumulated in independent histograms. The x and z dimension of the scintillators show reasonably uniform deposition through the scintillating volume considered. The y dimension exhibits a bias in the positive y direction. This is due to the reduced escape probability of neutrons that require longer pathlengths to exit the detector after scattering into a specific angle. The resultant recoil distributions for protons in the consider geometry are shown in Figure 6.2. In general, the desired overfill of the detector was preserved save for the small bias in the y dimension.

To obtain energy deposition spectra for the γ-ray calibrations, the simulation was modified. For the AmBe and ^{137}Cs γ rays, the source was changed to be monoenergetic γ rays of

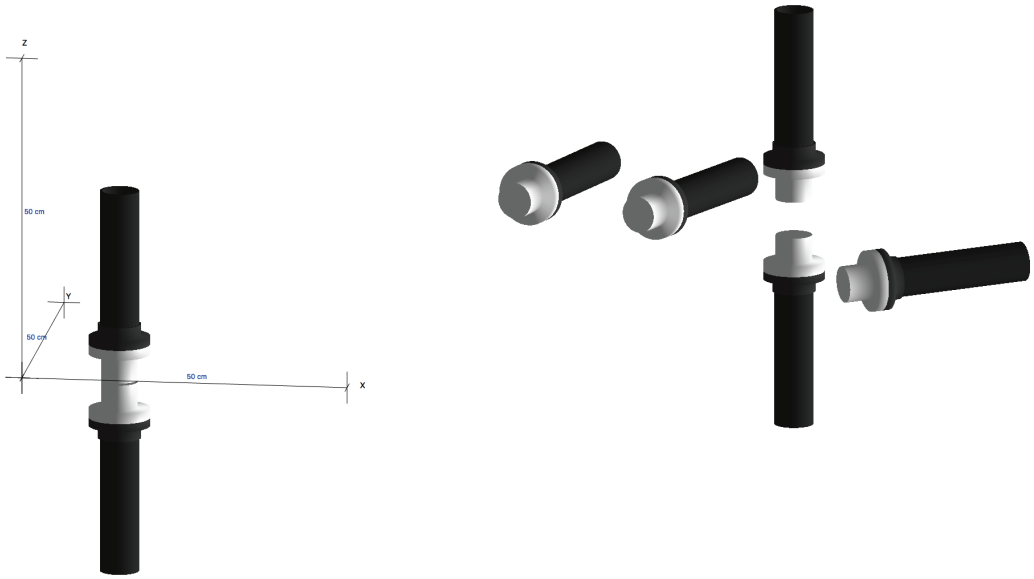

Figure 6.1: GEANT4 model of the scintillator scattering array.

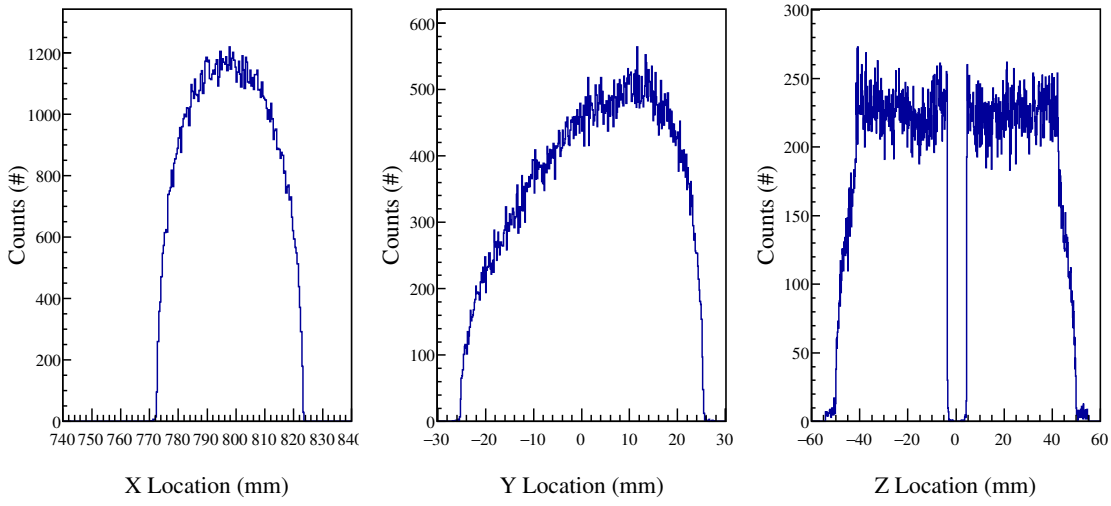

Figure 6.2: The spatial distribution of proton recoils resulting from the Monte Carlo of the experimental setup.

the appropriate energy emitting isotropically from a point source 1 cm from the edge of the target detectors. The constraint that energy depositions were required in both a target and scatter detector was dropped, i.e., any event that involved energy deposition in the target detectors was recorded. For the Al activation, a cylindrical isotropically emitting source was located within the Al walls of the scintillating volume to represent the self activity of the detector. Each γ ray was simulated independently and the result was accumulated according to their branching ratios. For each case, $\sim 2 \times 10^9$ γ-ray events were simulated. The resultant energy deposition spectra for both the EJ309 and EJ301 detectors are shown in Figure 6.3.

Constructing the same histograms of the spatial distributions for the γ-ray sources used for calibration revealed that the recoil distributions were not uniform throughout the detectors for the point sources. The distributions are shown in Figure 6.4. This was caused by the differential flux from an isotropic source being used at close range, as the source was placed near the front face of the detector and off to one side. There were significantly more events at the end of the scintillating volume as far away as possible from the photocathode. The concern with the recoil distribution being biased in this way is that the calibration would be shifted by the potential attenuation of the light or loss upon reflection. To test the degree to which this could bias the result, it was first verified that uniform distributions of energetic electrons could be obtained with a small standoff distance for the isotropic sources. At 25 cm, the point sources in simulation space showed uniform recoil distributions throughout the volumes. Data were taken both in the configuration of the light yield experiment and with the sources located at 25 cm for both the γ-ray sources used in the experiment that suffered from this potential bias. The results of the measured distributions were fit with the γCF in two ways. First, both sets of the individual γ-ray lines were fit and the predicted Compton edge in channels was compared. The results differed by less than 0.5%. Second, the two sets of γ-ray lines were fit together to get an overall calibration for the system. The result deviated by a maximum of 1% over the full scale range considered.

6.3 Potential Geometry Biases

Both the scattering angles and flight paths must be calculated from the measured geometry. To avoid potential systematic bias, it was necessary to test if calculating these quantities from the center point of the target detector to the center point of the scatter detector reflected the distribution of flight paths and angles. To accomplish this, the simulation result was translated into the data structures used for the experiment, and the flight paths and angles were calculated. The same quantities were then calculated for the known interaction locations from the simulation. The differences between them were accumulated in a histogram both on an angle-by-angle basis and as a whole. Both the flight path and angular consideration have a mean offset from zero by an amount much smaller than the error on the ability to calculate the quantity; thus, no corrections were made. The other quantity observed in these plots is the uncertainty both on the angles and flight paths. The

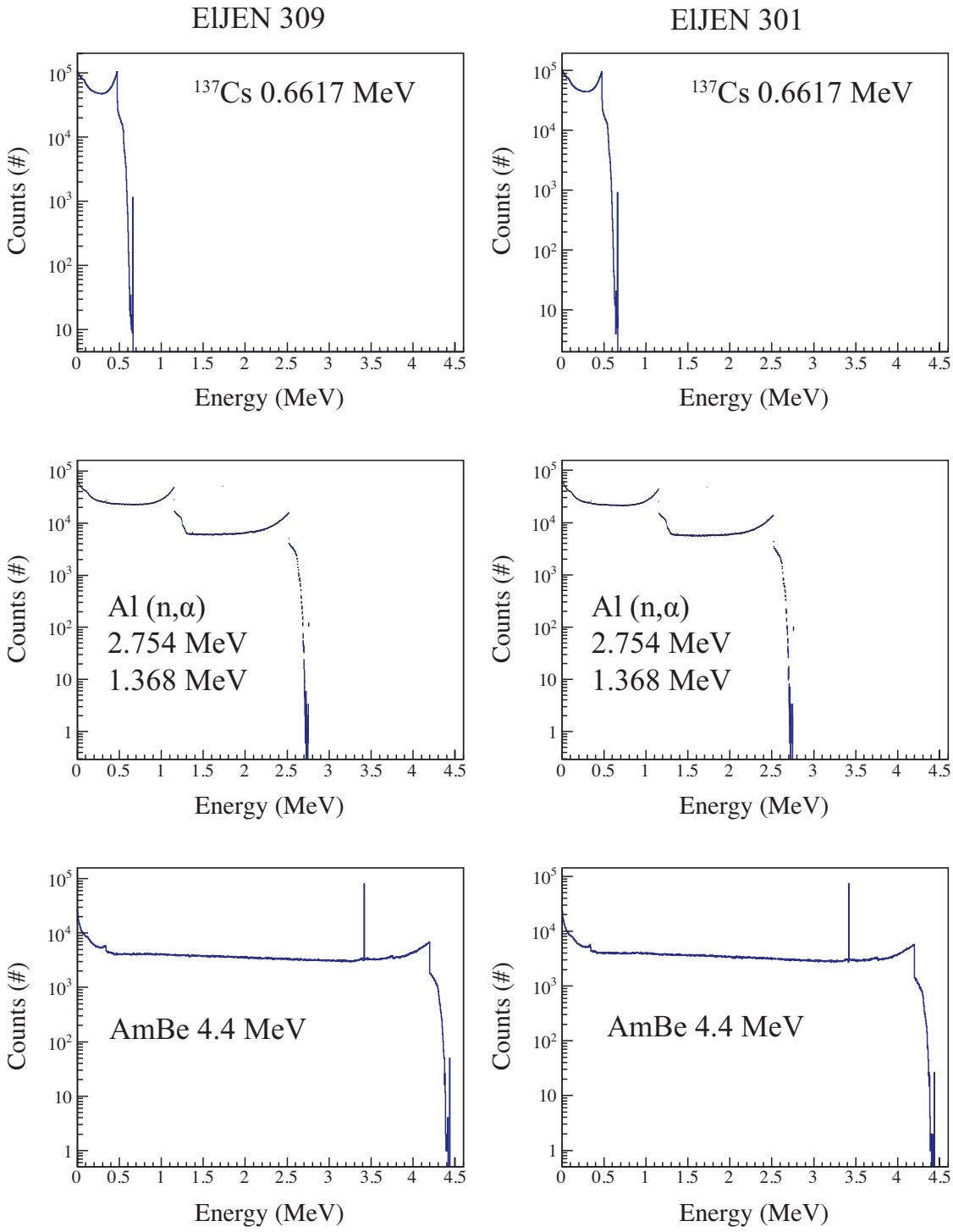

Figure 6.3: The results of energy deposition simulations for the γ-ray sources used to calibrate the MeVee light scale for both EJ301 and EJ309.

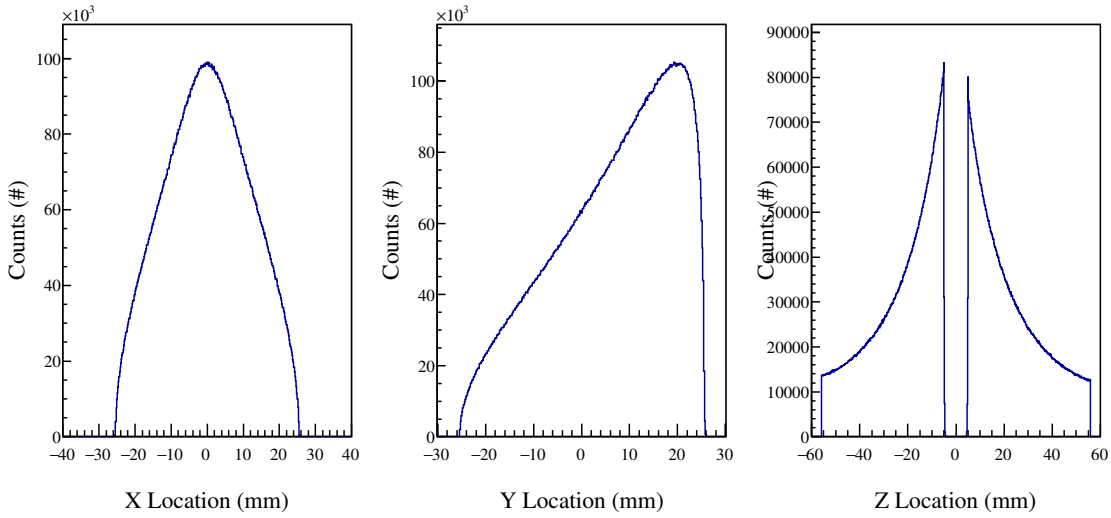

Figure 6.4: The spatial distribution of energetic electrons resulting from the Monte Carlo simulation of the experimental setup showing significant bias.

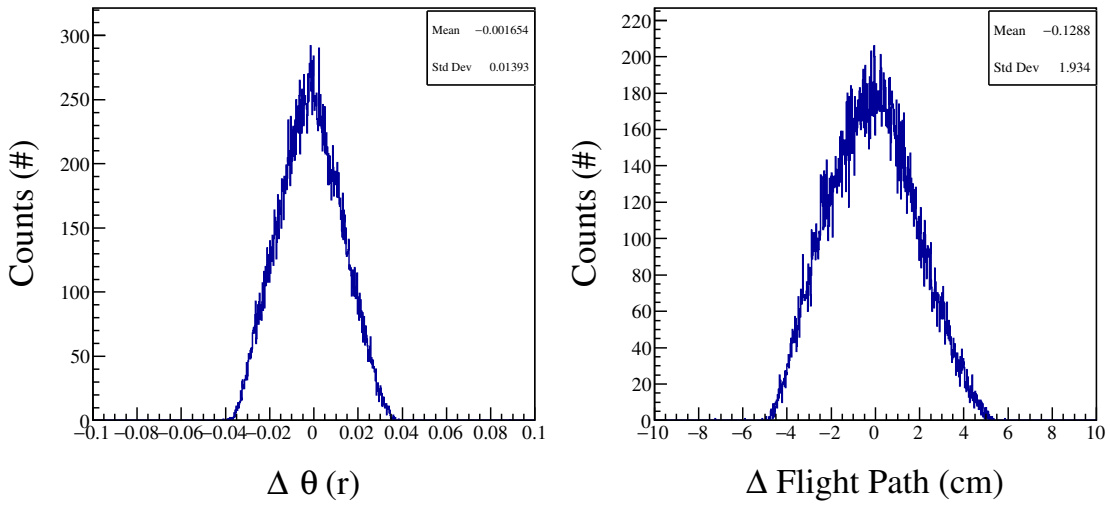

Figure 6.5: Left: The difference between angles calculated from the center points of the detectors vs. the angles calculated from interaction locations. Right: The difference between the distance between the center points of the detectors and the distance between the two interaction locations within the scintillator.

standard deviation is around 1° for all angles, and the uncertainty on the exit flight path is around the half width of the scintillator: 2 cm. The resultant distributions of the differences for the flight path and angle are shown in Figure 6.5.

6.4 Proton Energy Resolution

The proton energy resolution for the three different approaches to calculation of proton energy must be evaluated to optimize calculations of the quantity. The result of such an analysis is also necessary later in the data reduction. Analytic first-order approximations to the error prove troublesome as it is desirable to accumulate data for all angles, regardless of the means of calculating the proton energy, and each angle considered will have a different uncertainty. Time of flight measurements have uncertainty contributions from spatial variances, uncertainty in the flight path, and in obtaining the time of travel. To evaluate the uncertainty on proton energy, the data structures used for the experiment were filled with both the time of the observed interaction in the target detector and the time of the observed interaction in the scatter detector. Additionally, the experimental temporal uncertainty distributions were sampled and added to the times obtained from the simulation output. In this manner, the 4.4 ns uncertainty on the incoming time of flight and 0.5 ns uncertainty on the outgoing time of flight were added to the simulated times. The uncertainty in flight path is accounted for as real interaction locations are tracked in the Monte Carlo simulation, but the experimental analysis code uses the center-point of detectors. In this way, the experimental analysis code was used to calculate the proton energy using Equations 2.4, 2.5, and 2.6, respectively.

Since the actual energy deposition of the proton is recorded as part of the simulation, the percent difference between the calculated proton energy and the proton energy reported in the simulation can be obtained as:

$$\%\Delta E_p = 100 \times \frac{(E_{psim} - E_{pexp})}{E_{psim}}, \tag{6.1}$$

where E_{psim} is the energy recorded in the simulation and E_{pexp} is the energy calculated from the experimental analysis code given the simulation information as described above. Time of flight uncertainty calculations are generally heteroskedastic. This is especially true for the relativistic particles considered here due to the highly non-linear relationship between time and energy. Therefore, it is important to consider the proton energy resolution as a function of the proton energy. This was accomplished by accumulating the percent differences as a function of the proton energy, shown in Figure 6.6. The outgoing time of flight and angle distribution shows potential systematic bias at the low energy and has a larger variance than the incoming time of flight and angle determination which shows a consistent mean of zero. The difference in time of flight determination shows the largest variance of all of the distributions. To make the comparison more palatable, projections onto the y dimension were made for each x bin width. The resultant projections of the histograms were fit with

normal distributions in a χ^2 minimization procedure handled by Minuit [27]. The resulting standard deviations of the distributions and error on them were accumulated in Figure 6.7, which shows clearly that for all but the highest energies, the incoming time of flight and angle is the best means of calculating the proton energy for the setup considered herein. At the highest energies, there may be potential for a small improvement by using outgoing time of flight and angle to obtain the proton energy, but given the small difference, the incoming time of flight and angle was used for the proton energy calculations in this work.

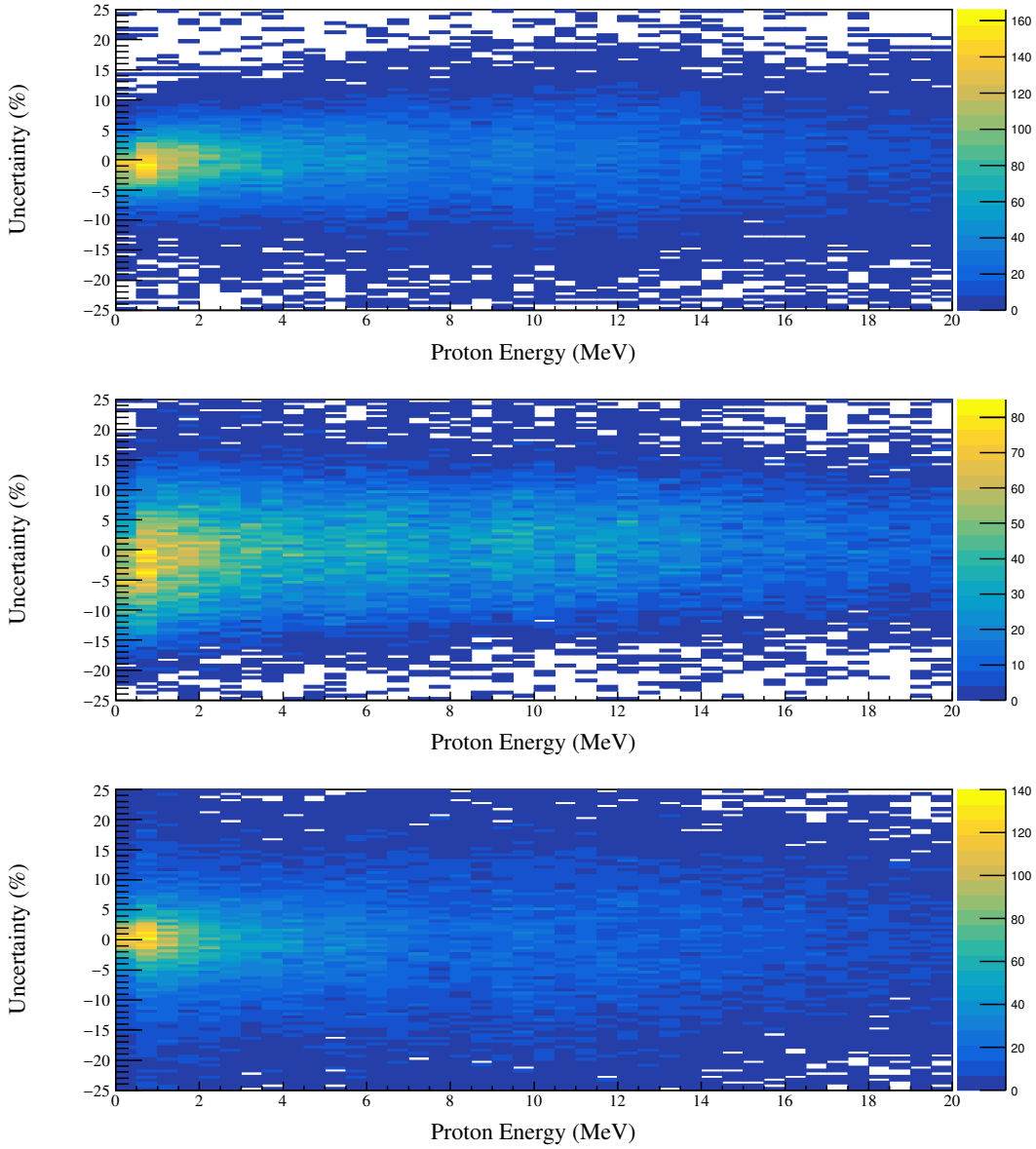

Figure 6.6: Results of the investigation of prospective proton energy resolution in simulation space considering the three different means of calculating proton energy. The top plot is the result using incoming time of flight and angle, the middle plot is using the outgoing time of flight and angle, and the bottom plot is using the difference in incoming and outgoing time of flight.

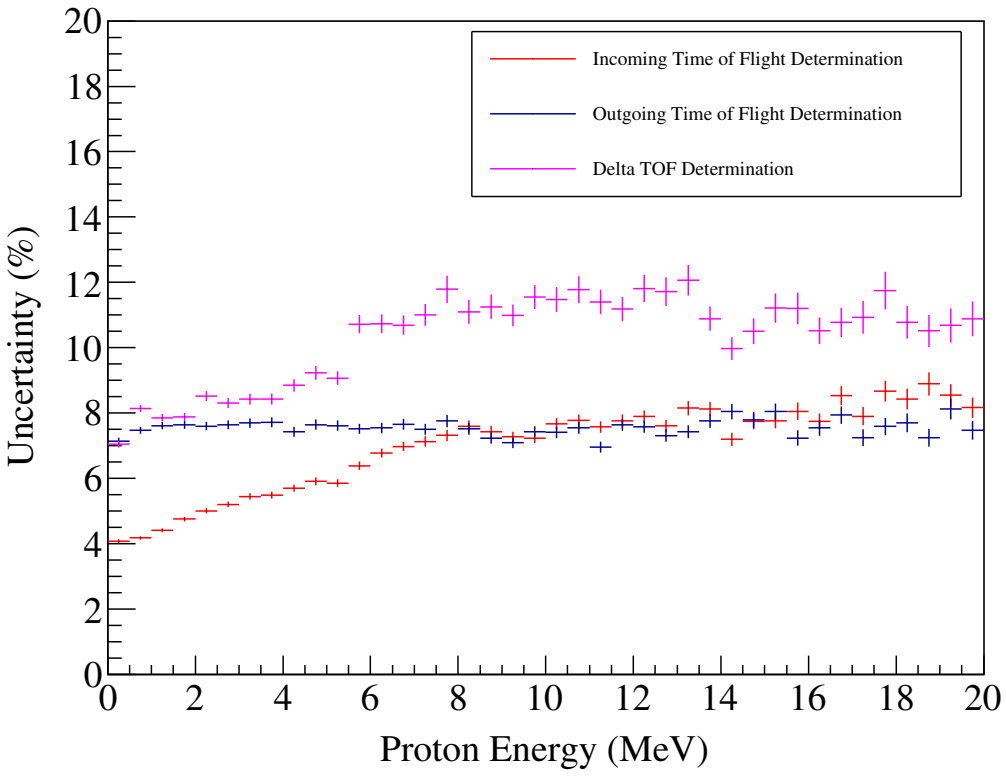

Figure 6.7: Results of fitting projections of the histograms shown in Figure 6.6 and accumulating the standard deviations of the distributions.

Chapter 7

Data Reduction and Error Analysis

The software developed to handle the analysis was intended to function generally regardless of the specific spatial configuration of the detectors or the number of detectors used. It was developed as a modular C++ code designed to take a set of raw waveform data from a scatter experiment to deliver a light yield result, through a series of automated and semi-automated algorithms. The algorithms in general either provide a characteristic of the data or system needed for additional processing or provide a reduction of the data into more fundamental quantities. An overview of the workflow is shown in Figure 7.1. This chapter details the the specific paths outlined in Figure 7.1, while presenting results of the intermediary steps. First, the management of quantities and calculations necessary throughout the process are detailed as well as the inputs required to run the analysis routines.

7.1 Geometry, System Configuration, and Kinematics

Nearly all of the algorithms require a specification of the system configuration with regard to the detector locations, their associated attachment to the acquisition machine, and the context of their use (i.e., target or scatter detector). This is handled by creating an ASCII file with the relevant information, referred to here as a 'configuration file.' The configuration file used in this analysis is included in Appendix B, along with a description of the formatting. A class was developed, *DDAQScatterConfig*, which is a child class of an inheritance tree that builds up the functionality incrementally from more basic types of configurations used in other analyses. The end result is a class that reads this file format and produces an interface layer for any algorithms or other codes, like the simulations previously discussed, that require information regarding acquisition configuration or geometry information. Internally, the *DDAQScatterConfig* class constructs a C++ map indexed by a vector of integers representing channel pairs that make up a coincident pair of detectors. The data structure stored with the index is a *ScatterCoincidence*, which stores flight paths, angles, as well as calibration information once it is generated later in the analysis. It can be constructed and used with just the configuration file, but also reads a calibration file generated later in the analysis. The flight paths and angles are calculated from the quantities physically measured (i.e., the

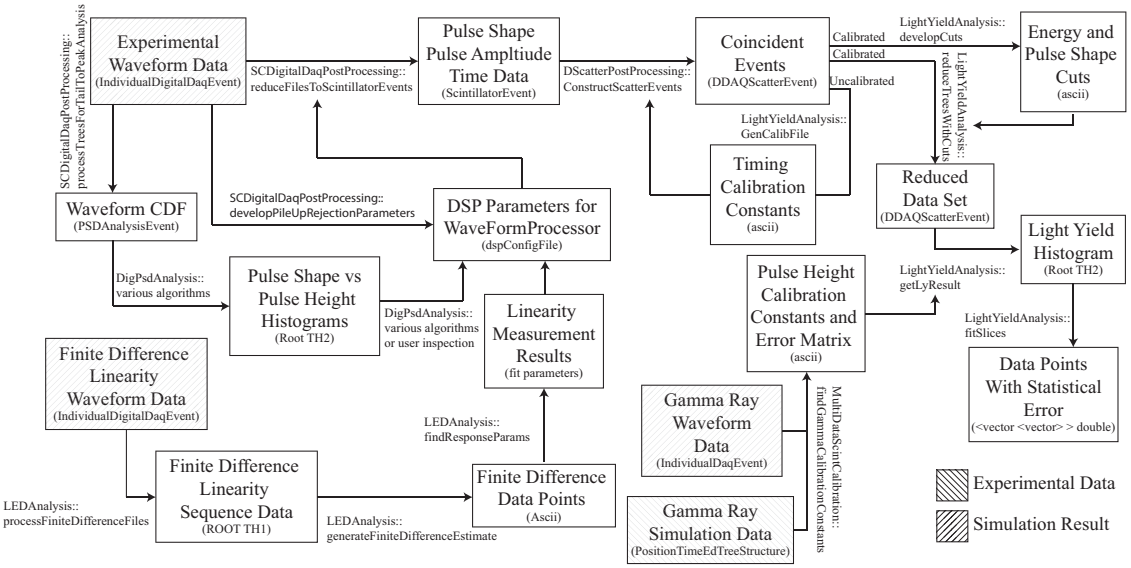

Figure 7.1: Functional diagram showing the inputs and steps used to generate a light yield result from collected waveform data.

detector locations in the room).

7.2 Signal Processing Parameters

The first step in the analysis is the development of appropriate parameters for the signal processing algorithms. First, the determination of pulse shape discrimination mode and associated parameters, pulse detection threshold, and pile-up rejection parameters must be determined. Second, any requirements for linearity corrections need to be assessed. These two analysis efforts are represented in the path leading down from the experimental waveform data box in Figure 7.1 that feeds into the 'DSP Parameter for WaveFormProcessor' box, and the path that starts with the finite difference waveforms and results in the same place. These paths result in the generation of a file that is read by a *WaveFormProcessor* class that manages the signal processing. The *WaveFormProcessor* class has an internal state for each of the individual channels that is a class developed for this analysis, called *DSPParam*, which holds variables that control what happens when its primary method, *processWaveform*, is called. The variables control what type of pulse shape discrimination algorithm to use, what integration length to use, what threshold to use as a start of the pulse, and a set of parameters to setup a function for linearity corrections.

7.2.1 Threshold and Pile-up Rejection

The threshold for determining the start of the pulse was set at 10 channels. To obtain parameters for the pile-up rejection algorithm, an iterative loop with user feedback is

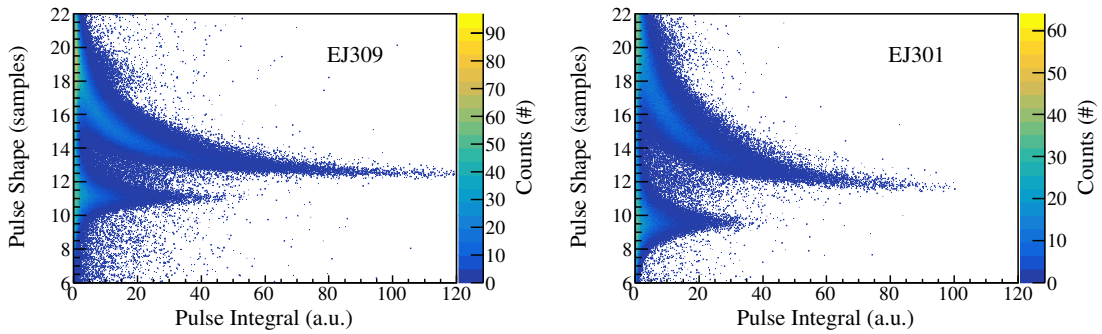

Figure 7.2: Results of using the 90-10 algorithm described in methods for both EJ309 (left) and EJ301 (right).

executed. The parameters are a smoothing parameter controlling the width of a centered moving average and a threshold control to identify pulses. A series of 1000 events is drawn for the user with determinations of pulse locations and pile-up data; then the user is asked for new parameters. The centered moving average was set to 21 samples and the threshold was set to 5 channels. These parameters were observed to include most clean events while not leading to spurious pile-up detection.

7.2.2 Pulse Shape Discrimination

To obtain a set of parameters for the pulse shape discrimination, a subset of the waveform data from the experiment was converted to *PSDAnalysisEvent*s, which are a container class storing the cumulative distribution functions of the original waveform. The only parameter necessary for the 90-10 analysis used here and described in Sec. 4.2 is the point at which to stop considering the 90-10 ratio. In this case, it was observed that a satisfactory result was obtained when the 90-10 analysis was truncated at 40 samples or 80 ns after the beginning of the pulse. A pulse shape discrimination plot with all of the data collected in the experiment for the target detectors is shown in Figure 7.2. With the double time of flight light yield methods, pulse shape discrimination is not neccessary, but can provide added reduction of background events. As an unimportant factor in the end result, little effort was expended in trying to obtain the best particle discrimination performance.

7.2.3 Linearity Results And Correction

Obtaining the parameters for the linearity correction begins with the reduction of raw waveform data to histograms of relevant quantities. This part of the analysis chain begins at the 'Finite Difference Linearity Waveform Data' box and results in a set of parameters used in the waveform processor. Since the data collection was managed point-wise across the range, each file related to each point was reduced individually using the *processFiniteDifferenceFiles* algorithm, which was designed to open a series of files, obtain pointers to the trees for each

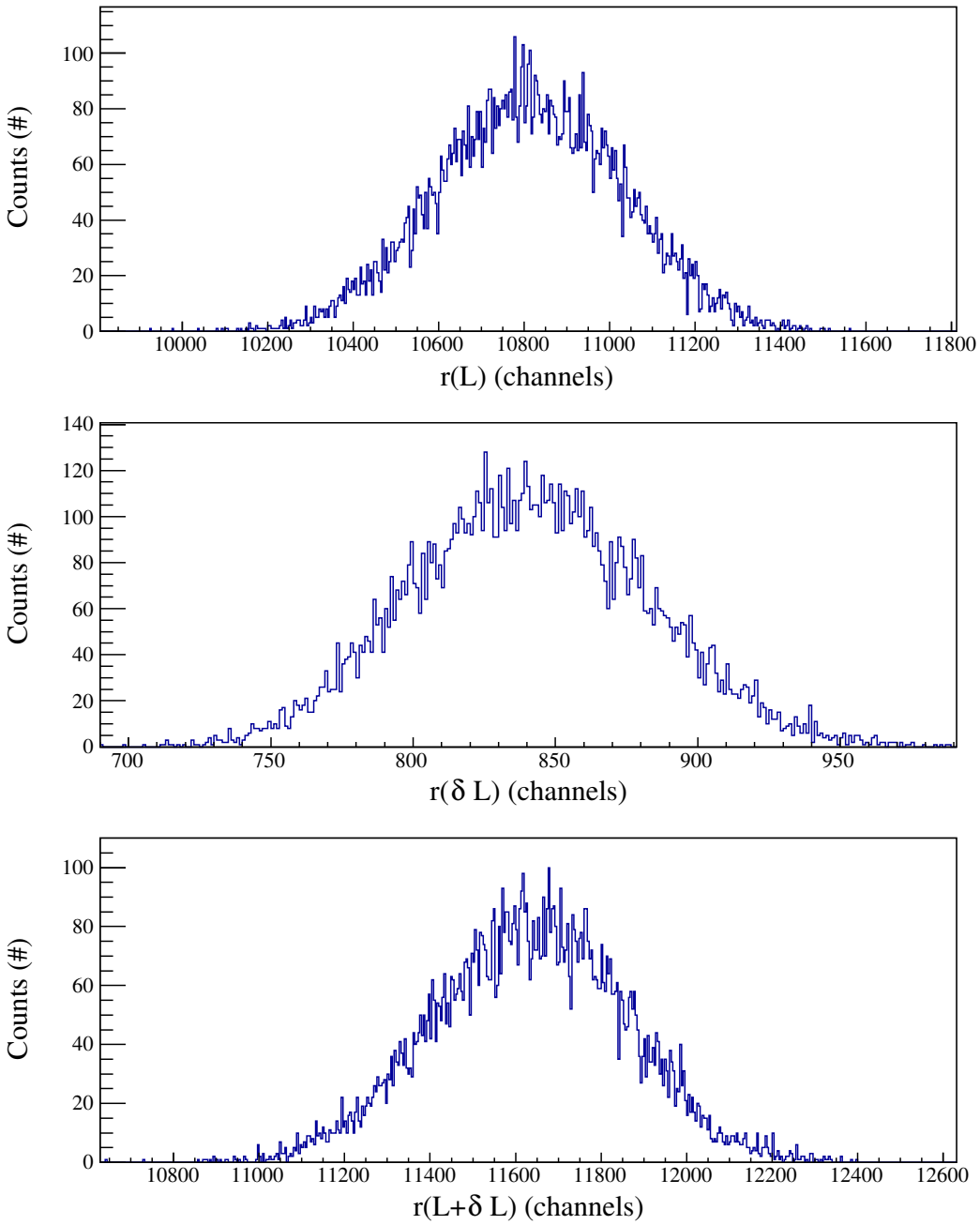

Figure 7.3: Results from data collection for a single point in the series of finite difference estimates used to obtain a linearity correction for the photomultiplier tubes used for the targets.

Parameter	Target 0	Target 1
a	-10.2 +/- 1.7	-8.7 +/- 2.5
b	0.98 +/- 0.06	1.08 +/- 0.06
c	6.9e-06 +/- 2.0e-07	3.9e-07 +/- 2.7e-07
d	-6.3e-10 +/- 1.3e-11	-2.3e-10 +/- 2.0e-11
e	9.4e-15 +/- 1.4e-15	-1.2e-15 +/- 1.8e-15

Table 7.1: Parameters representing a best fit for the phototube linearity measurements conducted.

channel, and then construct sequence data that includes a sum pulse, two delta pulses, and single pulse. The maximum observed amplitude for each of the events is stored in a container class and written to a tree. Additionally, histograms of these quantities were generated and stored on disk. To construct finite difference measurement points and produce predictions of them, three quantities for a given point were required: $r(L)$, $r(L+\delta L)$, and $r(\delta L)$. The resultant data files were processed in a loop that fit the relevant histograms using the *generateFiniteDifferenceEstimate* routine. The resultant estimated means of the distributions and the statistical error on the determination were stored as column-separated ASCII data. A series of the distributions corresponding to a single data point are shown in Figure 7.3. To handle the iteration between the trial response function and the measurement (see Sec. 5.3), a χ^2 function was minimized using MINUIT2 [27]. The χ^2 is given as:

$$\chi^2 = \frac{\left((r(L+\delta L) - r(L)) - (R(L_t+\delta L_t) - R(L_t))\right)^2}{\sigma_{r(L+\delta L)-r(L)}}. \tag{7.1}$$

The trial response function used was a fourth-order polynomial given as

$$R(L) = a + bL + cL^2 + dL^3 + eL^4, \tag{7.2}$$

where a, b, c, d, and e are the free parameters being minimized. The resultant parameters and their uncertainties are summarized in Table 7.1.

The resultant χ^2 for both of the photomultiplier tubes tested were approximately one showing that the response function was reasonably represented by a fourth-order polynomial. The result of the predicted difference measurements is shown in Figure 7.4 along with the resultant estimated response function compared to an ideal linear response generated from the first two parameters of the fit. Figure 7.4 also shows the predicted difference between the response generated by the fit and the ideal linear fit. This difference is obtained by taking the negative of the non-linear terms.

7.3 Reduction of Waveform Data

Having determined a full set of parameters for the signals processing algorithms, the waveforms are reduced to TTrees containing *DDAQProcEvent* class structures that store

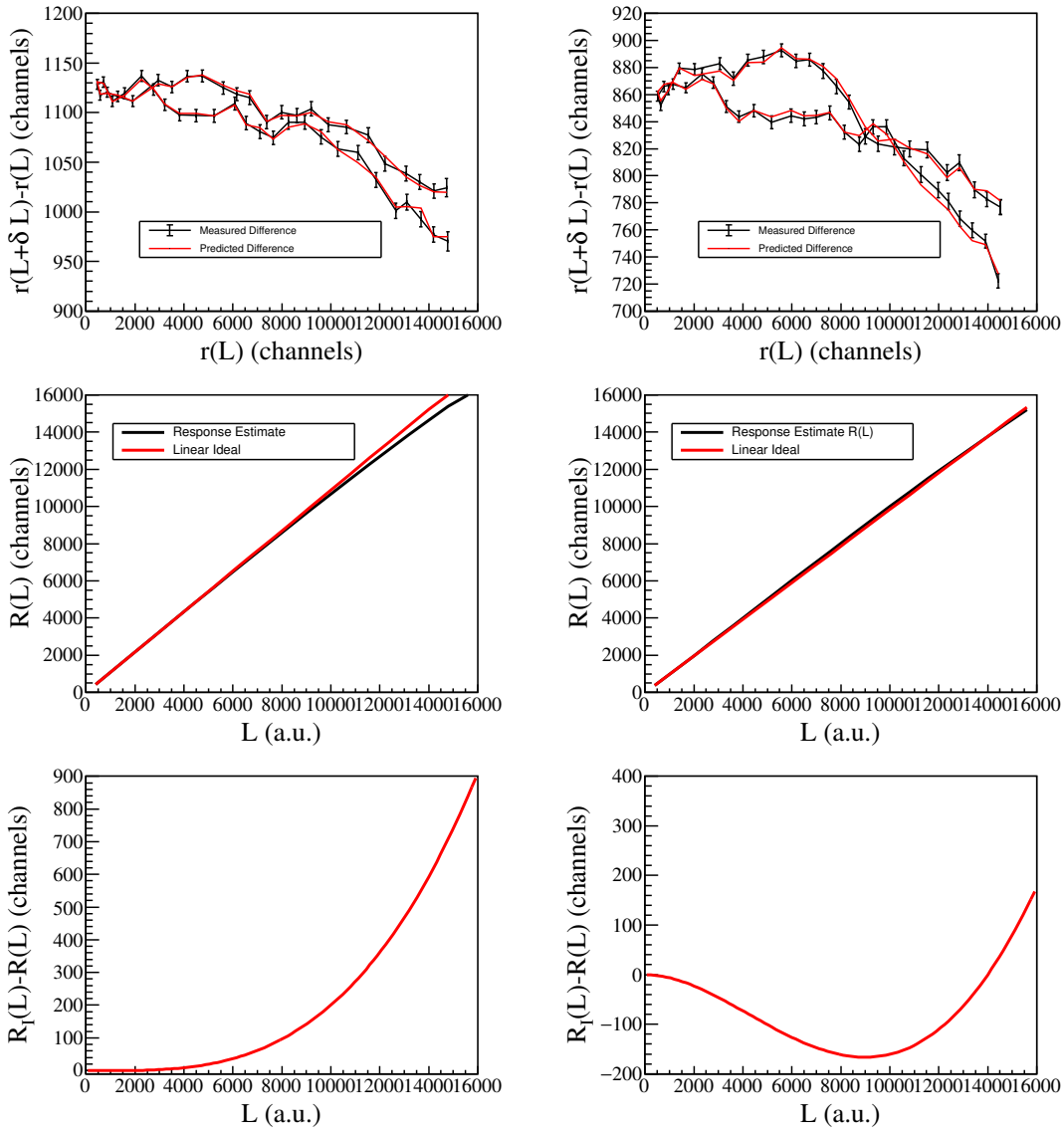

Figure 7.4: Results from the analysis of the finite difference measurements of phototube linearity. The left and right columns are the measurements for the photomultiplier tubes used with Target 1 and 0, respectively. The top figure here shows the measured differences as a function of the single amplitude and the predicted differences from a fit with a fourth-order polynomial. The middle figure is the estimated response of the photomultiplier tube. The bottom figure is the deviation from an ideal linear system.

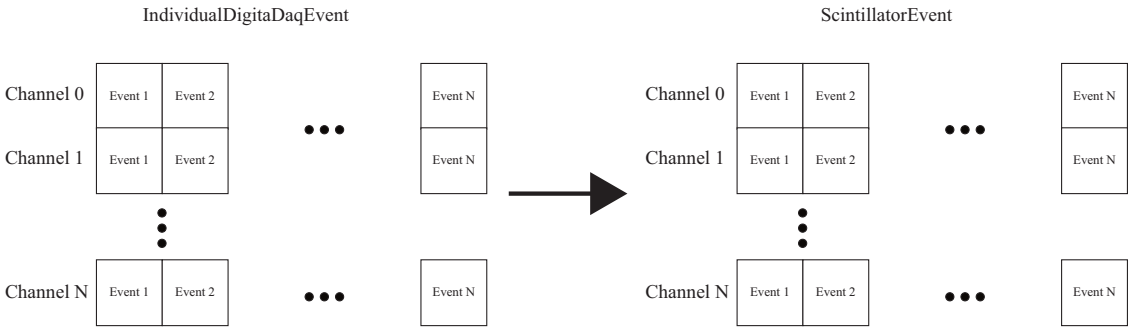

Figure 7.5: The *SCDigitalDaqPostProcessing::reduceTreesToScintillatorEvents* takes a series of files and reduces the full waveform data to pulse integral and pulse shape while preserving the overall data layout.

the original 32-bit unsigned integers from the acquisition and doubles for pulse shape and pulse integral. This step is represented in Figure 7.1 as starting at the 'Experimental Waveform Data' box and moving to the right. As the acquisition is restarted at regular intervals to keep file sizes at approximately 2 Gb, the resultant time stamps are referenced to the beginning of the file. So, the individual files were reduced individually and, at this stage, the individual channels are still managed independently. Although this step can be done in concert with the rest of the data analysis, the workflow was designed such that steps that may need to process the data multiple times do not need to duplicate the computationally complex effort present in this reduction. This reduction is managed by the *SCDigitalDaqPostProcessing::reduceTreesToScintillatorEvents* algorithm. The algorithm takes an ASCII list of the files to be processed and a signal processing configuration file. It uses the latter to construct a *WaveformProcessor* that is responsible for the reduction. It then loops over the file list given and the trees in each of those files, processing each individual event using *WaveformProcessor::processWaveform*. The *WaveformProcessor::processWaveform* takes the waveform and a channel number as input to obtain a pulse shape and pulse integral of the waveform. It then obtains a baseline corrected and inverted waveform using the methods described in Sec. 4.2 that results in Equation 4.2. Next, if a linearity correction needs to be applied, the positive waveform is adjusted on a sample-by-sample basis to reflect the difference between the observed amplitude and what would have been observed in a linear system. This is given as:

$$s_{ic} = s_i - \left(c(R^{-1}(s_i))^2 + d(R^{-1}(s_i))^3 + e(R^{-1}(s_i))^4\right), \tag{7.3}$$

where s_{ic} is the linearity-corrected sample value, s_i is the uncorrected sample value, $R^{-1}(s_i)$ is the inverse of the response, and the constants are from the fit of the experimental linearity data described in Sec. 7.2.2. The inversion was managed by interpolating a table of values generated from the inverse of the fourth-order polynomial trial function. Following the correction, the integral and pulse shape determination is performed as described in Sec. 4.2. The result is a set of reduced files with data layout similar in structure to the original data,

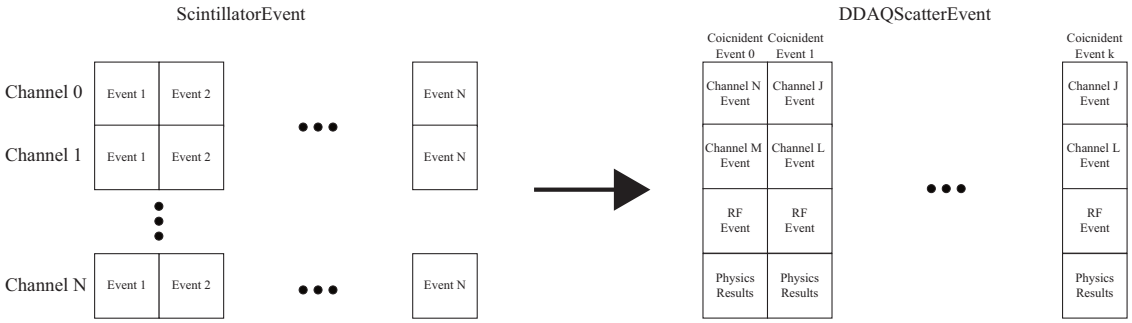

Figure 7.6: The *DScatterPostProcessing::constructScatterEvents* takes a series of files with asynchronously stored events with trees for each channel and constructs *DDAQScatterEvents* containing time-correlated events from different channels.

but with the waveforms transformed from arrays of ∼600 doubles, to 2 doubles representing the physical quantities of interest. This is represented in Figure 7.5. This step was performed for multiple integration lengths to investigate the effect of integration length on the final result. An exception exists in this step for the RF signal from the cyclotron. Since the RF has no associated amplitude or shape, the data are stored as an *RFEvent* class that stores just the timing information from the acquisition.

Two conditions can lead to rejection of events at this stage of the data processing. First, the data are tested to see if the digitizer has been saturated. If a negative event has a sample with amplitude zero, it has clipped the full scale range and is rejected. Second, the data are as to whether pulse pile-up exists. If more than one event is observed within the specified integration window, the data are rejected. These rejections account for less than 1% of the total data collected.

7.4 Scatter Event Construction And Timing Calibrations

Continuing to the right in Figure 7.1, the next step of the process is to transform the independent asynchronously written data to time-correlated events between target and scatter detectors and calculated physics quantities of interest. A representative diagram of this transformation is shown in Figure 7.6. This process was managed by the *DScatterPostProcessing::constructScatterEvents* algorithms. The algorithm, again, works on independent files provided as an ASCII list of file containing the output ROOT file from the waveform reduction. For each file, the asynchronous *DDAQProcEvents* from all of the channels are brought into memory in the form of a C++ deque. The *RFEvents* from the cyclotron are added to a separate deque. The deque containing the events from the detectors is sorted with regard to the acquisition time tag using *std::sort*. This results in a deque of all recorded channels stored as *DDAQProcEvent*s in the time series in which they were observed.

To construct the coincidences, the algorithm iterates over the deque testing if the next event is within a specified temporal overlap window. The window was set to 500 ns, just

slightly longer than the coincident window used for triggering of the data aquistion system. If the next event is within a coincident window, the algorithm first tests if the current event was in coincidence with the last event by testing if a vector of *DDAQProcEvents* holding coincidences is empty. If the event was already a part of a coincidence, the next event is added to the vector holding the coincidences. If the coincidence vector is empty, then both the current event and the next event are added to the vector. After either of these processes are completed, the algorithm moves to the next event. This ensures that coincidences between more than two detectors are identified, while not duplicating data from single events in the case where three or more detectors are in coincidence. When the next event is not in the match window, the algorithm tests if the coincident vector contains events. If there is not a coincidence stored in the vector, it moves to the next event. If it does have a coincidence in it, the RF event closest in time is associated with it.

The resultant collection of events corresponding to multiple detector events and an event from the cyclotron RF were tested for the following criteria. First, the time difference between the target detector event and the RF event is tested to ensure it is within 2 μs. With the trigger occasionally failing on the RF channel, this was done to ensure that the RF event was close in time and did not include any potential phase drift of the cyclotron. Although it is possible to associate the multiple detector events with RF events from longer times, selection of these events introduced additional uncertainty when timing against the cyclotron. Second, the number of detectors that participated in each coincidence is two. Although reconstruction of higher-order coincidences may be possible, these events were rejected. Lastly, the two detector events that occurred were tested to ensure they formed a valid coincidence between a target and scatter detector using the information from the *DDAQScatterConfig* class. If any of these criteria were not met, the coincidence was abandoned. If these criteria were met, the algorithm fetches the *Coincidence* class associated with the target and scatter pair and passes it, along with the two detector events and the RF event, to the constructor for the *DDAQScatterEvent* class. The *DDAQScatterEvent* stores the events it is handed and calculates the following quantities assigning them to internal doubles:

- the measured incoming time of flight of the neutron
- the reconstructed incoming time of flight
- the expected incoming time of flight of the neutron calculated from kinematics
- the time of flight of the outgoing neutron
- the incoming neutron energy determined via kinematics
- the incoming neutron energy determined via time of flight
- the scattered neutron energy determined via time of flight
- the energy of the proton determined via outgoing time of flight and angle

- the energy of the proton determined via incoming time of flight and angle
- the energy of the proton determined via energy conservation
- numerical ID for the *NDAQScatterCoincidence*
- pulse integral in the target detector
- pulse integral in the scatter detector
- pulse shape value for the target detector
- pulse shape value for the scatter detector
- cyclotron period offset

These *DDAQScatterEvent* objects are then stored on disk in a single TTree. The first time through, all of the time of flight quantities, and any quantity derived from these, are incorrect. There is an unknown offset between the time an event occurs in the scintillator and when the signal is recorded in the acquisition. These offsets, potentially different for all detectors involved, can come from different signal propagation times through the system electronics. For example, the scatter detectors require longer cables than the target detectors due to the spatial distance from the connection point. The difference in cable length can introduce tens of ns of delay, but many other potential offsets exist thus necessitating the need for an absolute time calibration.

To obtain an absolute calibration of the time domains of interest, γ-ray events are used to determine time calibration constants. As such, a cut is placed on the data in the pulse shape domain providing a cleaner selection of γ rays. For the incoming time of flight, the measured time, t_{m1}, can be represented as:

$$t_{m1} = t_1 - t_{\mathrm{RF}} \tag{7.4}$$

where t_1 is the time tag for the event in the target detector and t_{RF} is the time tag for the cyclotron RF event. To calibrate the signal chain so that the time corresponds to the transit time of the particle, a histogram of incident gamma rays was constructed. This resulted in a peak corresponding to the photon flash produced when deuterons impinge on the target. A χ^2 minimization between the photon flash and the superposition of a normal distribution with a linear background was performed to obtain the centroid of the distribution, the associated width of the distribution, and the statistical error on the parameters. The known speed of light and known flight path allows a prediction of the time that should have been measured for the γ-ray events. Therefore, subtracting the anticipated flight time of a photon produces a time calibration constant given by:

$$t_c = \bar{x} - \frac{L}{c}, \tag{7.5}$$

where $\bar{x}$ is the centroid of the distribution, L is the flight path, and c is the speed of light, thereby providing a relative time calibration between the cyclotron and the target detectors. A characteristic result of the χ^2 minimization considering incident γ rays is shown in the top panel of Fig. 7.7.

As discussed in Sec. 4.5, there is an ambiguity in the incoming flight time due to the cyclotron period, T_{cyc}, being shorter than the flight time of particles. In this case, $T_{cyc} = 111.094$ ns while flight times range from $\sim 80 - 400$ ns, which is resolved using the outgoing time of flight. As such, the absolute incoming time of flight, t_{inc}, is given as:

$$t_{inc} = t_{m1} - t_c + n \times T_{cyc}. \tag{7.6}$$

The uncertainty in the timing calibration constant is small and poses a potential source of systematic bias. An additional source of systematic uncertainty that does not lead to systematic bias is the temporal spreading of the incident deuteron beam. This is observed in the width of the photon flash. The photon flash from the beam was characterized in this work to have a width of $\sigma_X = 3.94$ ns. This is due to an inherent spatial spreading of the incoming beam pulse, and therefore, an individual event using this time of flight is uncertain by this amount regardless of the temporal resolution of the system. This uncertainty was used in the evaluation of the proton energy resolution discussed in Sec. 6.4.

The calibration of the exit time of flight was done using $\gamma - \gamma$ coincidences between the detectors using γ rays from the photon flash. The calibration is very similar to that for the incoming time of flight. The measured outgoing time of flight was taken as:

$$t_{m2} = t_2 - t_1, \tag{7.7}$$

where t_2 is the clock time of the event in the scattering detector. A calibration time constant was determined by creating a histogram of the $\gamma - \gamma$ coincidences. It was then fit with the same functional form as described above. Thus, the outgoing time of flight is given as:

$$t_{out} = t_{m2} - t_c, \tag{7.8}$$

where t_c is the same as in Eq. 7.5. A characteristic fit of $\gamma - \gamma$ coincidences is shown in Fig. 7.7. Here, the spreading in the peak is $\sim$0.25 ns, which is on the order of the coincident resolving time of the photomultiplier tubes used. This uncertainty was also used in assessing the proton energy resolution in Sec. 6.4.

Since the incoming time calibrations were required for each target and outgoing time calibrations were required for each angle, an algorithm was developed that manages the generation of a timing calibration file. The *LightYieldAnalysis:GenCalibFile* is a semi-automated routine that requires user input. It begins by generating pulse shape histograms to obtaining pulse shape cuts for γ rays for all detectors considered. The result of the cut on pulse shape is shown in Figure 7.8. The algorithm then generates a series of histograms needed for the timing calibrations, i.e., as many incoming time of flight histograms as there are target detectors and as many outgoing time of flight histograms as there are scatter detectors. Since the incoming time of flight is uncertain with regard to the cyclotron period, the histogram

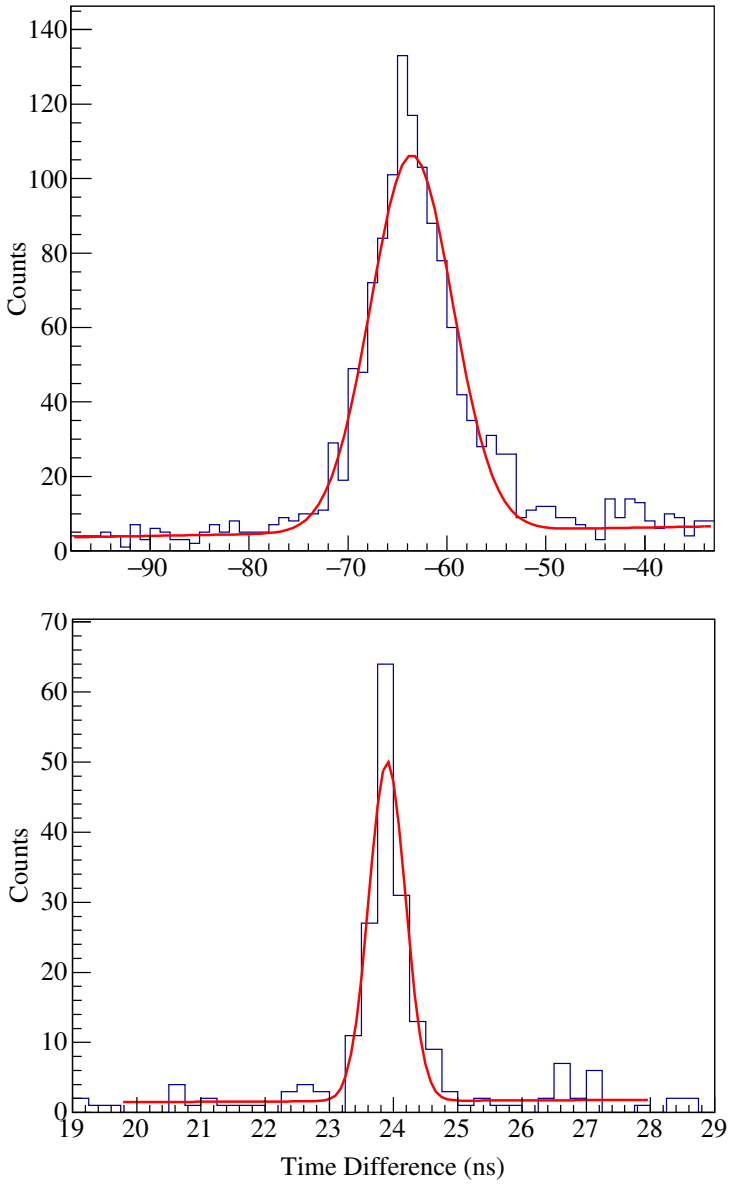

Figure 7.7: Top: The blue curve shows the result of histogramming time differences between the cyclotron RF signal and the γ-ray events in a target detector. The primary cause of the width this pulse is the spatial spreading of the beam pulse itself. The red curve is a fit of the measured data with a normal distribution plus a linear background. Bottom: The blue histogram shows the result of histogramming time differences between the detectors for γ-ray events. The spreading of the peak is reflective of the system time resolution with a $\sigma \approx 0.25$ ns. The red curve is a fit of the measured data with a normal distribution plus a linear background.

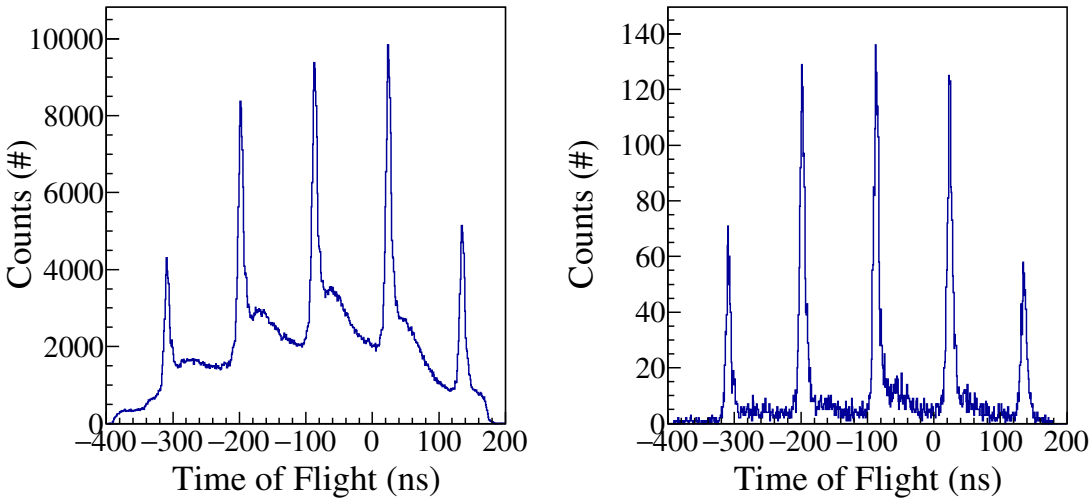

Figure 7.8: Incoming time of flight plot before (left) and after (right) γ-ray cuts applied to the pulse shape variable. Clearly seen is the ambiguity in the incoming time of flight due to the pulse period of the cyclotron.

constructed contains a series of γ-ray peaks corresponding to the photon flash. Figure 7.8 shows the results of the γ-ray cuts and the repetition of the cyclotron pulses in time. Since the γ-ray peaks observed are all separated by the pulse period of the cyclotron, any one of their centroids can be used to derive the timing calibration constant. Thus, the code requests that the user employ the ROOT interface to zoom on one of the γ-ray peaks and provide estimates of the centroid, standard deviation, and number of counts to use as a seed for the χ^2 minimization. This is repeated for all target detectors. Following this, the outgoing time of flight histograms are approached in a similar manner, but given the simpler time of flight spectrum shown in Figure 7.9, which has only one γ-ray peak, the code obtains an initial seed for the fit automatically and then runs the minimization only asking the user to verify the fit result. During the process, the algorithm writes the relevant results of the fit to disk in the form of a calibration file that specifies the observed centroid of the γ-ray peaks for all targets and angles. Additionally, it writes an error file that contains the centroids and their uncertainties that is used later in the treatment of systematic uncertainties. The *DetectorConfiguration* class is designed to read the calibration file at which time the calibration constants are determined for use in the analysis. Referring back to Figure 7.1, this whole process is represented as the loop below the 'CoincidentEvents' box, which illustrates that this information is fed back into the *DScatterPostProcessing::constructScatterEvents* algorithm.

With the timing calibration complete, the *DScatterPostProcessing::constructScatterEvents* is run on the data a second time to produce *DDAQScatterEvents*. This second pass through the data leaves all of the time of flight variables, and their derivatives including particle energies, correct. This allows investigation of the performance of the prospective reconstruc-

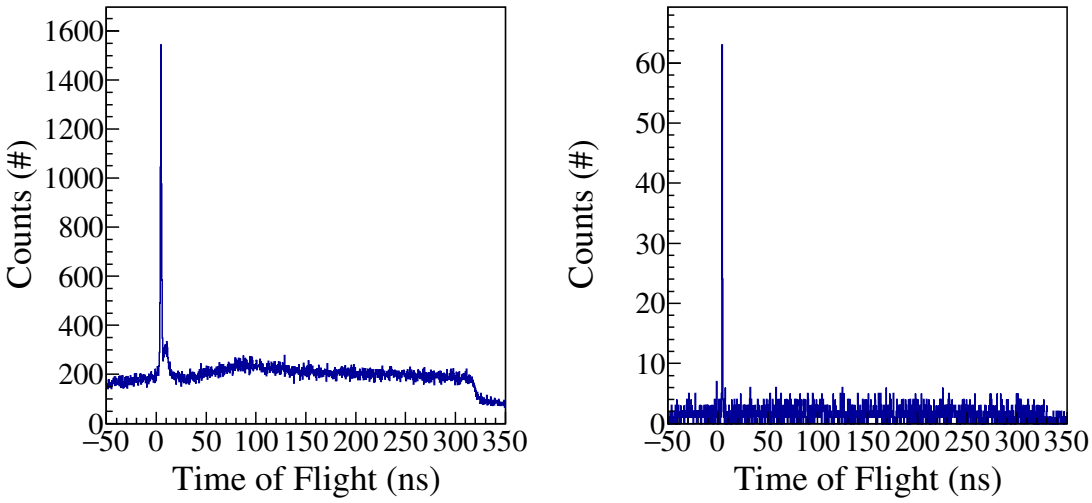

Figure 7.9: Outgoing time of flight plot before (left) and after (right) γ-ray cuts applied to the pulse shape variable. Clearly seen is the peak corresponding to $\gamma - \gamma$ coincidences between the detectors.

tion algorithm outlined in Section 4.5 for the incoming time of flight as well as correlating recoil particle energies with pulse integral. Starting with the reconstruction algorithm, Figure 7.10 shows the results of the reconstruction algorithm that establishes the correct integral cyclotron period offset. The top panel of Figure 7.10 shows the pulse integral measured in Target 0 plotted against the original measured time of flight. Although some features reflecting bands corresponding to n-p elastic scattering events are present, they are discontinuous and at unrealistic times offset by $n \times T$. The bottom panel of Figure 7.10, which is the pulse integral in Target 0 plotted against the reconstructed time of flight, shows the success of the reconstruction algorithm. Bands associated with different angles corresponding to n-p elastic scattering events in the target are continuous and reflect the flight times for neutrons of the energy range anticipated. Additionally, there are spurious events that are correlated with incorrect beam pulses. These events correspond to both accidental coincidences and double scatters in the target. Since the reconstruction algorithm assumes that the nuclear reaction in the target is n-p elastic scattering, other reactions that have different kinematics are assigned to the incorrect beam pulse. Translating the reconstructed time of flight to proton energy using Equation 2.4 results in Figure 7.11, which shows that the bands associated with different angles corresponding to n-p scattering events in the target coalesce into a single curve representative of the relationship between light production and proton energy deposition (as well as strong background contributions). The next efforts in the data analysis are the reduction of the background contributions in an attempt to isolate and characterize the light yield relation.

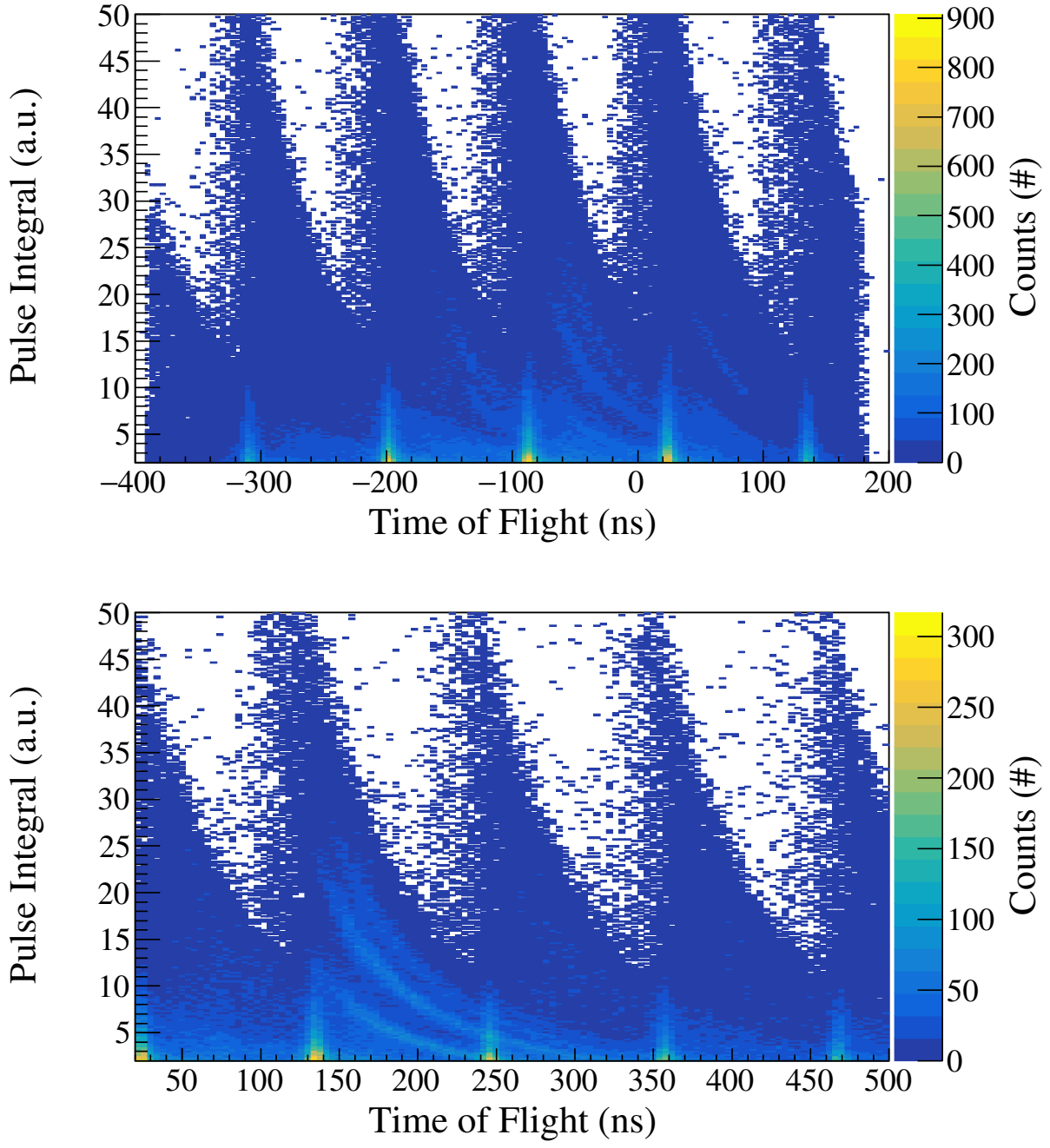

Figure 7.10: Comparison between the ampltude in target 0 when plotted against the measured time of flight (top) and the reconstructed time of flight (bottom). The reconstructed time of flight plot shows clear and continuous bands corresponding to the anticipated n-p scatter events.

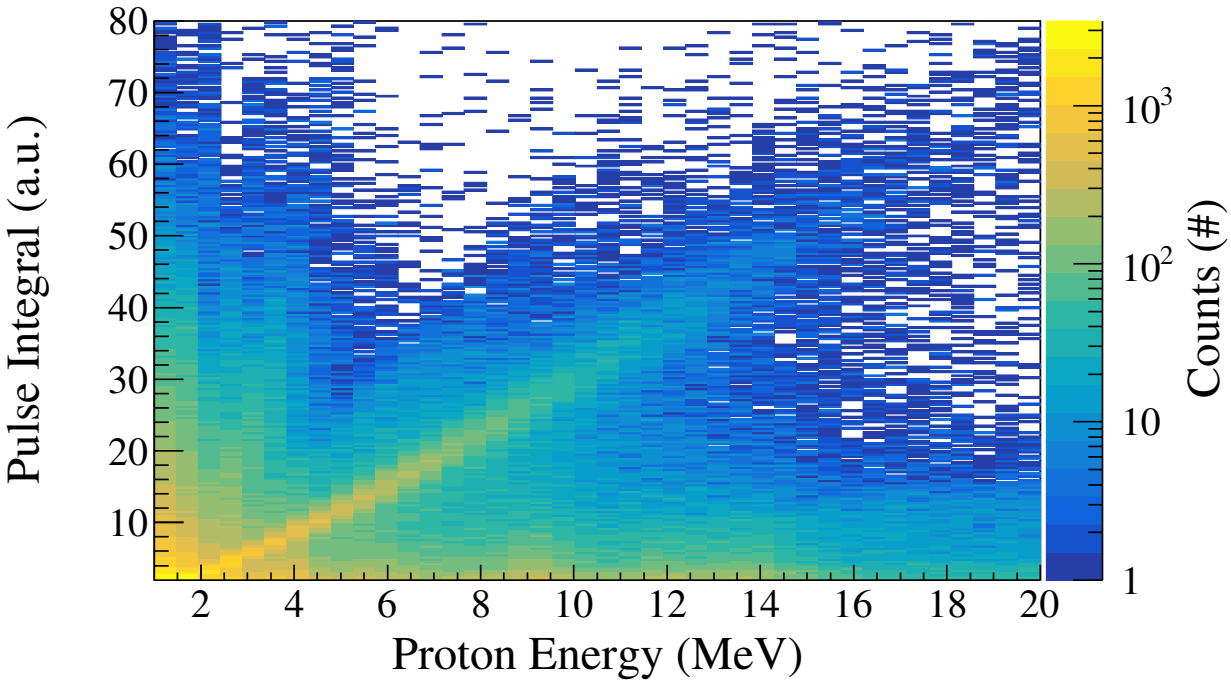

Figure 7.11: A histogram of the target pulse integral vs. proton energy yielding an initial state of a light yield result for the full data set for Target 0 (EJ309) with no cuts applied. The bands corresponding to different angles seen in the bottom panel of Figure 7.10 coalesce when considering the recoiling proton energy. Additionally, a significant amount of background exists.

7.5 Isolating n-p Scatter Events

The data set at this stage includes a significant amount of background events. To isolate the events of interest (i.e., n-p elastic scattering events in the target with a correlated time tag in the scatter detector), a series of physics-based constraints were developed and applied to the data. The following constraints were applied:

- The pulse shape parameter in the target corresponds to a proton recoil.
- The pulse shape parameter in the scatter detector is not a γ-ray event.
- The incoming neutron energy corresponds to locations where n-p elastic scattering bands are observed when considering the pulse integral vs. reconstructed incoming time of flight plots (such as in Figure 7.10).
- The outgoing neutron energy corresponds to locations where an n-p elastic scattering band is observed when considering the pulse integral vs. exit time of flight.
- The difference between the anticipated incoming time of flight and the exit time of flight is within a 20 ns match window.

To develop these cuts, an interactive algorithm, *LightYieldAnalysis::developCuts*, was developed that generates a series of plots, prompts the user to interact with them, and asks for specific input values. This is represented in Figure 7.1 as the loop coming from the right of the 'Coincident Events' box and feeding into the '*LightYieldAnalysis::reduceTreesWithCuts*' box. The *LightYieldAnalysis::developCuts* algorithm begins by prompting the user for horizontal cut values on the pulse shape plots shown in Figure 7.2, as well as similar plots for the scatter detectors. These pulse shape constraints are then used in the generation of a series of pulse integral vs. time of flight plots for both the incoming time of flight on a per target basis, and pulse integral vs. exit time of flight on a per angle basis for all considered angles. The user is asked to provide the times at which the n-p elastic scattering events begin and end, which are then translated to neutron energy values. The cut values are then written to an ASCII file which is read by a *ScatterCutBuilder* class. The *LightYieldAnalysis* class has a *ScatterCutBuilder* has a member variable and support for reading the cut file.

The match window constraint is understood through Figure 7.12. Figure 7.12 shows a histogram of the results of evaluating Equation 4.14 without rounding the constant to the nearest integer. The histogram shows strong peaks surrounding integer solutions. These peaks correspond to events that are coincident observations involving n-p elastic scattering in the target detector. Additionally, the histogram shows a significant underlying background. Much of this background is removed if a constraint on the difference between the expected and calculated time of flight is imposed, by selecting regions of this histogram with the peaks corresponding to the correct target interaction. This provides the strongest rejection criteria for events not corresponding to the reaction of interest.

Following the development of the cut file, all of the reduced independent experimental data files are loaded into memory in the form of a ROOT TChain. The cut class is then

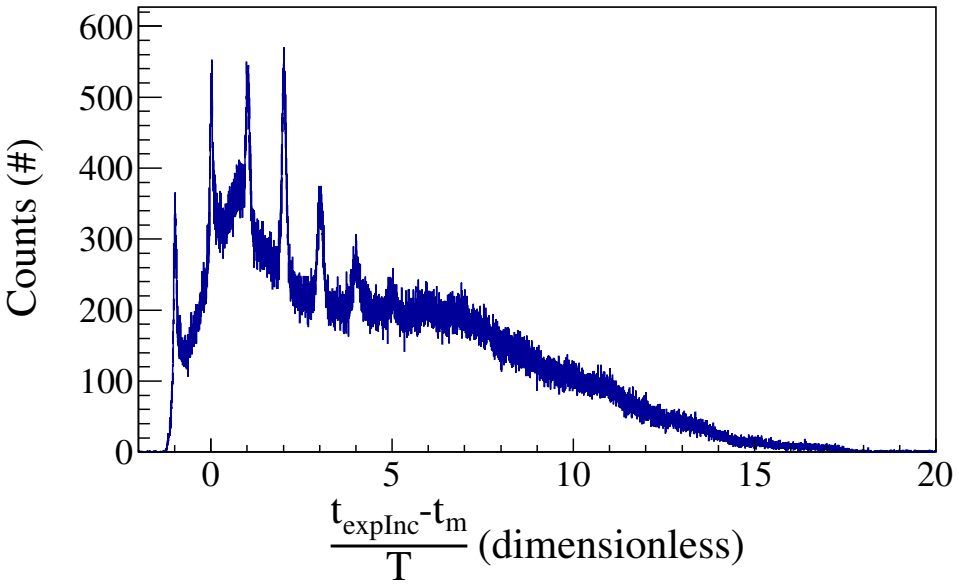

Figure 7.12: This histogram shows the number of observed events corresponding to a match on a given cyclotron period offset, as well as background events which fall in between integer values.

read into memory and the *LightYieldAnalysis::reduceTreesWithCuts* algorithm is run. The *LightYieldAnalysis::reduceTreesWithCuts* algorithm loops over all events in the TChain, i.e., all of the events in all files, and constructs a new TTree of *DDAQScatterEvents* that includes only events that meet the criteria outlined above. This TTree is written to a single file represented by the 'Reduced Data Set' box in Figure 7.1. Reproducing Figure 7.11 with the reduced data set, shown in Figure 7.13, demonstrates a much cleaner representation of the relationship of interest. The result provides a much higher signal-to-background ratio for events of interest. The difference is well illustrated when comparing a projection of Figure 7.11 to a projection of Figure7.13 onto the pulse integral axis, shown in Figure 7.14. The projection before constraints are applied shows a small feature on top of a large background, while the reduced data show a clear peak corresponding to the n-p elastic scattering events occurring in the energy range covered by the projection.

The remaining efforts in the analysis involve transforming the pulse integral axis to MeVee and developing an appropriate discretization of the proton energy dimension. First, the pulse integral will be addressed.

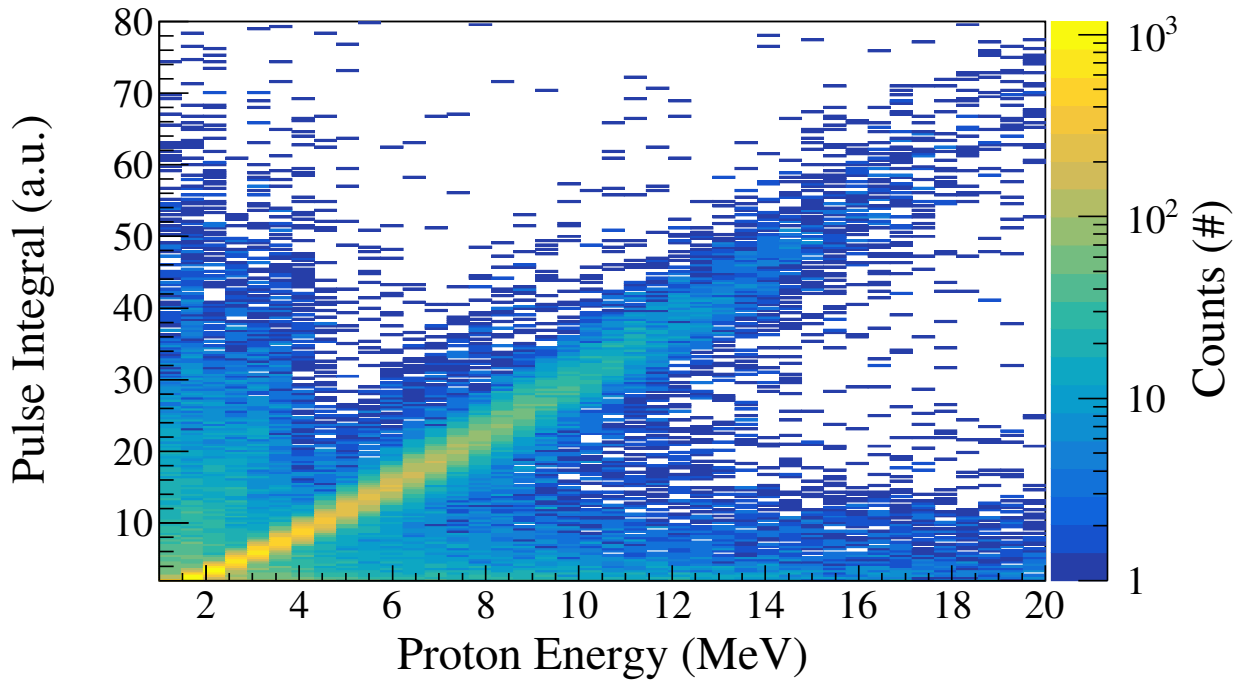

Figure 7.13: A histogram of the target pulse integral vs. proton energy giving a light yield result for the reduced data set for Target 0 (EJ309) with all cuts applied. The significant background observed in 7.11 is dramatically reduced.

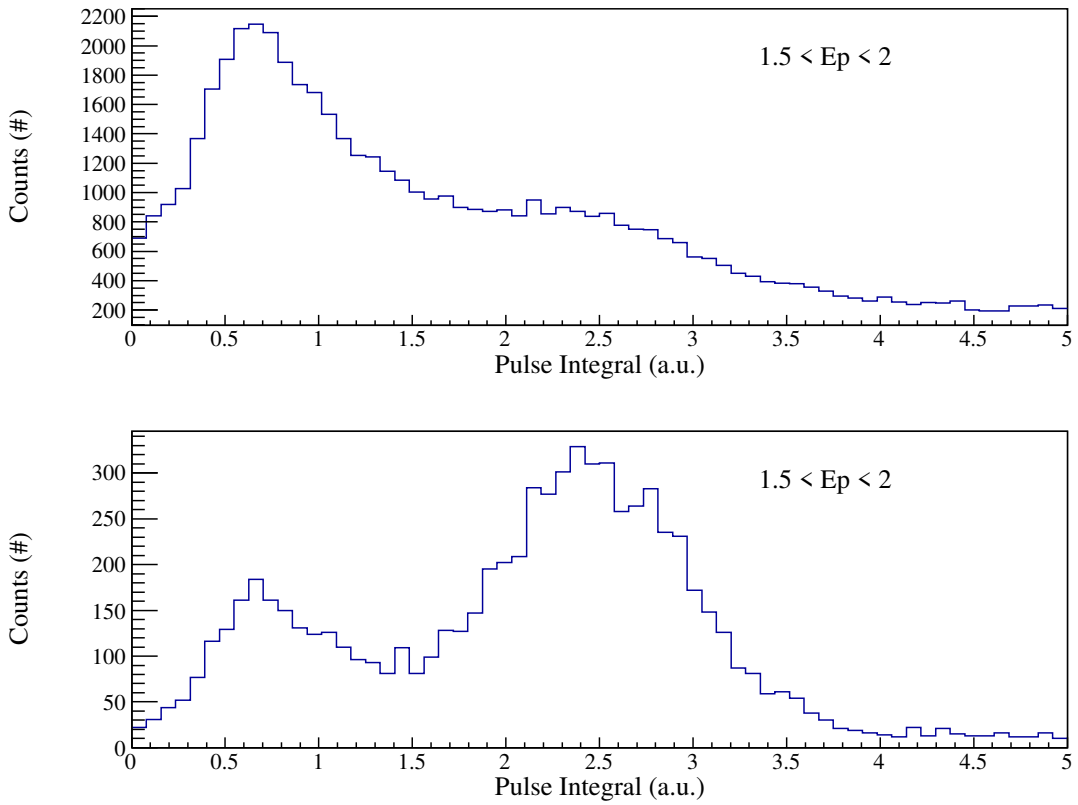

Figure 7.14: Comparison of a projection of Figure 7.11 (top) and Figure 7.13 (bottom) illustrating the necessity of reducing background events. The data before constraints are applied shows a signal-to-background ratio for the n-p elastic scattering events of ∼1:5, while the reduced data show a clear feature with a signal-to-background of ∼6:1.

7.6 Pulse Integral Data Reduction and Calibration

The γCF anticipates histograms of observations of known γ rays. The sources used here are detailed in Sec. 5.5. This section focuses on the reduction from raw waveform data to pulse integral spectra and the results produced by the γCF. As two integration lengths were considered, the reduction and calibration procedures were completed independently with each integration length. The waveforms were reduced to *DDAQProcEvents* using the same algorithms used to reduced the experimental waveform data. Following this, the events were accumulated into pulse integral spectra using a developed support class, *DigMeVeeCalibSupport*, which reads a setup file directing the accumulation across multiple data files for different sources. The file used in this analysis is provided in Appendix C.

The accumulated γ-ray spectra for the ^{137}Cs, the aluminum activation, and the AmBe source as observed by Target 0 with a 300 ns integration length are shown in Figure 7.15. These empirical inputs correspond to the simulation results shown in Figure 6.3, and both are needed as inputs to the γCF. The aluminum activation is also present in the collection of AmBe data; thus, the range used in the minimization was selected to bound the Compton edge and double escape peak. The 1.368 MeV γ ray from the activated aluminum has a strong overlap with other activation reactions and background in the experimental area, so the range of the minimization included for the aluminum activation was limited to include only the Compton edge and double escape peak of the 2.754 MeV γ ray. The aluminum activation provided a strong background to the ^{137}Cs data, so it was subtracted to produce a clean spectrum. The range for the minimization was selected to focus on the Compton edge with regard to the ^{137}Cs data.

The results of the χ^2 minimization between the input data shown in Figure 7.15 and the simulated spectra shown in Figure 6.3 are given in Figure 7.16. The corresponding plot for Target 1 is shown in Figure 7.17. Both of these plots show the result considering a 300 ns integration window, and the resulting agreement between the data and the model is similar for the two targets. The resultant parameters from the calibration procedures are summarized in Table 7.2. The uncertainties produced by HESSE are surprisingly small [27] and χ^2 contour plots were generated to explore if this was an error caused by potential issues in the objective function. The χ^2 contour plots showed that the represented values did correspond to changes in χ^2 of one, suggesting that these values do reflect the statistical error. The reported errors do not take into account any potential systematic effects, such as those described in Chapter 6.

7.7 Proton Energy Discretization and Reduction to Data Points

The next effort in the analysis involves the reduction of the two-dimensional histogram seen in Figure 7.13, transformed by pulse integral calibrations, to a series of data points with error that reflect the proton energy resolution discussed in Sec. 6.4. This is accomplished

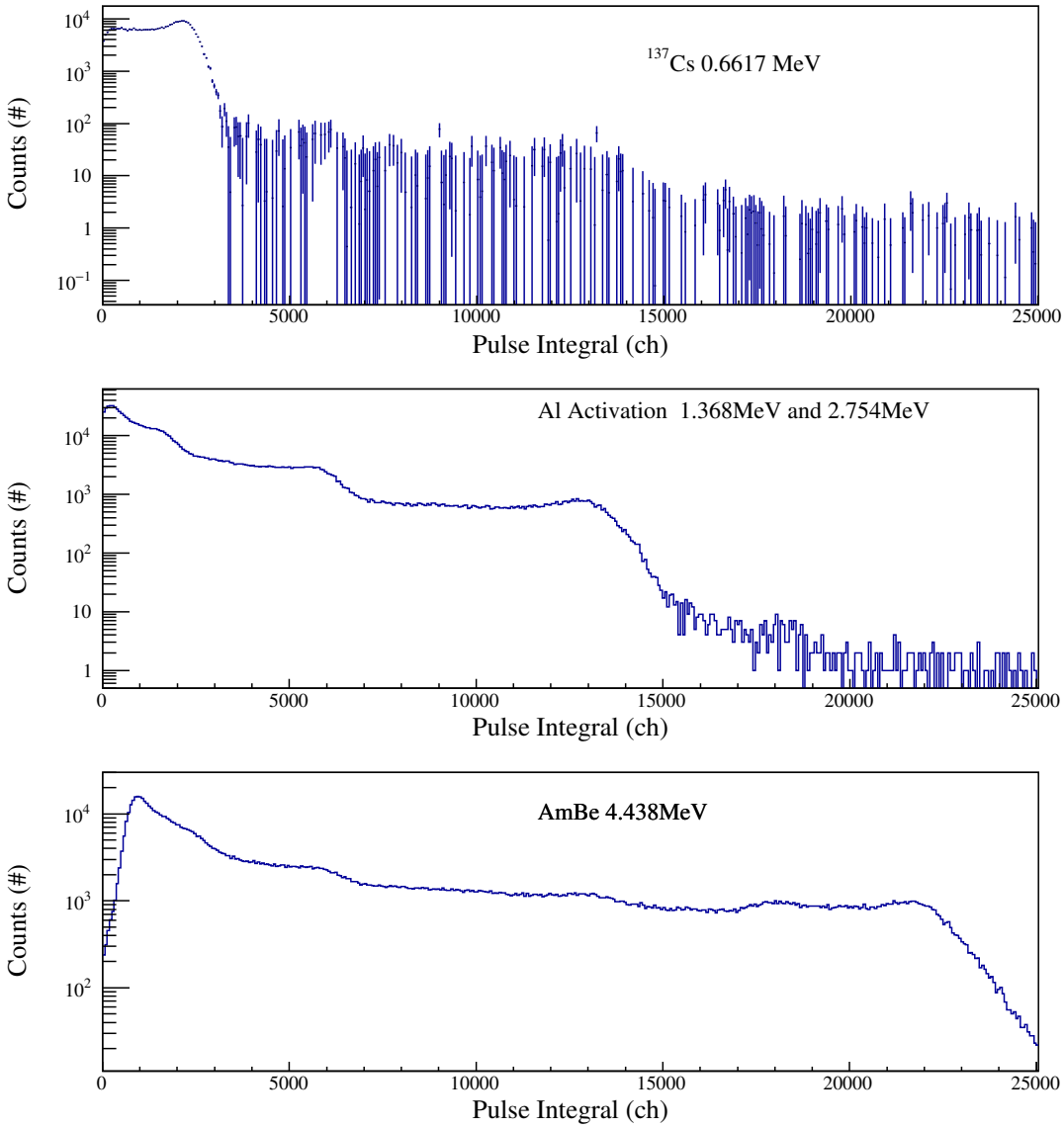

Figure 7.15: The conditioned input data for the γCF for Target 0, where the data has been integrated with a 300 ns integration window. These are the experimental data required for comparison with Figure 6.3.

	300 ns Integration		30 ns Integration	
Parameter	Target 0	Target 1	Target 0	Target 1
a	0.000186	0.000217	0.00023	0.00026
b	0.033	0.0336	0.023	0.024
σ_a^2	3.8×10^{-17}	3.8×10^{-18}	5.6×10^{-16}	3.12×10^{-16}
σ_b^2	2.3×10^{-9}	5.02×10^{-11}	1.0×10^{-8}	6.3×10^{-8}
σ_{ab}	-2.24×10^{-15}	-1.72×10^{-15}	-1.84×10^{-13}	-4.4×10^{-12}

Table 7.2: Summary of pulse integral calibration results for multiple integration lengths for both of the target detectors for EJ309.

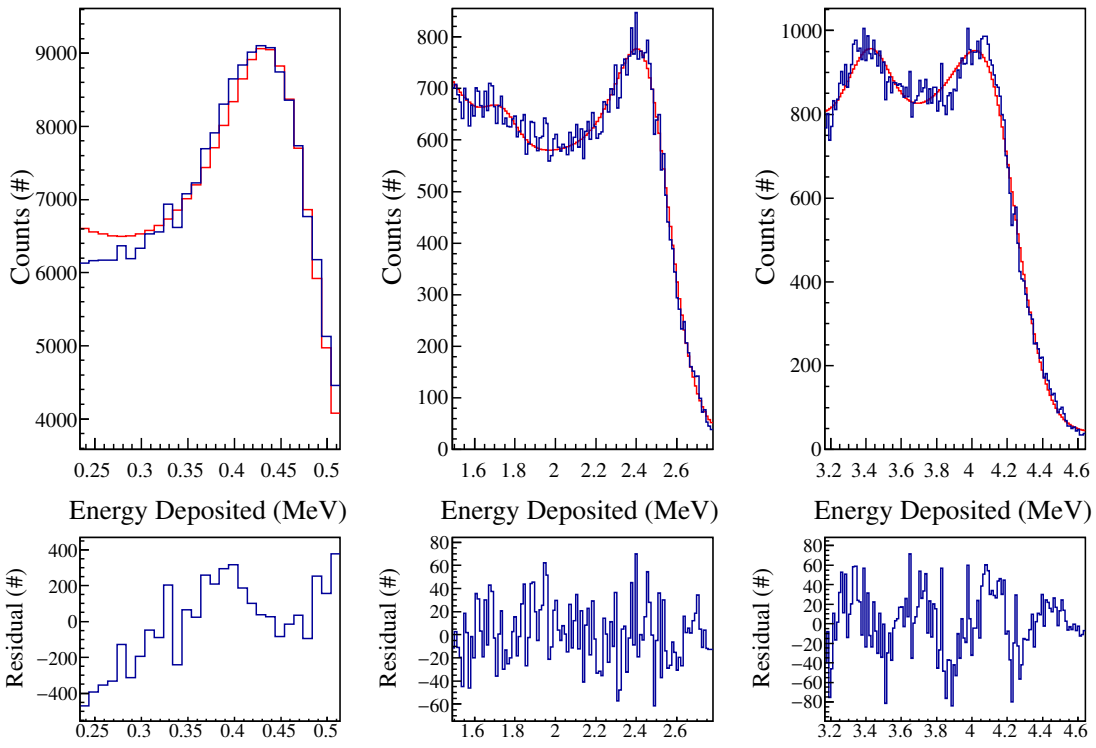

Figure 7.16: The results of a χ^2 minimization between the γ-ray data collected with the detector used as Target 0, reduced with a 300 ns integration window, and the simulation-based model results described in Sec. 5.5. The blue line in the top plots is the experimental data while the red line is the simulation-based model. The bottom panel is the residual between the simulation and experimental data for the plot directly above.

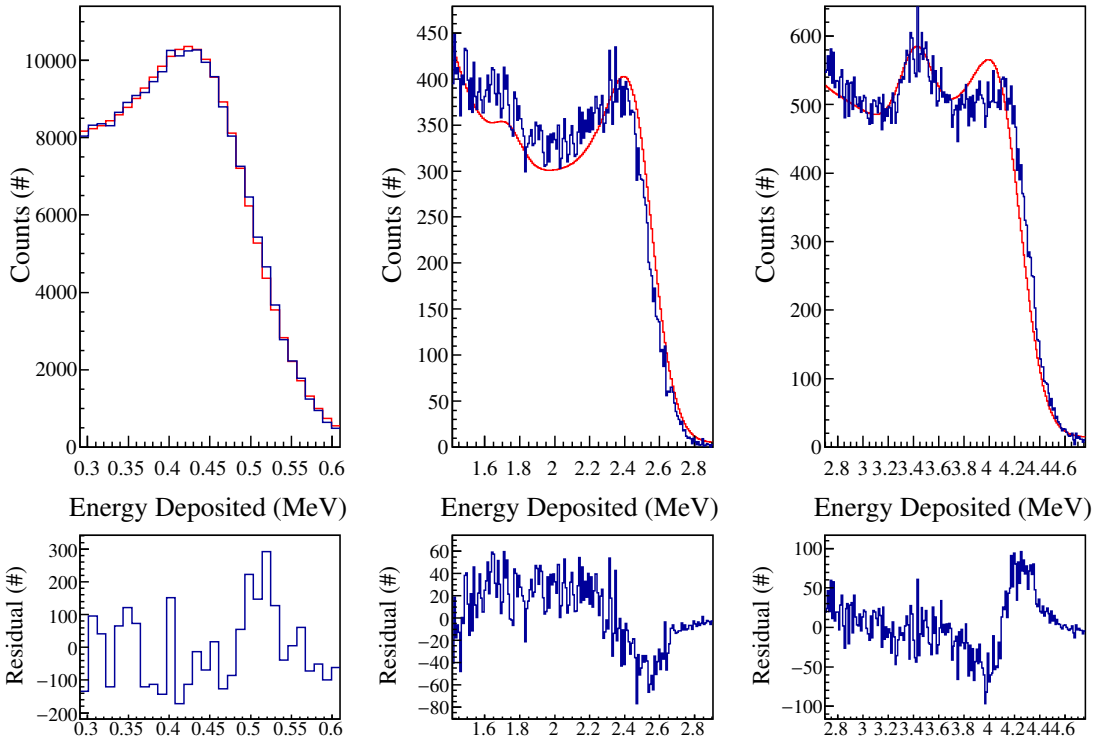

Figure 7.17: The results of a χ^2 minimization between γ-ray data collected with the detector used as target 1, reduced with 300ns integration window, and the simulation-based model results described in Sec. 5.5. The blue line in the top plots is the experimental data while the red line is the simulation-based model. The bottom panel is the residual between the simulation and experimental data for the plot directly above.

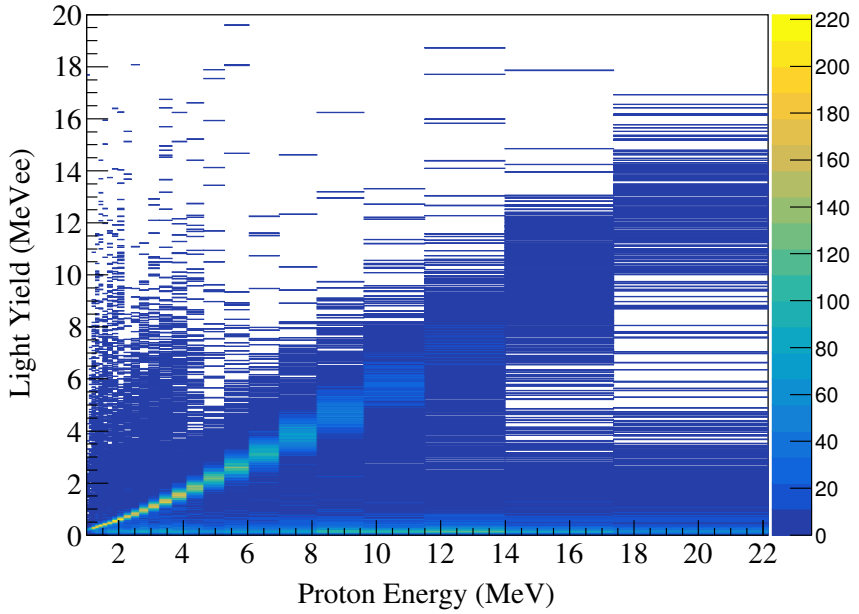

Figure 7.18: Results of accumulating the pulse integral calibrated data into a histogram with bin dimension in the proton energy axis corresponding to the proton energy resolution.

by taking a series of projections and estimating the centroid of the feature corresponding to the n-p elastic scattering band. This is accomplished by first re-accumulating the pulse integral calibrated data in a histogram with a non-uniform bin structure with regard to the proton energy axis. The result of the re-accumulation of the data for Target 0 is shown in Figure 7.18. This is the starting point for the reduction. A projection of each proton energy bin was made and a χ^2 minimization was performed between the histogram and a normal distribution superposed with a cusped power law. The fit function, B_i, for the ith projection is specified as:

$$B_i = \begin{cases} ab^{(c-d)}x^d + Ae^{-\frac{1}{2}(\frac{x-\mu}{\sigma})^2} & x \leq b \\ ax^c + Ae^{-\frac{1}{2}(\frac{x-\mu}{\sigma})^2} & x > 0, \end{cases} \tag{7.9}$$

where a, b, c, and d are nuisance parameters, μ is the centroid of the n-p elastic scattering distribution (i.e., the parameter of interest), and σ is the width of the distribution. A characteristic fit of a representative projection is shown in Figure 7.19.

The algorithm responsible for the projection and fitting, *LightYieldAnalysis::fitSlices*, has two modes. The first mode attempts to estimate the parameters of a specified bin, usually near the center, as a starting point for the minimization using derivative peak finding. Then the algorithm steps through projections in the positive direction first using the last fit parameters as a seed for the next fit. After this, it uses the initial fit of the specified bin then stepping down through the slices, again using the previous fit as a seed to start the next fit. There is an option to highlight problem slices, where the algorithm needs user attention for limit and seed setting. The other mode for running the algorithm takes a list of starting

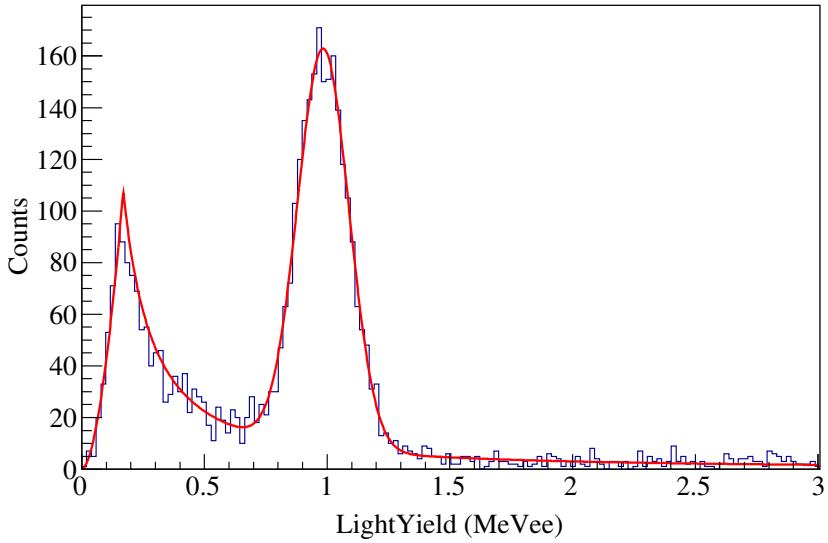

Figure 7.19: Results of fitting a slice of Figure 7.18 with Equation 7.9. The blue line represents the histogrammed data and the red line is Equation 7.9 with a set of best fit parameters.

points for the minimization and iterates through the bins setting the given parameters as the starting points with limits set to be ±50% of the original guesses. Regardless of the operational mode, the results of the algorithm is a vector of vectors of doubles, where element [0][i] is the center of the ith bin, element[1][i] is the ith estimated mean of the normal distribution, element [2][i] is the ith bin width, and [3][i] is the parameter error estimate reported by MINUIT [27]. These make up the desired result: a series of data points and error bars representing the proton light yield of the target. The resultant data is shown plotted on top of the original histogram from which the data points are estimated in Figure 7.20. Additionally, a plot of the resultant data points and statistical error bars is shown in Figure 7.21.

7.8 Monte Carlo Assessment of Systematic Contributions to Error

To estimate the systematic error on the light yield determination, the following sources of potential systematic bias were identified:

- Uncertainty on detector positions (x, y, z)
- Distance from the (0,0,0) point in the coordinate system to the breakup target
- Uncertainty on the incoming time of flight calibration constants

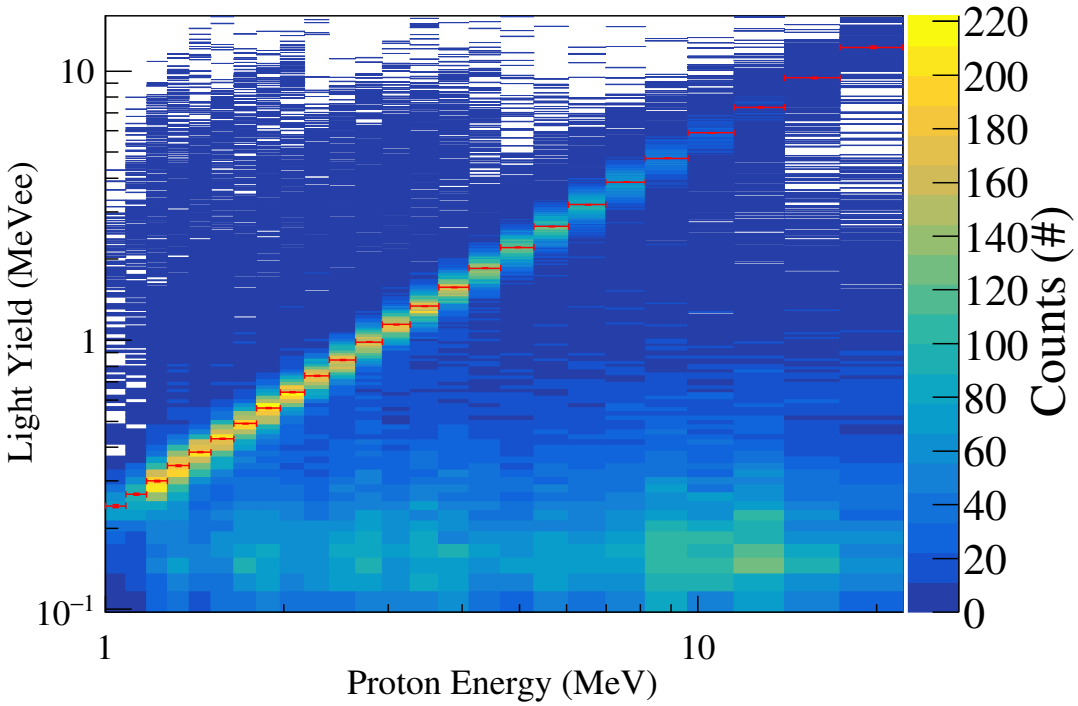

Figure 7.20: Figure 7.18 shown with the results of estimating the centroids of the distribution corresponding to n-p elastic scattering events. The error bars shown in the light axis represent the statistical uncertainty only, while the proton energy error bars are the bin widths corresponding to the proton energy resolution.

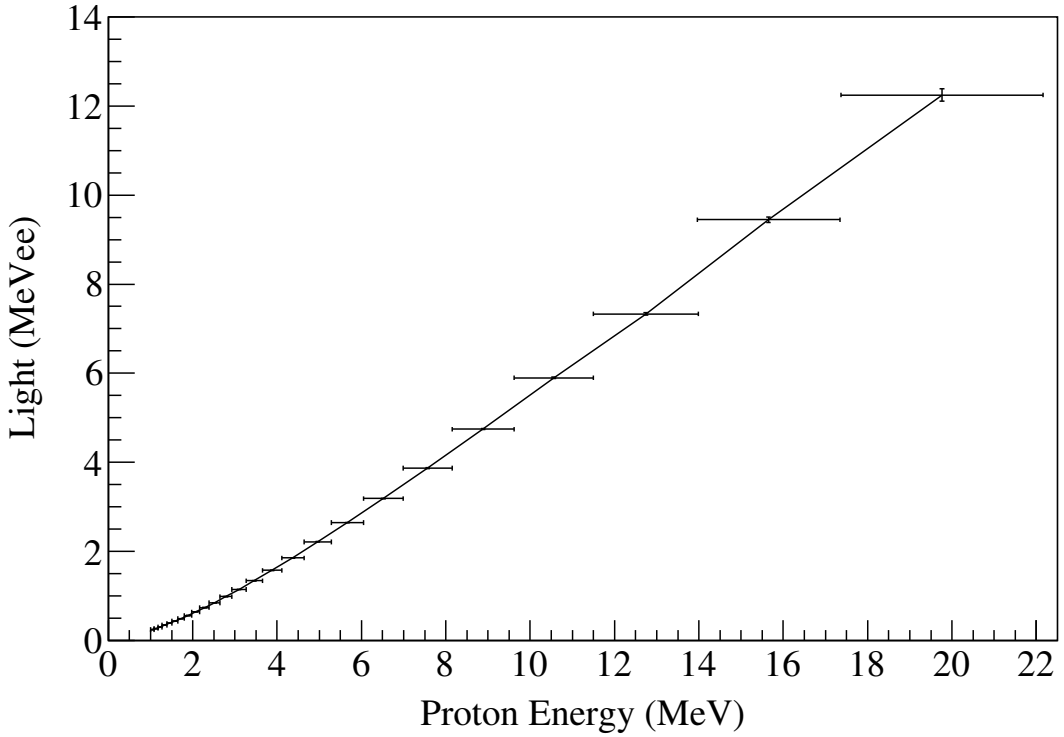

Figure 7.21: The results of estimating the centroids of the distribution corresponding to n-p elastic scattering events. The error bars shown in the light axis represent the statistical uncertainty only, while the proton energy error bars are the bin widths corresponding to the proton energy resolution.

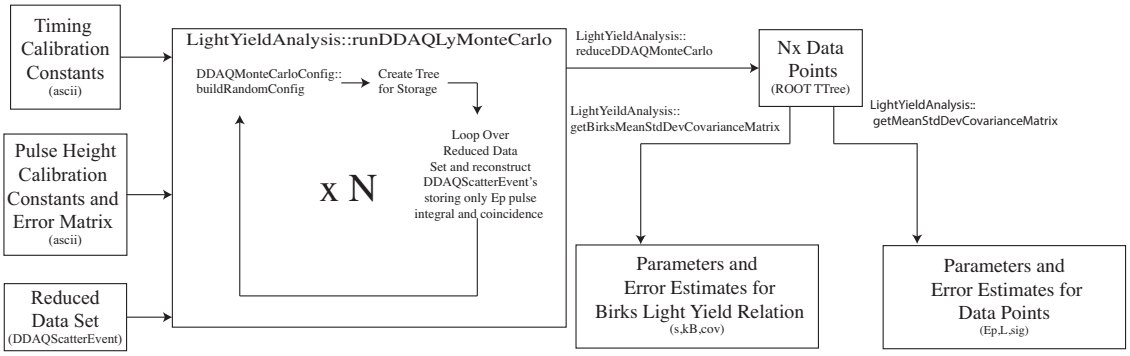

Figure 7.22: Overview of the steps and algorithms developed and used to characterize the systematic uncertainty on the proton light yield data points as well as model parameters for the semi-empirical model given by Equation 2.3.

- Uncertainty on the outgoing time of flight calibration constants
- Uncertainty on the pulse integral calibration parameters

To address the contributions of these uncertainties to the uncertainty on the measurement, a Monte Carlo code was developed to re-analyze the data while sampling the probability distributions of the error on the input parameters listed above. For each integration length considered, 3000 Monte Carlo trials were run where the above inputs to the calculation were randomized based on their uncertainty. Then the resultant data points were re-calculated with the randomized input parameters. Finally, the variation in the resultant data points was used to characterize the effect of these uncertainties, as well as their effect on parameters of the semi-empirical model given in Equation 2.3. Figure 7.22 shows an outline of the developed code responsible for the Monte Carlo assessment of the systematic uncertainty.

The algorithm responsible for the Monte Carlo assessment, *LightYieldAnalysis::runDDAQLyMonteCarlo*, begins by reading the reduced data set, the detector configuration, and the uncertainties into memory. The main class responsible for the randomization is *DDAQMonteCarloConfig*, which is a child class of *DDAQScatterConfig*. It effectively reconstructs a detector configuration and parameter set for the analysis on each trial. The sources of uncertainty were reduced, as much as possible, to an orthogonal basis so that the resultant data could be assessed with regard to covariance and correlation. For example, the measured detector locations, which are independently determined, and their associated uncertainties were used, as opposed to quantities derived from the locations such as angle and flight path. If the latter had been used, the uncertainties would necessarily have some correlation as they are derived from the same measurements. The only identified systematic contributions where this was not possible was the pulse integral calibration parameters. These have a correlation as they are derived through parameter estimation, so it was necessary to sample them in a way that preserved the correlation. Additionally, the pulse integral calibration error matrix produced through the minimization did not reflect the types of potential systematic bias discussed and explored in Chapter 6. To account for this, the error matrix produced in the

parameter estimation was scaled to reflect the observed systematic uncertainty before it was used in the Monte Carlo assessment.

To sample preserving correlations, a Cholesky decomposition of the scaled error matrix was performed. Then, to obtain a set of random parameters, the product of the upper triangular component of the Cholesky decomposition was multiplied into a vector of randomly sampled normal distributions with $\mu = 0$ and $\sigma = 1$. This was then added to the original means. Sampling of the normal distribution for both the pulse integral randomization and the other parameters was handled using the C++ *std::algorithm* header. The random number generator used was the Mersenne Twister pseudo-random number generator implemented through that header [37]. For the rest of the parameters, the C++ normal distribution was centered at the appropriate mean with widths representative of the experimental estimation of the uncertainties. For each trial in the Monte Carlo assessment, the full set of parameters were sampled at the beginning of the trial.

After obtaining a new set of randomized parameters with the appropriate correlation, the algorithm rebuilds the scatter coincidence map containing the new randomized set of inputs required for constructing *DDAQScatterEvent*s as previously discussed. The next step in *LightYieldAnalysis::runDDAQLyMonteCarlo* is to loop back over the data and recalculate the physics quantities listed in Sec. 7.4. The reconstructed scatter events are not stored for all trials, but are only temporary memory residents. The algorithm builds a series of TTrees, each in a single file. Each tree represents calculations from an independent trial and stores an associated list of data. The data stored in each tree is only the proton energy in MeV, the light in MeVee, and the angle identifier needed to sort independent targets when accumulating the data. This was done to reduce the amount of data stored on disk while providing a checkpoint state.

The next step in assessing the uncertainty is the reduction to data points. This is handled as described in Sec. 7.7. To ensure the minimization was stable, parameter maps of the original fits to the data were fed to the slice fitting algorithms. They are then used as seeds for the minimization. When re-accumulating the data for the slice fitting algorithm, the discretization of the histogram was left fixed. The resutant vector of vector of doubles corresponding to the data point estimates of the distributions are stored in a TTree, where the individual events correspond to individual trials.

Finally, with a randomized set of results corresponding to the list of experimental uncertainties, several quantities can be estimated. The mean, standard deviation, covariance matrix, and correlation matrix were generated from the result. The mean for a point is given as:

$$\mu_j = \frac{1}{N} \sum_{i=0}^{N} L_{ij}, \tag{7.10}$$

where μ_j is the mean of the jth data point in MeVee, N is the number of trials, and L_i is the light yield result for the ith trial corresponding to data point j in MeVee. The standard

deviation is given as:

$$\sigma_j = \frac{1}{N}\sum_{i=0}^{N} L_{ij} - \mu_j, \tag{7.11}$$

where σ_j is the standard deviation of the jth data point in MeVee. An element of the covariance matrix is given as:

$$\sigma_{jk} = \frac{1}{N}\sum_{i=0}^{N}(L_{ij} - \mu_j)(L_{ik} - \mu_i k), \tag{7.12}$$

where σ_{jk} is the covariance between point j and point k in MeVee^2. An element of the correlation matrix, ρ_{jk}, is given as:

$$\rho_{jk} = \frac{\sigma_{jk}}{\sigma_j \sigma_k}. \tag{7.13}$$

An additional potential systematic bias exists based on the chosen bin structure of the proton energy axis. If the observed events in the bin do not form a uniform distribution across the bin, the resultant observed light yield is not well represented by a data point at the centroid of the bin. To address this, the proton energy value for the data point was taken as the average proton energy for all events that were considered in a given bin for all trials of the Monte Carlo assessment. This offsets the center of the reported data point to reflect the non-uniformity of the distribution of events considered for the data point. Additionally, the independent light yield trials were fit using a χ^2 minimization between the data points with statistical error and the semi-empircal Birks relation given by Equation 2.3. This allows the construction of an error matrix for the parameter estimation of S and kB.

In summary, the Monte Carlo assessment of the systematic uncertainties produces several results. The data shown in the following plots correspond to Target 0 for EJ309 using a 300 ns integration window. The first result is a series of data points corresponding to the means from all trials as well as standard deviations shown in Figure 7.23. The next result is a covariance matrix associated with these data points, shown in Figure 7.24. Finally, the correlation matrix is shown in Figure 7.25. These results provide the basis for presenting a well characterized light yield for the samples measured here and a characterization of the method.

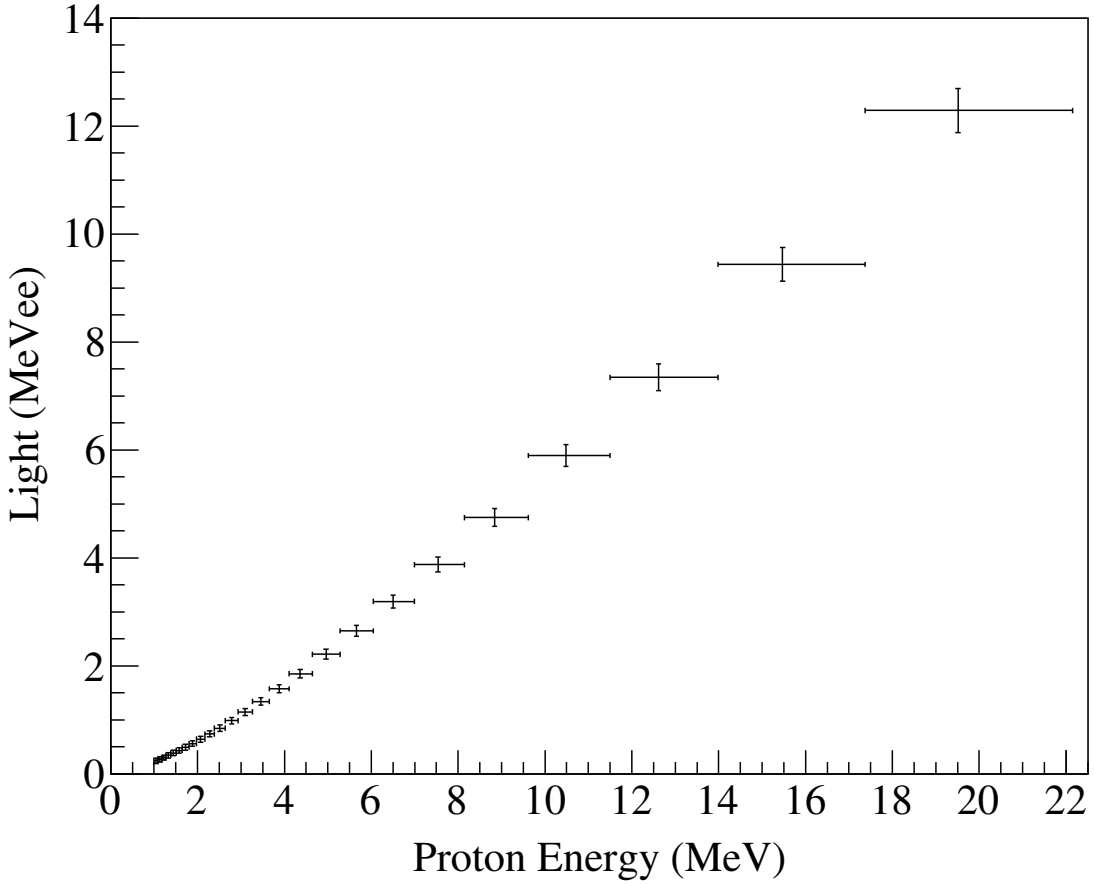

Figure 7.23: The series of μ and σ generated by Monte Carlo of the systematic uncertainties for Target 0 of EJ309 considering a 300 ns integration window.

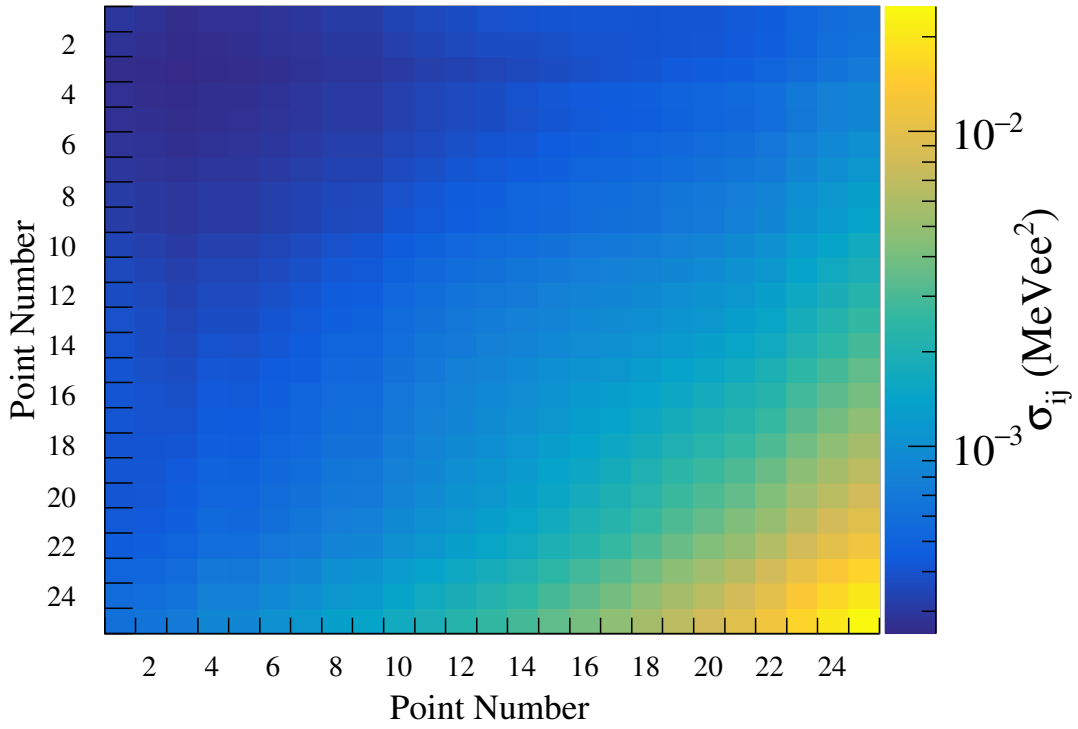

Figure 7.24: The variance-covariance matrix representing the result of a Monte Carlo assessment of the systematic uncertainty.

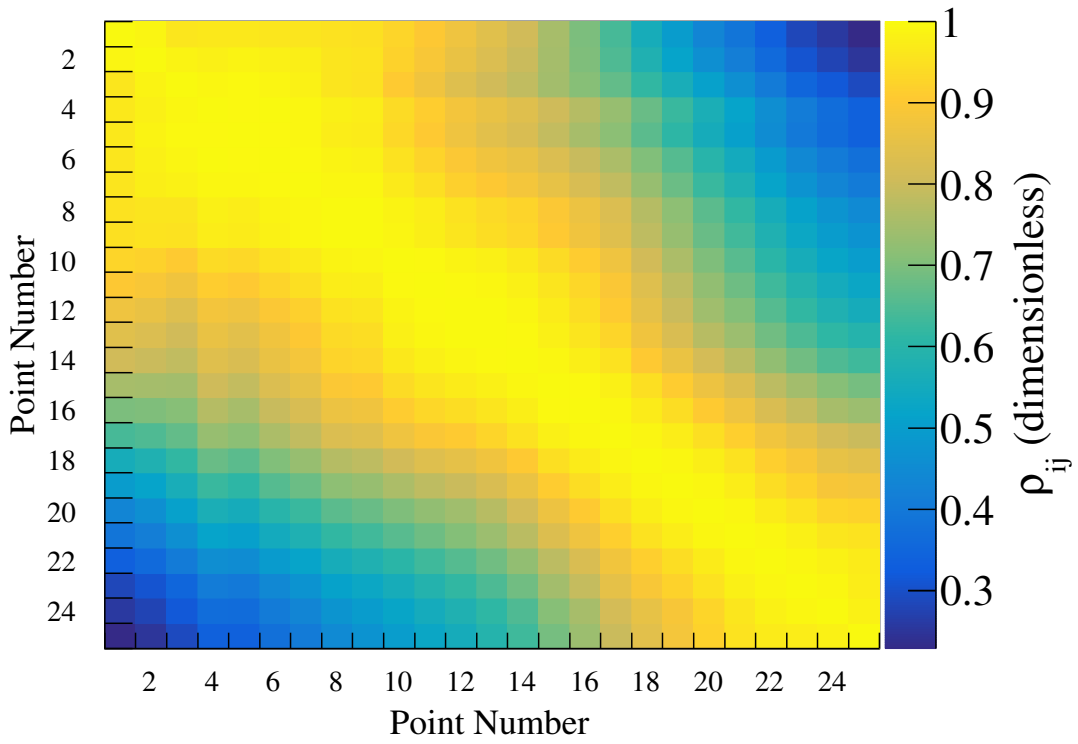

Figure 7.25: The correlation matrix representative of the result of a Monte Carlo assessment of the systematic uncertainty.

Chapter 8

Results, Summary, and Outcomes

The results of the work presented here are twofold. The first outcome is the establishment and benchmarking of a novel extension of indirect light yield measurements–the double time of flight method outlined in Sec. 4.5. The results of the application of the method to measurements of EJ301 and EJ309 with a characterization of the statistical and systematic errors will be presented and discussed in this chapter. The second outcome is the engineering and development of a system for producing light yield measurements exploiting this method at the 88-Inch Cyclotron. The status of the system will be discussed and the implications for future work will be explored.

8.1 Light Yield Results and Discussion

The data products resulting from this work include a series of light yield measurements for EJ301 and EJ309 considering multiple integration lengths, as well as distributions of model parameters corresponding to these data using the semi-empirical relation from Birks given in Equation 2.3. The proton light yield for EJ301 is presented in Figure 8.1. The classic measurement from Verbinski et al. [14] is also shown, extracted from the authors' data table and converted to MeVee using the preferred conversion factor from Dietz et al. [30]. Additionally shown is the best fit parameter result for NE-213 from Scherzinger et al. [17]. Over the full scale of the measurement, shown in Figure 8.1a, the double time of flight method is in good general agreement with the results for an equivalent material, NE-213. In the low energy range, shown in Figure 8.1b, the data are in good agreement with the results from Scherzinger et al. [17], who concluded that individual detectors require individual measurements. At the lower energies, a systematic difference is observed between the measurement of Verbinski et al. [14] and the double time of flight method, although nearly all data are within the estimated uncertainty. Another feature shown is the large difference in the result between a short and long integral. In the NE-213 measurements, results using short integrals or pulse amplitude are not present.

The proton light yield measurements for EJ309 are shown in Figure 8.2 along with the results of best fit parameters from Pino et al. [1], Takada et al. [38], Lawrence et al. [39],

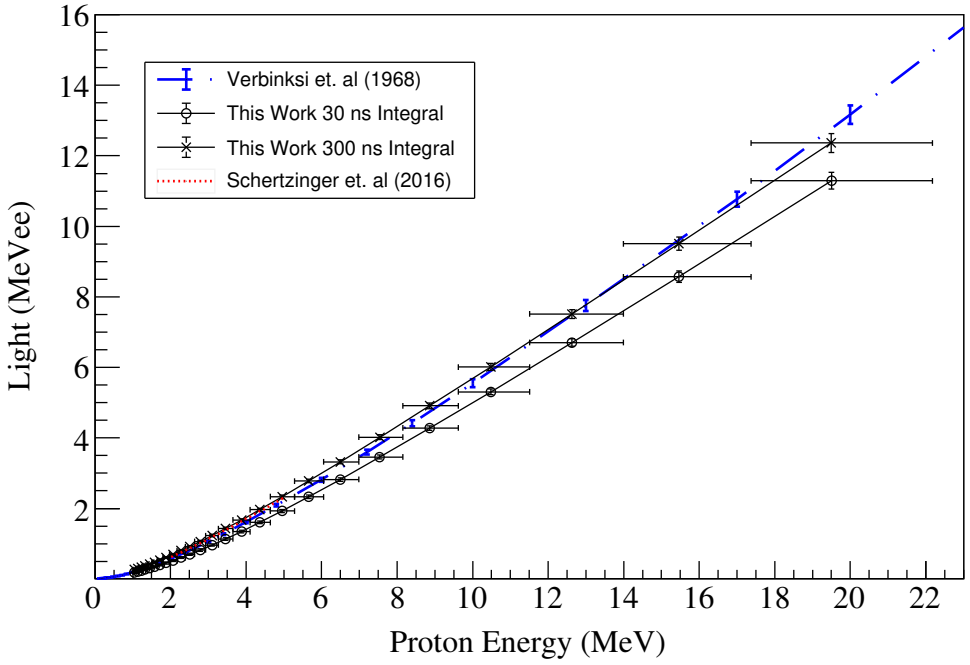

(a)

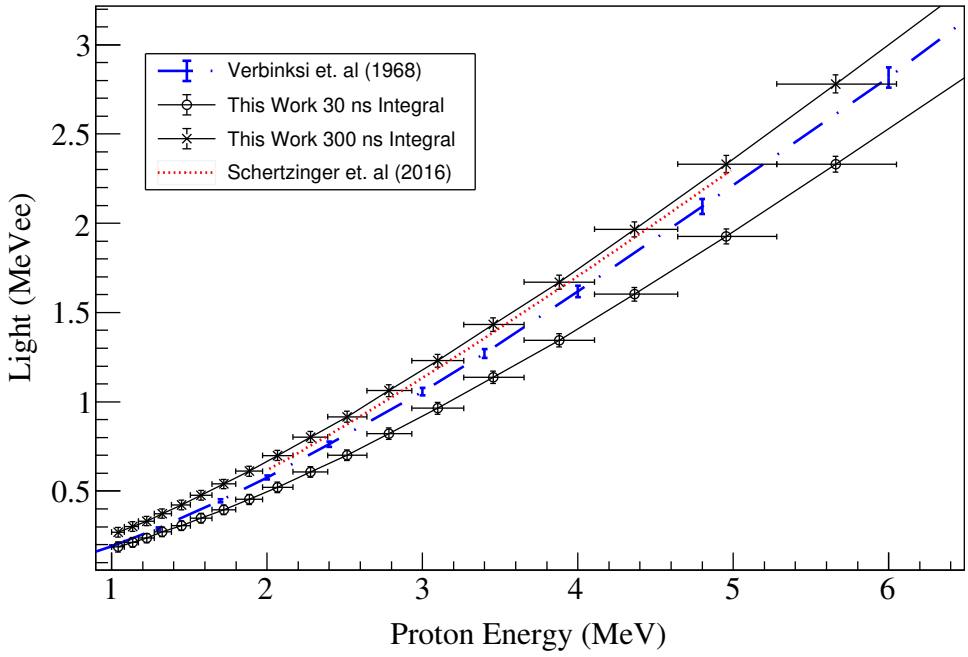

(b)

Figure 8.1: EJ301 proton light yield.

Norsworthy et al. [26], Bai et al. [18], and Tomanin et al. [24]. Figure 8.2a shows the high energy range of the measurement from approximately 1 to 20 MeV and Figure 8.2b shows the same data focused on the lower energy range up to 6 MeV. At first glance, the conclusion from Bai et al. [18] that the community has not converged on a material specific property of the detection medium is compelling. But careful attention to the pulse processing chain used by the various authors prompts a different conclusion. The results cluster around two different regions corresponding to the integration length used in the pulse processing chain. This is most easily observed in the low energy range shown in Figure 8.2b. The exception to this is the result from Pino et al. [1], who references an external paper with regard to the signal processing chain that is not explicit about the integration length. Looking specifically at the broader energy range plot for the EJ309 proton light yield, shown in Figure 8.2a, the one high energy measurement explicit about their pulse processing chain from Tomanin et al. [24] agrees well with the results established in this work. Interestingly, Tomanin et al. [24] measured a large cubic detector, and when comparing to the literature, concluded that the difference they observed was due to the shape and size of the detection medium. However, the comparisons were made to measurements performed by Enqvist et al. [16] (see Figure 3.3), which used the maximum observed element of the waveform as representative of the size of the pulse. Thus, the notion that detectors of different shapes and sizes require different measurements is not supported by the measurements presented here. It is also worth noting that the measurements presented here, with the exception of Takada et al. [38], are edge characterization methods. The only author that incorporates a feedback mechanism between a Monte Carlo simulation of the neutron response functions and the observed response functions is Bai et al. [18], who note deviations of up to 8% on the originally considered values. The short integral comparison here is in excellent agreement with both Bai et al. [18] and Takada et al. [38], the latter of which was a direct measurement. Considering this, along with the variation in calibration procedures, the notion that proton light yield is a detector-specific quantity is not supported.

Comparing the proton light yield results with results from the literature helps to disentangle some of the open questions regarding measurements of proton light yield. The very good agreement between the current work and Scherzinger et al. [17], Takada et al. [38], Bai et al. [18], and Tomanin et al. [24] suggest that the postulate that measurements must be made on a case-by-case basis is not supported. The results presented here completely bound the literature regardless of detector size, detector shape, readout system used, or method used with a change of a single parameter in the pulse processing chain: the integration length. There are two exceptions to this. The data of Enqvist et al. [16] and its re-interpreted calibration by Norsworthy et al. [26] lie below the measurements presented here and show much additional curvature. The pulse processing chain used for both of these results take the maximum of the waveform as characteristic of the pulse. With the readout systems employed, this will be proportional to the maximum photon fluence, not the number of photons produced. Additionally, the analysis used a single calibration point at the bottom of the range to scale the full range of the measurement. Outside of this exception, the data generally fall into two categories– short integral and long integral–and the measurements

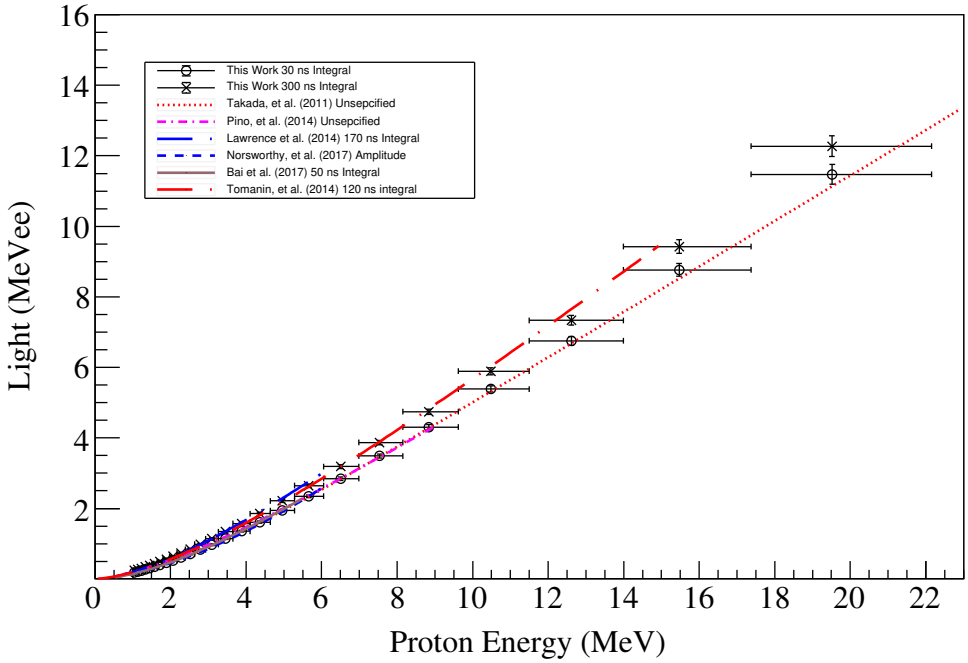

(a)

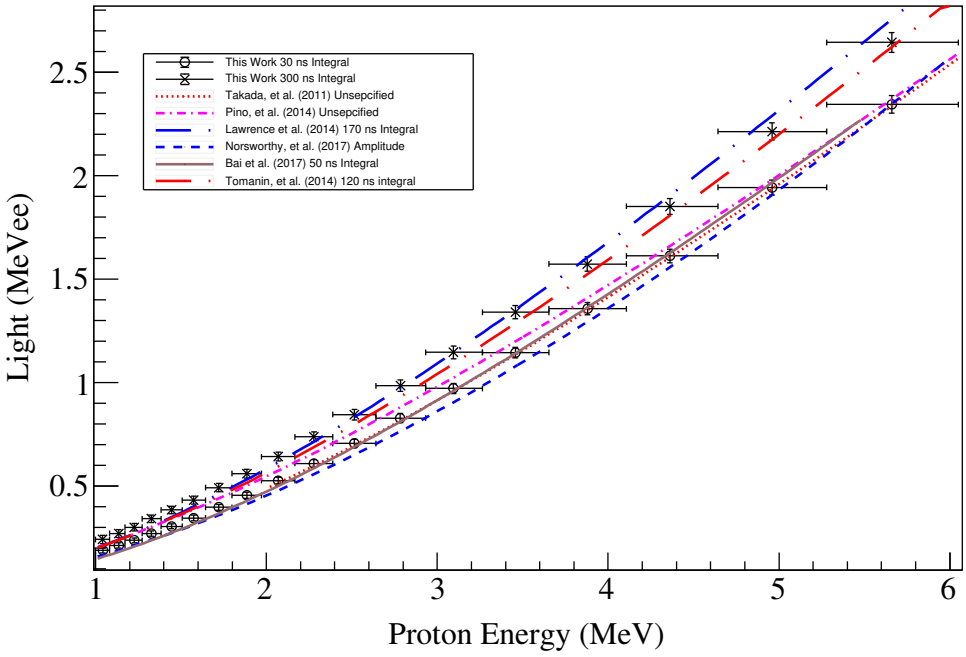

(b)

Figure 8.2: EJ309 proton light yield.

	300 ns Integration		30 ns Integration	
Parameter	EJ309	EJ301	EJ309	EJ01
S $(\frac{\text{MeVee}}{\text{MeV}})$	0.98	0.94	1.11	1.14
kB $(\frac{\text{mg}}{\text{cm}^2\text{MeV}})$	7.5	6.2	12.0	12.9
σ_s^2 $(\frac{\text{MeVee}}{\text{MeV}^2})$	0.01	0.0066	0.01	0.09
σ_{kB}^2 $(\frac{\text{mg}}{\text{cm}^2\text{MeV}^2})$	3.6	1.8	3.6	3.7
σ_{skB} $(\frac{\text{mg MeVee}}{\text{cm}^2\text{MeV}^2})$	0.18	0.11	0.18	0.19

Table 8.1: Summary of Birks parameterization (Eq. 2.3) of the proton light yield measurements for EJ309 and EJ301 for 300 ns and 30 ns integration lengths.

agree within the uncertainty on edge characterization methods established by Bai et al. [18] through a feedback loop with a Monte Carlo simulation of the anticipated responses. Additional differences among these clusters can likely be attributed to the lack of standardization in calibration procedures.

The EJ301 and EJ309 light yield measurements presented in this work were also characterized with model parameters derived from fitting the Monte Carlo trials of the systematic uncertainty analysis with the semi-empirical relation from Birks. The resultant parameters as well as the elements of the resulting variance-covariance matrix are summarized for the EJ309 and EJ301 proton light yield data with both 30 ns and 300 ns integration lengths in Table 8.1. The dramatic difference in both the scintillation efficiency and quenching parameters for short and long integrals comes from the treatment of the delayed light. If short integrals of the waveforms are used, the delayed light emission is treated as quenched and as such, the quenching parameter is larger. If these model parameters are used in a statistical trial or comparison with other model data, care should be taken to include the correlation as the parameters are extremely dependent on each other. Figure 8.3 shows the probability distribution function corresponding to the Birks parameter analysis for the EJ309 proton light yield result using the 300 ns integration length. The strong correlation requires consideration when using the results presented here for either assessing error on quantities produced from these results or when making a comparison between other light yield measurements.

The Birks model demonstrates anticipated physically-relevant features when considering long integrals. First, the S value from the Birks relation is very near unity. This is the anticipated result when working in the relative unit of MeVee, as Birks initially postulated that S should be particle independent [5]. This suggests that Equation 2.3 could possibly

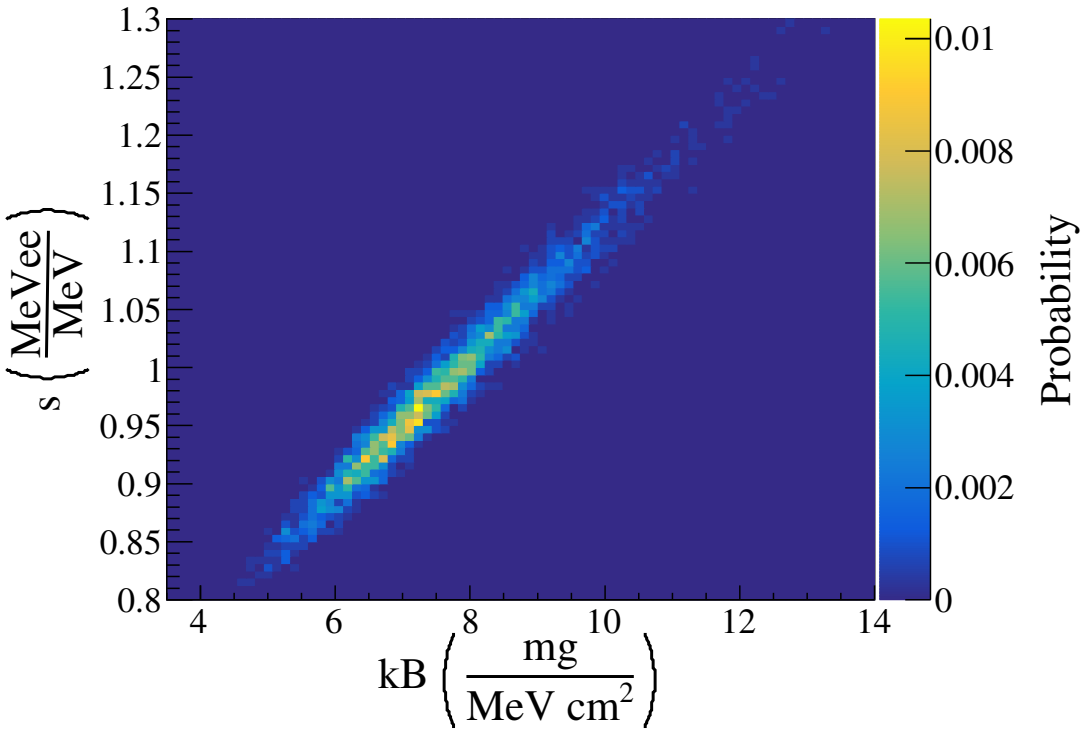

Figure 8.3: Probability distribution of the model parameters resulting from fitting the 300 ns integration length proton light yield data for EJ309 with the semi-empirical relation from Birks. The strong correlation requires consideration when propagating error using the parameters provided in this work.

be used for different heavy charged particles. However, it's worth noting that Birks later suggested there could be differences between S values for heavier ionizing particles [4]. The short integral Birks analysis suggest a higher relative scintillation efficiency, S, but a much larger kB value. This doesn't fit well with the anticipated physics for proton energy deposition that should include additional singlet quenching and increased delayed fluorescence due to the increased stopping power. This suggests that the model breaks down when the light from both prompt and delayed fluorescence is not considered. Regardless, the parameters provide a good empirical fit to the data over the energy range considered. The current measurements provide little insight into other regimes where Birks relation breaks down, e.g., for heavy particles ($A > 12$) and low proton energies (< 500 keV).

The results here suggest that the desire for a list of benchtop experiments that would allow the use of proton light yield in analysis for a specific detector on which it has not been measured is a realizable goal. The measurements provided here are meant to represent a relative proton light yield for the material itself and not the readout system. Using such a light yield requires some characterization of the system used with the material. The linearity of the readout system should be measured across the full range of anticipated light levels. The electron light yield should be established across a range of energies using multiple γ-ray sources. The results here require an extrapolation of the electron light yield from the maximum measured point, 4.4 MeVee, to the full scale range of the measurement at approximately 12 MeVee. This is not a desirable state, but the uncertainty referenced here should be reflective of that. Any linearity corrections should be made to the γ-ray calibration data prior to calibration, and then to the neutron data. The γ-ray calibration procedure should be a statistical characterization of the observed data. The method for doing outlined herein is accessible and robust, allowing simultaneous consideration of multiple Compton edges. Lastly, the integration length of the pulse should be similar to the light yield used in the analysis. Future investigations of potential factors that could affect the observed light output from the detection system and in turn, the light yield result, need explanation as to how they differentially affect the light observed from Compton electrons as compared to proton recoils.

8.2 Outcomes, Summary, and Outlook

The light yield results obtained in this work establish the double time of flight method as a viable technique for measuring proton light yield. This method enables measurement of the proton light yield over a broad range of energies without requiring changes to either detector positions or beam parameters. The limits on the proton recoil energy range assessed come from the energy distribution of the beam combined with the angular configuration, as well as the dynamic range of the readout system. In the measurements presented here, proton recoil energies ranging from $\sim 1 - 20$ MeV were accessible in a single measurement for both EJ301 and EJ309.

The detection system used in this work was studied in simulation space to characterize

the potential for bias due to differential spatial distributions of recoiling particles used for calibration and measurement purposes, and the results were included in the uncertainty quantification. Additionally, the proton energy resolution for the specific setup and beam parameters was assessed to provide a bin structure for the final result. The linearity of the system was measured using an established method to ensure that the non-linearity of the result was reflective of the relative relationship between the linear electron light yield and the proton light yield, and not non-linearities of the detection system.

The system was calibrated with respect to the electron light yield using a combination of γ-ray sources leading primarily to Compton electrons ranging from 0.45 to 4.4 MeV by means of a χ^2 minimization between simulations of the electron energy deposition and the measured distributions. Parameter error estimation was used to establish the correlation of the parameters, but was increased to match the systematic differences observed when generating different spatial distributions of energetic electrons. Future work would benefit from calibration data taken at the time of measurement that produces the same spatial distribution anticipated for the protons used to make the light yield measurement.

The systematic errors of the proton light yield measurement were assessed by Monte Carlo methods that modified the uncertain input parameters stochastically, appropriately managing correlations, and stored the results of individual trials. The individual trials were then assessed to establish systematic error, covariance, and correlation for the resultant light yield data points. The Monte Carlo trials were also fit to generate a set of parameters for the Birks semi-empirical model, providing parameters for the relation with covariance.

The method developed here can be used to access the lower energy regime for protons and potentially other neutron reactions in the scintillator. The need for reconstruction of the incoming time of flight puts a limit on the other reactions that can be assessed (i.e., they would need to be kinematically constrained). One such reaction is neutron elastic scattering on carbon. To approach a carbon light yield measurement, this would require changing detector gains and additional software development. Lower energy measurements, or light yield for other particles, would allow the testing of additional models such as those proposed by Voltz et al. [9].

An additional objective of this work was to develop a platform for measuring proton light yield at the 88-Inch Cyclotron. This has been accomplished by exploiting primarily commercially available hardware with a combination of open source software and a modular C++ framework developed for this analysis. The hardware is comprised of a CAEN V1730 16 channel 14 bit 500 Ms/S digitizer. It is managed by a modified version of the vendor-supplied acquisition software that writes to a compressed format in list mode including full waveforms. Use of the internal trigger logic for the purpose of light yield measurements was developed and tested. An experimental apparatus for measuring the linearity of the readout system was developed that includes fast avalanche pulsers coupled to UV LED modules as well as the design of control modules for managing the measurements.

The software development on this project was done with the intent of providing a modular and extensible framework for proton light yield analysis. The current features of the software include support for multiple basic procedures needed to produce well characterized results.

To begin, the software base includes a set of reduction algorithms that were developed for applying and testing signal processing algorithms needed to turn waveform data into pulse shape and pulse integral quantities. The pulse integral has been decoupled from the pulse shape algorithms to allow optimization of the pulse shape algorithms without influence on the integral quantity. Several methods of pulse shape discrimination are currently supported including multiple parameterizations of charge integration methods as well as the 90-10 algorithm used in this analysis. The waveform reduction algorithms include support for both clipping and pulse pile-up detection or rejection. The setup for the digital signal processing is managed through a simple ASCII configuration file. Next, the software base includes a framework for calibrating organic scintillators in MeVee using multiple γ-ray spectra in a χ^2 minimization procedure with graphical support for assessing starting points of the minimization, range selection, and assessment of the results. Supporting simulation code was developed to produce anticipated energy deposition spectra for detectors under study. The current simulations support EJ301 and EJ309, but can be easily extended to consider additional geometries and detection media. Next, the software base includes support for managing detector configuration information that includes geometrical information about detectors used in a scattering detector array as well as information regarding the relation between channels in the digitizer and the geometry. This information is again provided to the software through a simple ASCII file. Next, the software base includes support for temporally calibrating a scattering detector setup using coincidences between γ-ray events. This is managed through prompting the user for inputs regarding accumulated data. Next, the software includes support for developing a series of physics-based cuts on the data on an angle-by-angle basis by prompting the user for input regarding accumulated data. The constraints can then be applied to generate a subset of the data corresponding to physically relevant events. Next, the software includes adaptable support for simulation of a scattering array to assess the anticipated proton energy resolution needed for the data reduction. Again, the simulation currently assumes the geometry and material of the detectors used in this work, but is easily adaptable for consideration of other geometries and materials. Next, the software includes support for accumulating and characterizing the data representative of the proton light yield to produce a series of data points and associated error bars. This support is adaptable and can be employed with user feedback to generate a parameter map of the data used for stable repetitive fitting. Next, the software package includes support for a Monte Carlo assessment of the systematic uncertainties identified in the measurement technique and is easily extensible if additional sources of potential bias are identified. The software has algorithms for fitting the resultant trials of the Monte Carlo assessment with light yield models providing the relevant parameters and covariances on them. Additionally, reduction of the trials directly to a series of data points and an error matrix is supported.

The end result of the development is a hardware and software platform capable of producing proton light yield measurements with approximately 12 hours of beam time at the cyclotron. The amount of time needed depends on the number of scattering detectors employed and the energy range considered. An expanded scattering detector array is currently being developed that includes 12 scattering detectors, which should decrease the time needed

for a measurement by approximately half. Further geometry optimizations could be studied in a multi-parameter optimization algorithm that balances experimental uncertainties with efficiencies for an energy range of interest. With the current framework, an experienced user can take a collected dataset from the raw output of the measurement to a characterized result with a week of dedicated time. Additional experiments have been performed in an effort to explore the low energy regime to examine the limits of model extrapolation for a series of physical models of the light yield relation, and an experimental campaign on a series of fast plastics with prospective use in a compact neutron imaging device are planned in the near future.

Bibliography

[1] F. Pino, L. Stevanato, D Cester, G. Nebbia, L. Sajo-Bohus, and G. Viesti. The light output and the detection efficiency of the liquid scintillator EJ-309. *Applied Radiation and Isotopes*, 89:79 – 84, 2014.

[2] S. Agostinelli et al. GEANT4: A Simulation toolkit. *Nucl. Instrum. Meth.*, A506:250–303, 2003.

[3] F. D. Brooks. Development of organic scintillators. *Nuclear Instruments and Methods*, 162:477–505, June 1979.

[4] J. B. Birks. *The Theory and Practice of Scintillation Counting*. Macmillan, 1964.

[5] J. B. Birks. The specific fluorescence of anthracene and other organic materials. *Phys. Rev.*, 84:364–365, Oct 1951.

[6] G.F. Knoll. *Radiation Detection and Measurement*. John Wiley & Sons, 2010.

[7] James E Parks. The compton effect–compton scattering and gamma ray spectroscopy. 2004.

[8] C. J. Taylor, W. K. Jentschke, M. E. Remley, F. S. Eby, and P. G. Kruger. Response of some scintillation crystals to charged particles. *Phys. Rev.*, 84:1034–1043, Dec 1951.

[9] R. Voltz, J. Lopes da Silva, G. Laustriat, and A. Coche. Influence of the nature of ionizing particles on the specific luminescence of organic scintillators. *The Journal of Chemical Physics*, 45(9):3306–3311, 1966.

[10] D. Kraus, K. Lande, E. Leboy, and W. Selove. Detection of fractional–MeV neutrons in plastic scintillator. *Review of Scientific Instruments*, 29(12):1142–1143, 1958.

[11] J. R. Prescott and A. S. Rupaal. The specific fluorescence of plastic scintillator NE102. *Canadian Journal of Physics*, 39(1):221–227, 1961.

[12] M. Gettner and W. Selove. Pulse size from neutrons of 0.14 to 2.3 MeV in plastic scintillator. *Review of Scientific Instruments*, 31(4):450–451, 1960.

[13] R. Batchelor, W.B. Gilboy, J.B. Parker, and J.H. Towle. The response of organic scintillators to fast neutrons. *Nuclear Instruments and Methods*, 13(Supplement C):70 – 82, 1961.

[14] V. V. Verbinski, W. R. Burrus, T. A. Love, W. Zobel, N. W. Hill, and R. Textor. Calibration of an organic scintillator for neutron spectrometry. *Nuclear Instruments and Methods*, 65(1):8 – 25, 1968.

[15] N.V. Kornilov, I. Fabry, S. Oberstedt, and F.-J. Hambsch. Total characterization of neutron detectors with a 252Cf source and a new light output determination. *Nuclear*

Instruments and Methods in Physics Research Section A: Accelerators, Spectrometers, Detectors and Associated Equipment, 599(2–3):226 – 233, 2009.

[16] Andreas Enqvist, Christopher C. Lawrence, Brian M. Wieger, Sara A. Pozzi, and Thomas N. Massey. Neutron light output response and resolution functions in EJ-309 liquid scintillation detectors. *Nuclear Instruments and Methods in Physics Research Section A: Accelerators, Spectrometers, Detectors and Associated Equipment*, 715:79 – 86, 2013.

[17] J. Scherzinger, R. Al Jebali, J.R.M. Annand, K.G. Fissum, R. Hall-Wilton, K. Kanaki, M. Lundin, B. Nilsson, H. Perrey, A. Rosborg, and H. Svensson. The light-yield response of a NE-213 liquid-scintillator detector measured using 2–6 MeV tagged neutrons. *Nuclear Instruments and Methods in Physics Research Section A: Accelerators, Spectrometers, Detectors and Associated Equipment*, 840:121 – 127, 2016.

[18] Huaiyong Bai, Zhimin Wang, Luyu Zhang, Yi Lu, Haoyu Jiang, Jinxiang Chen, and Guohui Zhang. Calibration of an EJ309 liquid scintillator using an AmBe neutron source. *Nuclear Instruments and Methods in Physics Research Section A: Accelerators, Spectrometers, Detectors and Associated Equipment*, 863(Supplement C):47 – 54, 2017.

[19] D.L. Smith, R.G. Polk, and T.G. Miller. Measurement of the response of several organic scintillators to electrons, protons and deuterons. *Nuclear Instruments and Methods*, 64(2):157 – 166, 1968.

[20] W. Tornow, W. Arnold, J. Herdtweck, and G. Mertens. Measurement of the response of the deuterated scintillators NE 232 and NE 230 to protons and deuterons. *Nuclear Instruments and Methods in Physics Research A*, 244:477–482, April 1986.

[21] S. Yoshida, T. Ebihara, T. Yano, A. Kozlov, T. Kishimoto, I. Ogawa, R. Hazama, S. Umehara, K. Mukaida, K. Ichihara, Y. Hirano, I. Murata, J. Datemichi, and H. Sugimoto. Light output response of kamland liquid scintillator for protons and 12C nuclei. *Nuclear Instruments and Methods in Physics Research Section A: Accelerators, Spectrometers, Detectors and Associated Equipment*, 622(3):574 – 582, 2010.

[22] J. Iwanowska, L. Swiderski, T. Krakowski, M. Moszynski, T. Szczesniak, and G. Pausch. The time-of-flight method for characterizing the neutron response of liquid organic scintillators. *Nuclear Instruments and Methods in Physics Research Section A: Accelerators, Spectrometers, Detectors and Associated Equipment*, 781(Supplement C):44 – 49, 2015.

[23] Robert B. Galloway and Hadi Savalooni. The dependence on scintillator size of the response of NE213 to electrons and protons. *Nuclear Instruments and Methods in Physics Research*, 199(3):549 – 555, 1982.

[24] A. Tomanin, J. Paepen, P. Schillebeeckx, R. Wynants, R. Nolte, and A. Lavietes. Characterization of a cubic EJ-309 liquid scintillator detector. *Nuclear Instruments and Methods in Physics Research Section A: Accelerators, Spectrometers, Detectors and Associated Equipment*, 756(Supplement C):45 – 54, 2014.

[25] Joanna Iwanowska, Lukasz Swiderski, Tomasz Krakowski, Tadeusz Kozlowski, Marek Moszynski, and Guntram Pausch. Calibration of EJ309 liquid scintillator for neutron spectrometry. In *IEEE Nuclear Science Symposium Conference Record*, pages 149–152, 10 2012.

[26] Mark A. Norsworthy, Alexis Poitrasson-Riviére, Marc L. Ruch, Shaun D. Clarke, and Sara A. Pozzi. Evaluation of neutron light output response functions in EJ-309 organic scintillators. *Nuclear Instruments and Methods in Physics Research Section A: Accelerators, Spectrometers, Detectors and Associated Equipment*, 842(Supplement C):20 – 27, 2017.

[27] I. Antcheva, M. Ballintijn, B. Bellenot, M. Biskup, R. Brun, N. Buncic, Ph. Canal, D. Casadei, O. Couet, V. Fine, L. Franco, G. Ganis, A. Gheata, D. Gonzalez Maline, M. Goto, J. Iwaszkiewicz, A. Kreshuk, D. Marcos Segura, R. Maunder, L. Moneta, A. Naumann, E. Offermann, V. Onuchin, S. Panacek, F. Rademakers, P. Russo, and M. Tadel. ROOT A C++ framework for petabyte data storage, statistical analysis and visualization. *Computer Physics Communications*, 180(12):2499 – 2512, 2009. 40 YEARS OF CPC: A celebratory issue focused on quality software for high performance, grid and novel computing architectures.

[28] *User Manual UM2580 DPP-PSD Digital Pulse Processing for Pulse Shape Discrimination.*

[29] M. Faisal, R. T. Schiffer, M. J. Haling, M. Flaska, S. A. Pozzi, and D. D. Wentzloff. A data processing system for real-time pulse processing and timing enhancement for nuclear particle detection systems. *IEEE Transactions on Nuclear Science*, 60(2):619–623, April 2013.

[30] G. Dietze and H. Klein. Gamma-calibration of NE 213 scintillation counters. *Nuclear Instruments and Methods in Physics Research*, 193(3):549 – 556, 1982.

[31] K.P. Harrig, B.L. Goldblum, J.A. Brown, D.L. Bleuel, L.A. Bernstein, J. Bevins, M. Harasty, T.A. Laplace, and E.F. Matthews. Neutron spectroscopy for pulsed beams with frame overlap using a double time-of-flight technique. *Nuclear Instruments and Methods in Physics Research Section A: Accelerators, Spectrometers, Detectors and Associated Equipment*, 877(Supplement C):359 – 366, 2018.

[32] J P Meulders, P Leleux, P C Macq, and C Pirart. Fast neutron yields and spectra from targets of varying atomic number bombarded with deuterons from 16 to 50 MeV (for radiobiology and radiotherapy). *Physics in Medicine & Biology*, 20(2):235, 1975.

[33] M Friend, G Franklin, and B Quinn. An LED pulser for measuring photomultiplier linearity. *Nuclear Instruments and Methods in Physics Research Section A: Accelerators, Spectrometers, Detectors and Associated Equipment*, 676, 08 2011.

[34] M. Vi'cić, L.G. Sobotka, J.F. Williamson, R.J. Charity, and J.M. Elson. Fast pulsed UV light source and calibration of non-linear photomultiplier response. *Nuclear Instruments and Methods in Physics Research Section A: Accelerators, Spectrometers, Detectors and Associated Equipment*, 507(3):636 – 642, 2003.

[35] M.B. Chadwick, M. Herman, P. Oblozinsky, M.E. Dunn, Y. Danon, A.C. Kahler, D.L. Smith, B. Pritychenko, G. Arbanas, R. Arcilla, R. Brewer, D.A. Brown, R. Capote, A.D. Carlson, Y.S. Cho, H. Derrien, K. Guber, G.M. Hale, S. Hoblit, S. Holloway, T.D. Johnson, T. Kawano, B.C. Kiedrowski, H. Kim, S. Kunieda, N.M. Larson, L. Leal, J.P. Lestone, R.C. Little, E.A. McCutchan, R.E. MacFarlane, M. MacInnes, C.M. Mattoon, R.D. McKnight, S.F. Mughabghab, G.P.A. Nobre, G. Palmiotti, A. Palumbo, M.T.

Pigni, V.G. Pronyaev, R.O. Sayer, A.A. Sonzogni, N.C. Summers, P. Talou, I.J. Thompson, A. Trkov, R.L. Vogt, S.C. van der Marck, A. Wallner, M.C. White, D. Wiarda, and P.G. Young. Endf/b-vii.1 nuclear data for science and technology: Cross sections, covariances, fission product yields and decay data. *Nuclear Data Sheets*, 112(12):2887 – 2996, 2011. Special Issue on ENDF/B-VII.1 Library.

[36] A.R. Garcia, E. Mendoza, D. Cano-Ott, R. Nolte, T. Martinez, A. Algora, J.L. Tain, K. Banerjee, and C. Bhattacharya. New physics model in GEANT4 for the simulation of neutron interactions with organic scintillation detectors. *Nuclear Instruments and Methods in Physics Research Section A: Accelerators, Spectrometers, Detectors and Associated Equipment*, 868(Supplement C):73 – 81, 2017.

[37] Makoto Matsumoto and Takuji Nishimura. Mersenne twister: A 623-dimensionally equidistributed uniform pseudo-random number generator. *ACM Trans. Model. Comput. Simul.*, 8(1):3–30, January 1998.

[38] Masashi Takada, Kazuaki Yajima, So Kamada, Hiroshi Yasuda, and Takashi Nakamura. Simulated neutron response functions of phoswich-type neutron detector and thin organic liquid scintillator. *Prog. Nucl. Sci. Technol*, 2:274–279, 2011.

[39] Chris C. Lawrence, Michael Febbraro, Thomas Massey, Marek Flaska, Frederick Becchetti Jr, and Sara Pozzi. Neutron response characterization for an EJ299-33 plastic scintillation detector. *Nuclear Instruments and Methods in Physics Research Section A: Accelerators, Spectrometers, Detectors and Associated Equipment*, 759:16–22, 09 2014.

[40] *User Manual UM4380 725-730 DPP-PSD Registers: Register Description for 725 and 730.*

Appendix A

FreeWrites.txt File

Below is the FreeWrites.txt file used to build the coincident trigger logic in the CAEN DPP_PSD control software. For a complete description of the registers and modifications, see Ref. [40].

```
#CFD DISCRIMINATION
GENERIC_WRITE 0x1080 0x0040 0x0040
GENERIC_WRITE 0x1180 0x0040 0x0040
GENERIC_WRITE 0x1280 0x0040 0x0040
GENERIC_WRITE 0x1480 0x0040 0x0040
GENERIC_WRITE 0x1580 0x0040 0x0040
GENERIC_WRITE 0x1680 0x0040 0x0040
GENERIC_WRITE 0x1780 0x0040 0x0040
GENERIC_WRITE 0x1880 0x0040 0x0040
GENERIC_WRITE 0x1980 0x0040 0x0040
GENERIC_WRITE 0x1A80 0x0040 0x0040
#RF IN CH14
#to remove detection of opposite polarity
#signal [31] and disable trigger histeresis [30]
GENERIC_WRITE 0x1E80 0xC0000040 0xC0000040
############CFD settings
##### CFD delay= 4 ns   75% fraction
GENERIC_WRITE 0x103C 0x0202 0x0FFF
GENERIC_WRITE 0x113C 0x0202 0x0FFF
GENERIC_WRITE 0x123C 0x0202 0x0FFF
GENERIC_WRITE 0x143C 0x0202 0x0FFF
GENERIC_WRITE 0x153C 0x0202 0x0FFF
GENERIC_WRITE 0x163C 0x0202 0x0FFF
GENERIC_WRITE 0x173C 0x0202 0x0FFF
GENERIC_WRITE 0x183C 0x0202 0x0FFF
GENERIC_WRITE 0x193C 0x0202 0x0FFF
```

```
GENERIC_WRITE 0x1A3C 0x0202 0x0FFF
GENERIC_WRITE 0x1E3C 0x020C 0x0FFF
###ENABLE TRIGGER PROPAGATION
GENERIC_WRITE 0x8000 0x4 0x4
#########enables coincidences
#over_range rejection for 2 bit29
#bit18-19 trigger mode 4=coinc 0=normal C=anticoinc
GENERIC_WRITE 0x1080 0x20040000 0x200C0000
GENERIC_WRITE 0x1180 0x20040000 0x200C0000
GENERIC_WRITE 0x1280 0x20040000 0x200C0000
GENERIC_WRITE 0x1480 0x40000 0xC0000
GENERIC_WRITE 0x1580 0x40000 0xC0000
GENERIC_WRITE 0x1680 0x40000 0xC0000
GENERIC_WRITE 0x1780 0x40000 0xC0000
GENERIC_WRITE 0x1880 0x40000 0xC0000
GENERIC_WRITE 0x1980 0x40000 0xC0000
GENERIC_WRITE 0x1A80 0x40000 0xC0000
GENERIC_WRITE 0x1E80 0x40000 0xC0000
###SHAPE TRIGGER
GENERIC_WRITE 0x1070 0x2C 0xFF
GENERIC_WRITE 0x1170 0x2C 0xFF
GENERIC_WRITE 0x1270 0x2C 0xFF
GENERIC_WRITE 0x1470 0x08 0xFF
GENERIC_WRITE 0x1570 0x08 0xFF
GENERIC_WRITE 0x1670 0x08 0xFF
GENERIC_WRITE 0x1770 0x08 0xFF
GENERIC_WRITE 0x1870 0x08 0xFF
GENERIC_WRITE 0x1970 0x08 0xFF
GENERIC_WRITE 0x1A70 0x08 0xFF
GENERIC_WRITE 0x1E70 0x0C 0xFF
########TRIGGER OFFSET (NEVER CHANGES)
GENERIC_WRITE 0x106C 0x9 0xFF
GENERIC_WRITE 0x116C 0x9 0xFF
GENERIC_WRITE 0x126C 0x9 0xFF
GENERIC_WRITE 0x146C 0x9 0xFF
GENERIC_WRITE 0x156C 0x9 0xFF
GENERIC_WRITE 0x166C 0x9 0xFF
GENERIC_WRITE 0x176C 0x9 0xFF
GENERIC_WRITE 0x186C 0x9 0xFF
GENERIC_WRITE 0x196C 0x9 0xFF
GENERIC_WRITE 0x1A6C 0x9 0xFF
GENERIC_WRITE 0x1E6C 0x9 0xFF
```

```
#### INTERNAL TRIGGER SETUP
# bit0-3 ->5 even channel only 7->BOTH CH
# bit 4-7 -> 5 is trig validation from mother
#board 7 is OR = self validation
# bit 8-11 -> 2 Extended time stamp /
#flag / fine time stamp print
GENERIC_WRITE 0x1084 0x257 0x777
GENERIC_WRITE 0x1184 0x257 0x777
GENERIC_WRITE 0x1284 0x257 0x777
GENERIC_WRITE 0x1484 0x257 0x777
GENERIC_WRITE 0x1584 0x257 0x777
GENERIC_WRITE 0x1684 0x257 0x777
GENERIC_WRITE 0x1784 0x257 0x777
GENERIC_WRITE 0x1884 0x257 0x777
GENERIC_WRITE 0x1984 0x257 0x777
GENERIC_WRITE 0x1A84 0x257 0x777
GENERIC_WRITE 0x1E84 0x255 0x777
######## TRIGGER MASK
GENERIC_WRITE 0x8180 0x22C 0xFFF
GENERIC_WRITE 0x8184 0x22C 0xFFF
GENERIC_WRITE 0x8188 0x203 0xFFF
GENERIC_WRITE 0x818C 0x203 0xFFF
GENERIC_WRITE 0x8190 0x203 0xFFF
GENERIC_WRITE 0x8194 0x203 0xFFF
GENERIC_WRITE 0x819C 0x62F 0xFFF
```

Appendix B

configFile.dat File

The configuration file used for informing the analysis code of the specifics of the experimental setup is presented below. Lines preceded by a line with three backslashes are detector location and orientation specification in the form: $x, y, z, rotx, roty, rotx, detectordepth$, where *rot* specifies components of a vector running from the front face to the back of the detector allowing specification of the orientation of the detector in space. The configuration file must have a line following four backslashes that specifies the channels the detectors are connected to in the data acquisition system.

```
///
79.8 0 0.2 0 0 1 5.08
///
79.8 0 -.1 0 0 -1 5.08
///
124.3 125.1 0 10.5 29 0 5.08
///
144.2 118.3 0 12.5 27 0 5.08
///
169.4 108.55 5.6 0 0 1 5.08
///
169.4 108.55 0 0 0 -1 5.08
///
181.1 76.9 0 30 17 -1 5.08
////
0 2 5 4 6 7 10
/////
1 1 0 0 0 0 0
//**
14
//**sourceloc
79.8 2 0
```

```
//**WESTWALL
647.2
//**CYCPERIOD
111.094
```

Appendix C

gammaReduction.txt File

```
//#
AlActivation
Background_001.0_SE.root
Background_001.1_SE.root
Background_001.2_SE.root
Background_001.3_SE.root
//#
AmBeGamma
AmBe_003.0_SE.root
AmBe_003.1_SE.root
AmBe_003.2_SE.root
//#
Cs137
137Cs_001.0_SE.root
137Cs_001.1_SE.root
137Cs_001.2_SE.root
//#
background
background_002.0_SE.root
background_003.0_SE.root
background_004.0_SE.root
background_004.1_SE.root
background_004.2_SE.root
background_004.3_SE.root
///#
0 2
////#
4 12.8 4 12.5
```